The use of energetic ions to determine some aspects of the dynamics of the geomagnetic tail.

Neil Murphy.

Thesis submitted for the degree
of Doctor of Philosophy
of the University of London, and for the
Diploma of Membership of Imperial College.

October 1987.

Department of Physics,
Imperial College of Science and Technology,
London SW7 2BZ.

Avoid the teachings of speculators
whose judgements are not confirmed by experience.

Leonardo da Vinci

CONTENTS

	Page
Abstract	8
Acknowledgements	10
List of figures	5
List of tables	7
Chapter 1. Introduction.	11
The ISEE mission.	12
The structure of the earths magnetotail.	18
ISEE-3 magnetotail results.	24
Chapter 2. Instrumentation and analysis techniques.	31
The ISEE-3 payload.	32
The EPAS instrument.	34
System design.	35
Particle detectors.	37
Detector telescopes.	38
Other possible sources of contamination in the proton energy channels.	43
Analysis techniques.	44
Chapter 3. Travelling compression regions in the magnetotail lobes.	49
Introduction.	50
Geomagnetic data.	52
Properties of TCRs, as determined from the magnetic field and geomagnetic data.	54
Frequency distribution of TCR properties.	60
Variation of TCR properties with position.	60
Variation of TCR properties not dependent on position.	82
Effects of TCRs on energetic ion fluxes.	82
Energetic ion enhancements associated with TCRs.	83
Conclusions.	104
Energetic ion decreases associated with TCRs.	109
Interpretation.	113
TCRs not showing any effect in energetic ion fluxes.	115

Chapter 4. Determination of the thickness of the plasma sheet in the distant magnetotail. 11

Introduction. 117
Data selection. 118
Results of thickness measurements. 130
Plasma flow and magnetic field topology. 135

Chapter 5. Magnetotail flux ropes. 145

Introduction. 146
Magnetic field observations. 146
Energetic ion observations. 153
Conclusions. 164

Chapter 6. Concluding remarks. 165

References. 170

List of figures.

1.1 ISEE-3 orbit around sun-earth libration point. 13
1.2 ISEE-3 first two geotail orbits. 15
1.3 ISEE-3 geotail orbits 3 and 4. 16
1.4 ISEE-3 geotail orbits 5 and 6. 17
1.5 Model magnetosphere (after Ness, 1965.). 19
1.6 Model of plasmoid formation (after Hones et al., 1984.). 23
1.7 Magnetotail model, with curved neutral line (after Slavin et al., 1985.). 26
1.8 A cross section of the distant magnetotail (after Gosling et al., 1985). 27
1.9 Twisted magnetotail (after Cowley 1981.). 28

2.1 Cross section of an EPAS telescope (after v Rooijen et al., 1979.). 39
2.2 Block diagram of EPAS (after van Rooijen et al., 1979.). 40
2.3 EPAS viewing directions in the GSE Y-Z plane (after Murphy et al., 1987.). 46

3.1 Magnetic field data between 0230 and 0430 UT on 14th April 1983. 51
3.2a Histogram of TCR compression ratio. 56
3.2b Histogram of TCR duration. 57
3.2c Histogram of TCR velocity. 58
3.2d Histogram of TCR length. 59
3.3a Compression ratio plotted against -GSM'X 62
3.3b TCR duration plotted against -GSM'X. 63
3.3c TCR velocity plotted against -GSM'X. 64
3.3d TCR length plotted against -GSM'X. 65
3.4a Compression ratio plotted against |GSM'Y|. 67
3.4b TCR duration plotted against |GSM'Y| 68
3.4c TCR velocity plotted against |GSM'Y|. 69
3.4d TCR length plotted against |GSM'Y|. 70
3.5a Compression ratio plotted against |GSM'Z|. 72
3.5b TCR duration plotted against |GSM'Z| 73
3.5c TCR velocity plotted against |GSM'Z|. 74
3.5d TCR length plotted against |GSM'Z|. 75
3.6a TCR observations in the GSM'X-|Z| plane. 77
3.6b TCR observations in the GSM'|X|-|Z| plane. 78
3.6c TCR observations in the GSM'X-|Y| plane. 79
3.7a Compression ratio plotted against TCR duration. 80
3.7b Compression ratio plotted against TCR length. 81

3.8a Omnidirectional ion flux compared with magnetic field between 1730 and 1830 UT on October 21st 1982. 84
3.8b Omnidirectional ion flux compared with magnetic field between 1400 and 1500 UT on October 22nd 1982. 85
3.8c Omnidirectional ion flux compared with magnetic field between 0230 and 0430 UT on April 14th 1983. 89
3.8d Omnidirectional ion flux compared with magnetic field between 0600 and 0700 UT on March 21st 1983. 90
3.8e AFGL magnetogram for the period 0500 to 0700 UT on March 21st 1983. 91
3.9a Streaming ion and 90° pitch angle ion fluxes compared with magnetic field magnitude between 1730 and 1830 UT on October 21st 1982. 95
3.9b Streaming ion and 90° pitch angle ion fluxes compared with magnetic field magnitude between 1400 and 1500 UT on October 22nd 1982. 96
3.9c Streaming ion and 90° pitch angle ion fluxes compared with magnetic field magnitude between 0230 and 0430 UT on April 14th 1983. 100
3.9d Streaming ion and 90° pitch angle ion fluxes compared with magnetic field magnitude between 0600 and 0700 UT on March 21st 1983. 101
3.10 A possible scenario for TCR production. 108
3.11a Omnidirectional ion flux compared with magnetic field between 0530 and 0630 UT on December 26th 1982. 111
3.11b Omnidirectional ion flux compared with magnetic field between 1300 and 14000 UT on December 26th 1982. 112

4.1a Omnidirectional ion flux compared with magnetic field between 0830 and 0930 UT on March 7th 1983. 121
4.1b Streaming ion and 90° pitch angle ion fluxes compared with magnetic field magnitude between 0830 and 0930 UT on March 7th 1983. 122
4.2a Omnidirectional ion flux compared with magnetic field between 2100 and 2200 UT on January 21st 1983. 126
4.2b Streaming ion and 90° pitch angle ion fluxes compared with magnetic field magnitude between 2100 and 2200 UT on January 21st 1983. 127
4.3 Histogram of plasma sheet thickness. 131
4.4 Plasma sheet thickness plotted against GSM'X. 132
4.5 Plasma sheet thickness plotted against GSM'|Y|. 133

4.6 Histogram of plasma sheet inclination. 138
4.7 Twisted magnetotail (after Cowley 1981.). 139
4.8 A model of the magnetotail, with a curved neutral line (after Slavin et al., 1985.). 143

5.1 Magnetic field data for the three flux rope events. 147
5.2a Model flux rope. 150
5.2b Section of a model flux rope. 150
5.3a Omnidirectional ion flux for the period 0200 to 0300 UT on December 28th 1982. 151
5.3b Omnidirectional ion flux for the period 0430 to 0530 UT on December 30th 1982. 152
5.3c Omnidirectional ion flux for the period 0700 to 0800 UT on March 25th 1983. 152
5.4 Streaming ion and 90° pitch angle ion fluxes compared with magnetic field magnitude between 0200 and 0300 UT on December 28th 1982. 154
5.5 Streaming ion and 90° pitch angle ion fluxes compared with magnetic field magnitude between 0430 and 0530 UT on December 30th 1982. 155
5.6 Streaming ion and 90° pitch angle ion fluxes compared with magnetic field magnitude between 0700 and 0800 UT on March 25th 1983. 156
5.7 Entry and exit velocities for the three flux rope events. 158
5.8 Model trajectory for ISEE-3 through the flux rope in event 3. 162

Abstract.

The ISEE-3 geotail mission consisted of 6 highly eccentric earth orbits, during which ISEE-3 was kept in the region of the nominal magnetotail by a series of close lunar encounters (Farquhar and Dunham, 1981.). The maximum apogee was 230 R_E, and the mission lasted for approximately 12 months. The research presented in this thesis is based on observations made during the ISEE-3 geotail mission.

In chapter 3 we examine the energetic ion characteristics of travelling compression regions (TCRs) in the magnetotail lobes, and conclude that enhancements in energetic ion flux associated with TCRs are caused by motion of the plasma sheet boundary layer. This supports the model developed by Slavin et al., 1984, which explains TCRs in terms of the tailward motion of plasmoids.

Chapter 4 deals with rapid crossings of the magnetotail neutral sheet. Energetic ion remote sensing is used to determine the velocity of the plasma sheet, as it moves across ISEE-3, from which the thickness of the plasma sheet is calculated. It is found that during this type

of crossing the average thickness of the plasma sheet is $1.2 \pm 0.8\ R_E$.

In chapter 5 energetic ion remote sensing is used to examine the structure of three events seen in the magnetotail lobes and reported to be flux ropes (Sibeck et al., 1984.). It is concluded that two of these events are most probably flux ropes, whilst the third is definitely not.

Acknowledgements.

I would like to thank the following, who have assisted in the production of this thesis:

The Science and Engineering Research Council, for the provision of a research studentship.

Those who have contributed to the design and construction of the Energetic Proton Anisotropy Spectrometer (EPAS).

J.A. Slavin and W.J. Hughes, for the provision of magnetic field and ground magnetogram data, and for providing useful advice.

F.L. Scarf for the provision of ISEE-3 wave data.

Geza Erdos, for developing the data plotting programs.

S.W.H. Cowley, I.G. Richardson, D.G. Sibeck, R.C. Elphic and C. Farrugia for their useful advice.

And finally, R.J. Hynds for his support and patient supervision.

Chapter 1

Introduction

The ISEE mission.

The International Sun Earth Explorer (ISEE) mission consisted of three spacecraft, ISEE-1, ISEE-2 and ISEE-3. ISEE-1 and 2 were launched in 1977 and placed into earth orbit, with an inclination of 28^{O} and an apogee of 23 R_E. The inter-spacecraft distance was small and was varied by manoeuvring ISEE-2. This part of the mission was designed to study small scale structures in the magnetosphere and utilised dual spacecraft observations in order to separate spatial and temporal effects.

ISEE-3 was launched on 12 August 1978 and was placed in orbit around the sun-earth libration point L_1 , 240 R_E sunward of the earth, on 20 November 1978 (the libration point, of course, corotates with the earth) (Figure 1.1, after Farquhar et al., 1985). ISEE-3 was the first spacecraft to attempt to use this type of halo orbit. The orbit was elliptical, with a semi major axis of 100 R_E along GSE Y and a semi minor axis of 17 R_E along GSE Z. This orbit meant that the line of sight from earth to ISEE-3 was always between 4^{O} and 26^{O} from the sun-earth line, thus avoiding the region within 3.5^{O} of the sun-earth line where solar radio noise would have swamped the spacecraft transmissions. The reasons for placing ISEE-3 in this orbit were twofold; firstly, in this position ISEE-3 could make continuous long term observations of

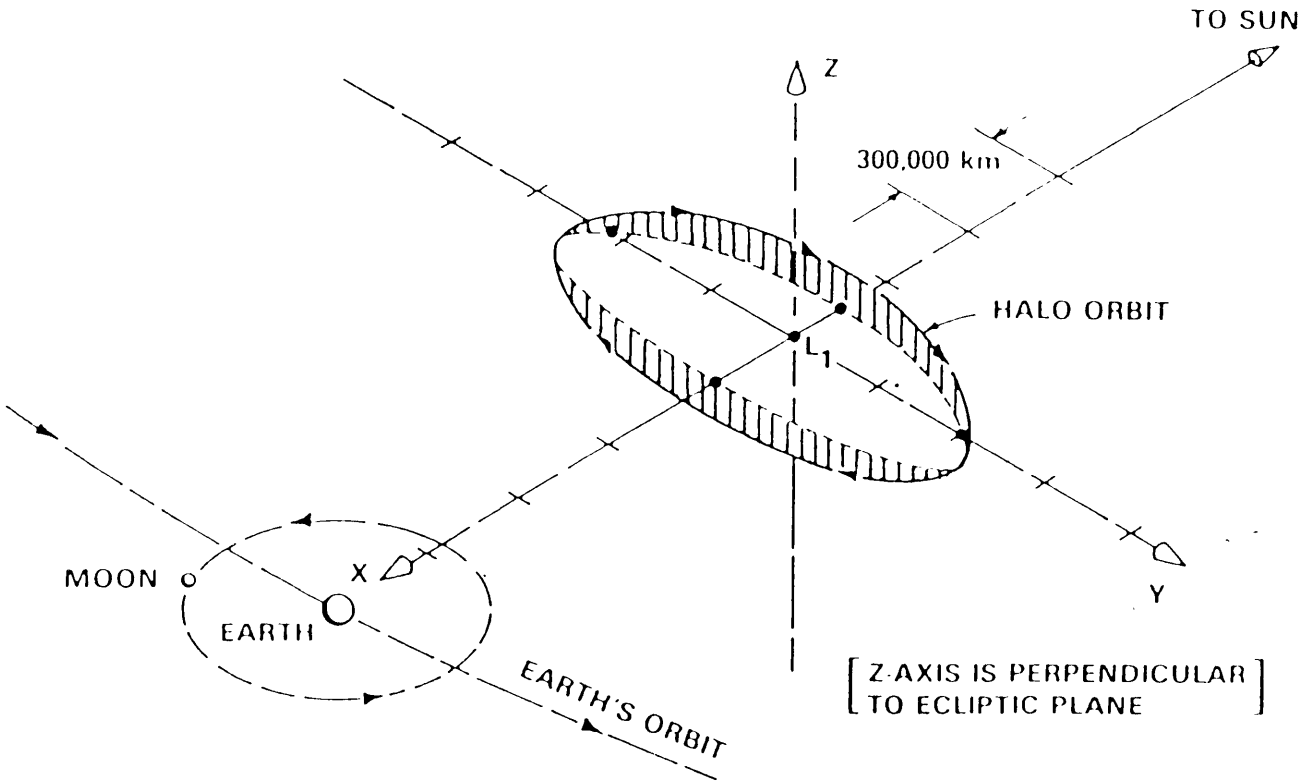


Figure 1.1) ISEE-3's orbit around the sun-earth libration point L1. The orbit of the moon is shown for comparison (After Farquhar et al., 1985).

the solar wind, interplanetary magnetic field and cosmic rays, as it always remained in interplanetary space, and secondly, ISEE-3 could act as an upstream solar wind monitor for ISEE-1 and 2, so providing prior warning of the arrival of interplanetary shocks and high speed solar wind streams.

On June 10^{th} 1982 the second phase of the ISEE-3 mission began, when the spacecraft was removed from halo orbit, using its hydrazine thrusters. From this position ISEE-3 then moved into a series of 6 highly eccentric earth orbits which allowed it to examine, for the first time, the structure of the distant geomagnetic tail out to an apogee of 238 R_E. The opportunity to study the magnetotail was afforded by a series of unique, close lunar encounters (Farquhar and Dunham, 1981.), which allowed ISEE-3 to remain within the region of the nominal magnetotail for most of the geotail mission (approximately 12 months). Figure 1.2) (after Farquhar et al., 1985) shows the transfer trajectory of ISEE-3 from halo orbit into the magnetotail, and the first two orbits in the geotail mission, whilst figures 1.3) and 1.4) (after Farquhar et al., 1985) show the remaining orbits comprising the geotail mission.

The final lunar encounter, marked S_5 in figure 1.4, was used to project ISEE-3 out of the earth moon system, in

TRANSFER FROM L1 HALO ORBIT TO GEOMAGNETIC TAIL

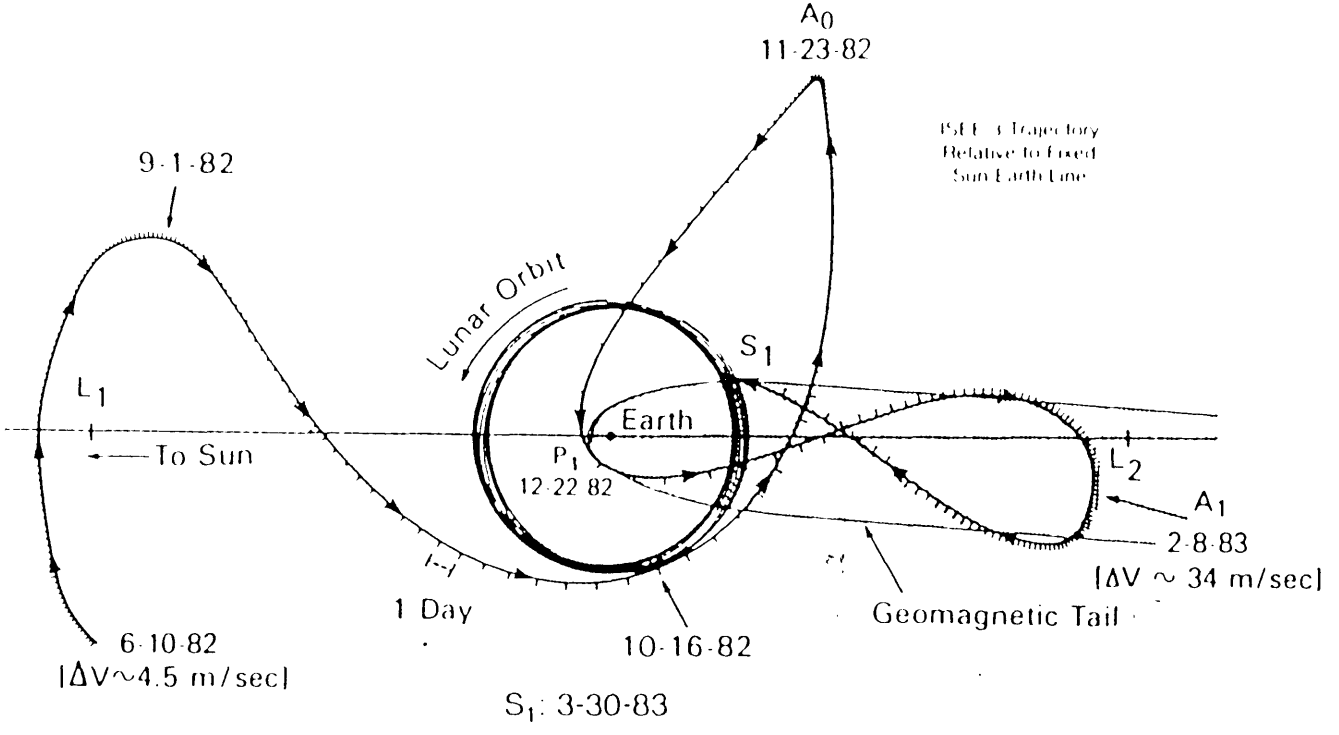


Figure 1.2) ISEE-3's trajectory out of orbit around the L1 libration point, and the first two geotail orbits. S1 marks the position of ISEE-3's first encounter with the moon. A0 and A1 are the positions of the first two orbital apogees (After Farquhar et al., 1985).

FIVE-MONTH GEOTAIL EXCURSION

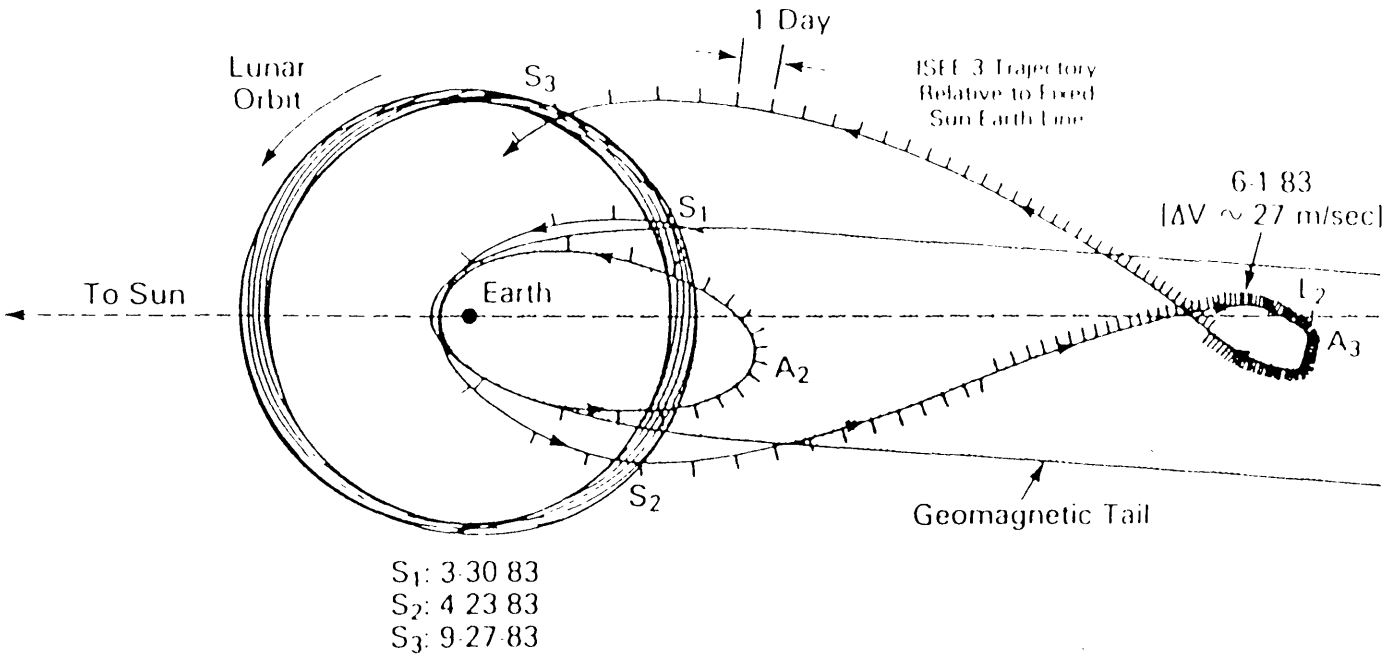


Figure 1.3) Orbits 3 and 4 in the geotail mission. S1, S2 and S3 show the positions of the first three lunar encounters. A2 and A3 are the third and fourth apogees (After Farquhar et al., 1985).

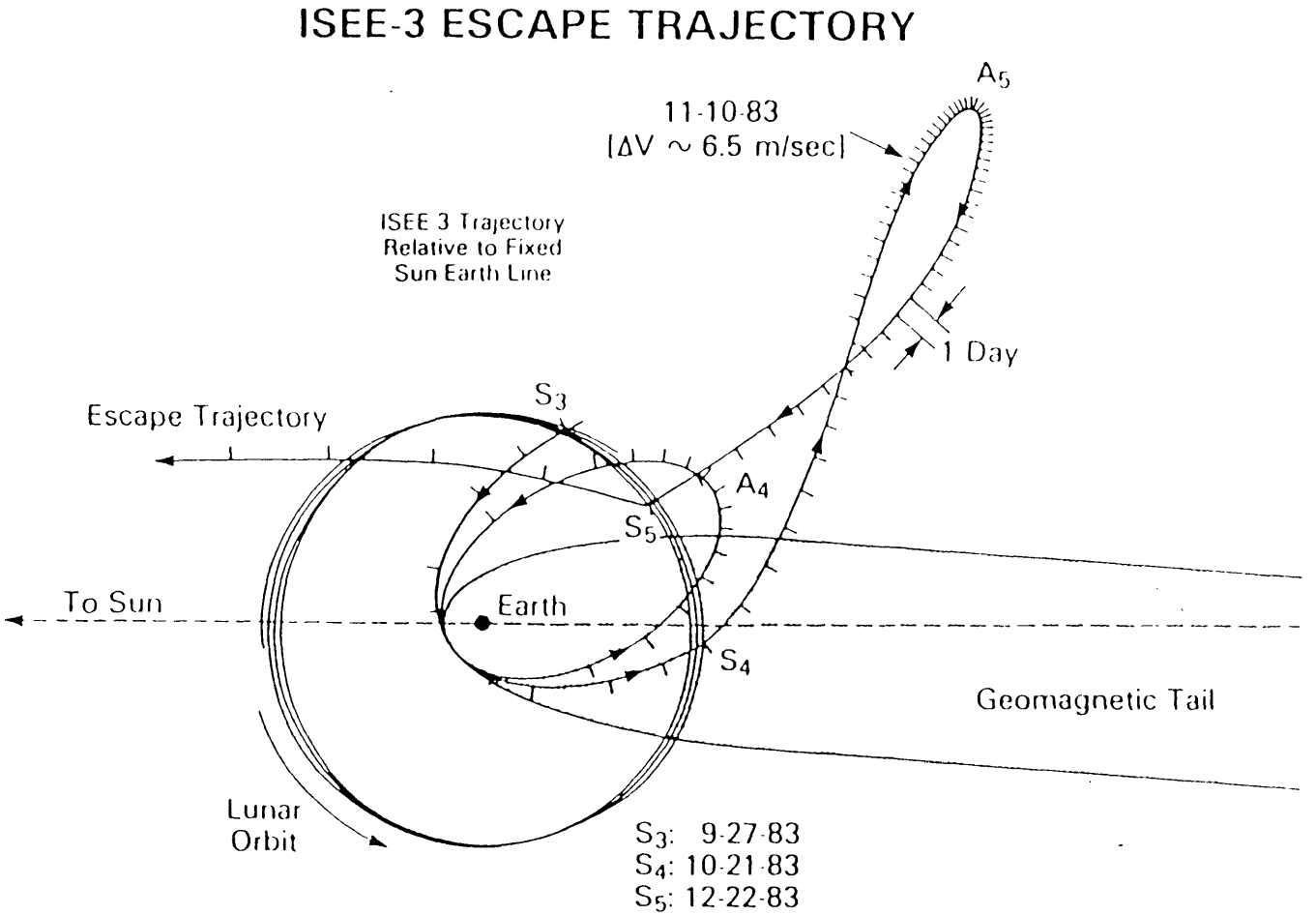


Figure 1.4) The final two orbits in the geotail mission, together with ISEE-3's escape trajectory from the earth-moon system (After Farquhar et al., 1985).

preparation for the encounter with comet Giacobini-Zinner on September 11th 1985. Following this flyby of the moon ISEE-3 was renamed the International Cometary Explorer (ICE). In order to gain sufficient gravitational energy to leave the earth moon system, the final lunar flyby took place at an altitude of less than 120 km on the dark side of the moon. After the successful completion of the Giacobini-Zinner phase of the mission, ICE was used to provide upstream solar wind data for the comet Halley missions.

The structure of the earths magnetotail

The fact that the earth's magnetic field was dragged out, in the antisolar direction, to form some kind of magnetic tail was first suggested by Explorer X observations, made in 1961 (Heppner et al., 1963) and Explorer XIV observations, made in 1963 (Cahill 1964). Both these sets of observations suggested that the earths magnetic field was distorted away from the sun. The first comprehensive observations of the earths magnetotail, and its embedded magnetic neutral sheet were made by IMP I (Explorer XVIII), and reported by Ness in 1965. IMP I observations were made out to a distance of 31.4 R_E, and established the existence of a twin lobed tail surrounding a magnetic neutral sheet containing energized plasma. Figure 1.5 shows the model used to interpret the

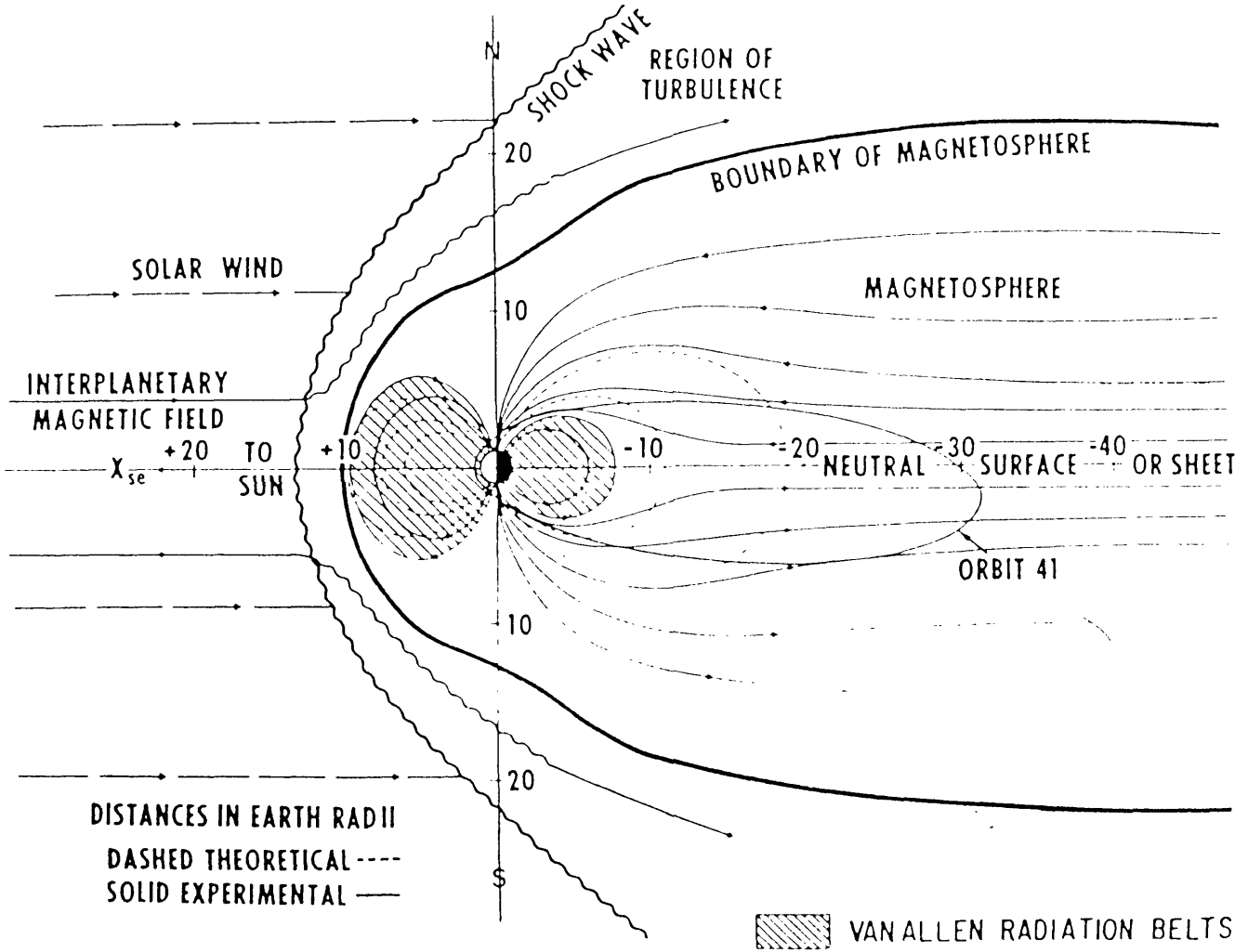


Figure 1.5) Illustrates the magnetic field topology used to interpret IMP I observations of the magnetotail. The dashed lines indicate early predictions of magnetic field line configurations in the nightside magnetosphere (After Ness, 1965).

observations made by IMP I, and is taken from Ness 1965. As figure 1.5 shows, the magnetic field in the tail lobes was found to be either closely parallel or antiparallel to the sun-earth line. The possible existence of a neutral sheet was suggested by Dungey 1961, and also discussed by Axford et al., 1964. The Ness 1965 paper is also important in introducing the Geocentric Solar Magnetospheric coordinate system as a tool in the study of the magnetosphere and magnetotail.

In parallel with early observational work theoretical studies of the magnetotail were also taking place. Early models of the interaction of the solar wind with the earths magnetic field were developed by Axford and Hines, 1961, and Dungey, 1961. The former work proposed that the magnetosphere was topologically distinct from the interplanetary magnetic field (IMF), and that momentum transfer took place between the solar wind and the magnetosphere by way of a viscous interaction. Dungey, in the latter work, proposed that magnetic field reconnection took place on the dayside magnetopause, ie the boundary of the magnetosphere, and was balanced by magnetic field reconnection in the magnetotail. This meant that the magnetosphere was 'open' to the IMF and solar wind, and the idea of momentum transfer via viscous interactions was unnecessary to explain plasma convection within the magnetosphere.

Based on the model proposed by Axford and Hines, Dessler (Dessler 1964) calculated the length of the magnetotail, by considering the effects of hydromagnetic wave pressure. Dessler's calculations led him to postulate a magnetotail which was terminated by external effects in the solar wind, with a length between 20 and 50 AU (of the order of 10^6 R_E). By considering the magnetosphere as being open Dungey (Dungey 1965) calculated a length for the magnetotail of the order of 10^3 R_E, which is a factor of 10^3 less than that proposed by Dessler. Dungey's calculation was based on considering the length of time a magnetic field line, reconnected on the dayside magnetopause, would remain connected to the earth, and the distance the free end of this magnetic field line would travel in this time. His calculation, therefore, gives us the length of the topological magnetotail, ie the extent of the magnetotail which is connected to the earth. The open model of the magnetosphere, suggested by Dungey, implies a magnetotail which is terminated by intrinsic means, rather than by the external effects of the solar wind.

One important consequence of the existence of a neutral sheet in the magnetotail was recognized by Ness 1965, that is, its inherent instability. This recognition was based on early laboratory work on sheet pinches, carried

out as part of the thermonuclear fusion program (Furth et al., 1963). The acceleration of particles by magnetic reconnection across a neutral sheet was proposed by Petschek 1963, and this mechanism was taken up as an explanation for auroral phenomena and geomagnetic substorms, in contrast to the mechanism proposed by Dessler and Juday, 1964, which argued that auroral particles were accelerated at the magnetospheric boundary. An overview of theoretical work on reconnection, as applied to the magnetotail, can be found in Vasyliunas, 1975. Evidence for the acceleration of particles in 'fireballs' on the magnetopause was claimed by Frank et al., 1976, but this remains a controversial claim.

The first trans lunar observations of the earth's magnetotail were made by Pioneer 8, at 500 R_E, (Bavassano et al., 1974) and Pioneer 7 at 1000 R_E and 3100 R_E (Walker et al., 1975, Intriligator et al., 1979). Both these sets of observations were made by single spacecraft passes through the magnetotail, but still provide evidence for a well ordered twin lobe structure at these distances (although early analyses of these data provided inconclusive results).

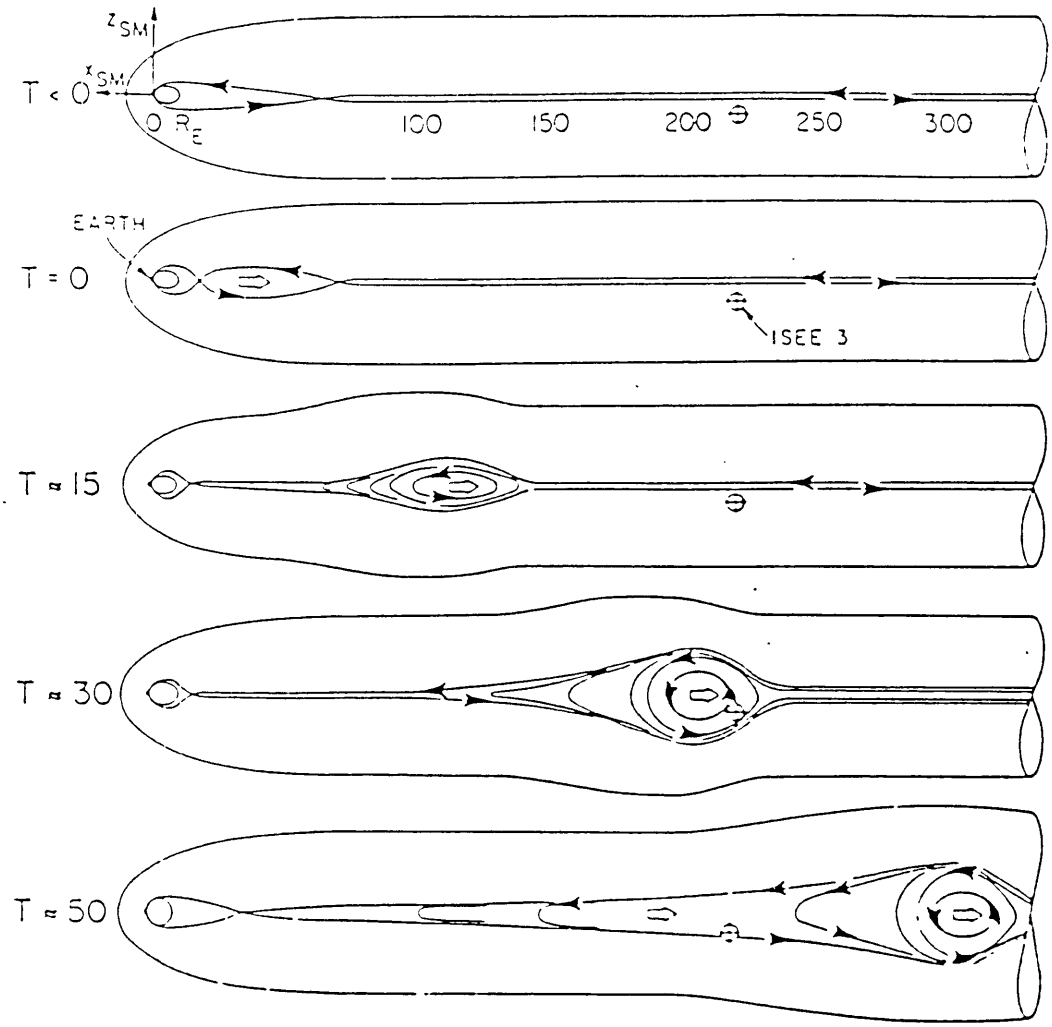


Figure 1.6) A model of plasmoid formation in the magnetotail, taken from Hones el al., 1984. An approximate timescale is indicated by T in minutes.

ISEE-3 magnetotail results

The ISEE-3 geotail mission provided the first extended observations of the magnetotail at trans lunar distances. Early results confirmed the previous picture of the magnetotails twin lobed structure (Bame et al., 1983, Slavin et al., 1983) and the energetic ion populations in the magnetotail were described in Cowley et al., 1984. Further work on interpretation of ISEE-3 results focussed on the determination of the relationship between the magnetotail and geomagnetic activity, and in particular geomagnetic substorms. One prediction of the open model of the magnetosphere was the formation of closed magnetic field islands, during substorm activity (Hones 1976). These islands, named plasmoids, play a major part in models of the transfer of magnetic flux from the magnetotail during substorm activity. Observations of plasmoids in the magnetotail were reported by Hones et al., 1984, and figure 1.6) shows the model developed to explain these observations. Further observations of the characteristics of plasmoids were reported by Baker et al., 1984 and Scholer et al., 1984. The properties of the plasma sheet energetic ion boundary layer, seen during the passage of plasmoids down the magnetotail, were investigated by Richardson and Cowley, 1987, whilst the properties of the plasma sheet, during plasmoid events were investigated in Richardson et al 1987. The

possible effects of the tailward passage of plasmoids on the magnetotail lobes were reported by Slavin et al., 1984. These effects consist of a compression of the lobe magnetic field travelling along the magnetotail, with the plasmoid, and were termed travelling compression regions.

ISEE-3 based studies were also conducted in order to determine the average quiet time structure of the magnetotail, that is, the magnetotail configuration when not disturbed by geomagnetic activity (Slavin et al., 1985, Tsurutani et al., 1987). An important feature of the quiet time magnetotail is the position of the neutral line. Early estimates of this position suggest that it is highly variable, but on average around -120 R_E GSE X (Zwickl et al., 1984, Cowley et al., 1984, Scholer et al., 1984). Slavin et al., 1985, by consideration of the variation of plasma parameters across the magnetotail, infer that the quiet time neutral line is in fact curved. Figure 1.7) shows a schematic diagram of the average position of the quiet time neutral line, taken from Slavin et al., 1984. As can be seen from this figure the position of the neutral line varies from just over 120 R_E at the centre of the plasma sheet, out to over 280 R_E at the magnetopause. The quiet time lobe magnetic field conditions were determined by Tsurutani et al., 1987, who found that the quiet time lobe magnetic field strength between 200 and 238 R_E was 7.1 nT (The average lobe

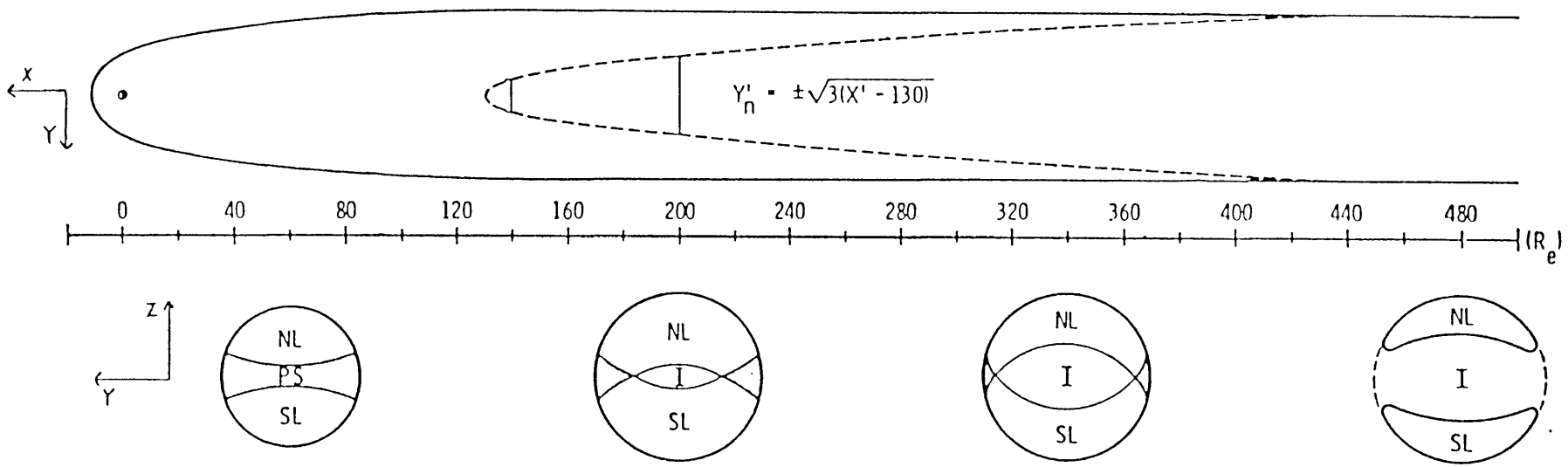


Figure 1.7) A model of the average distant tail magnetic field topology based on a curved neutral line. The upper part of the figure is a cut in the X-Y plane, with a model neutral line shown dashed. The bottom part of the figure shows four cuts through the magnetotail parallel to the Y-Z plane. NL signifies the northern tail lobe SL the southern tail lobe, PS the plasma sheet, and I interplanetary magnetic field lines (after Slavin et al., 1985.)

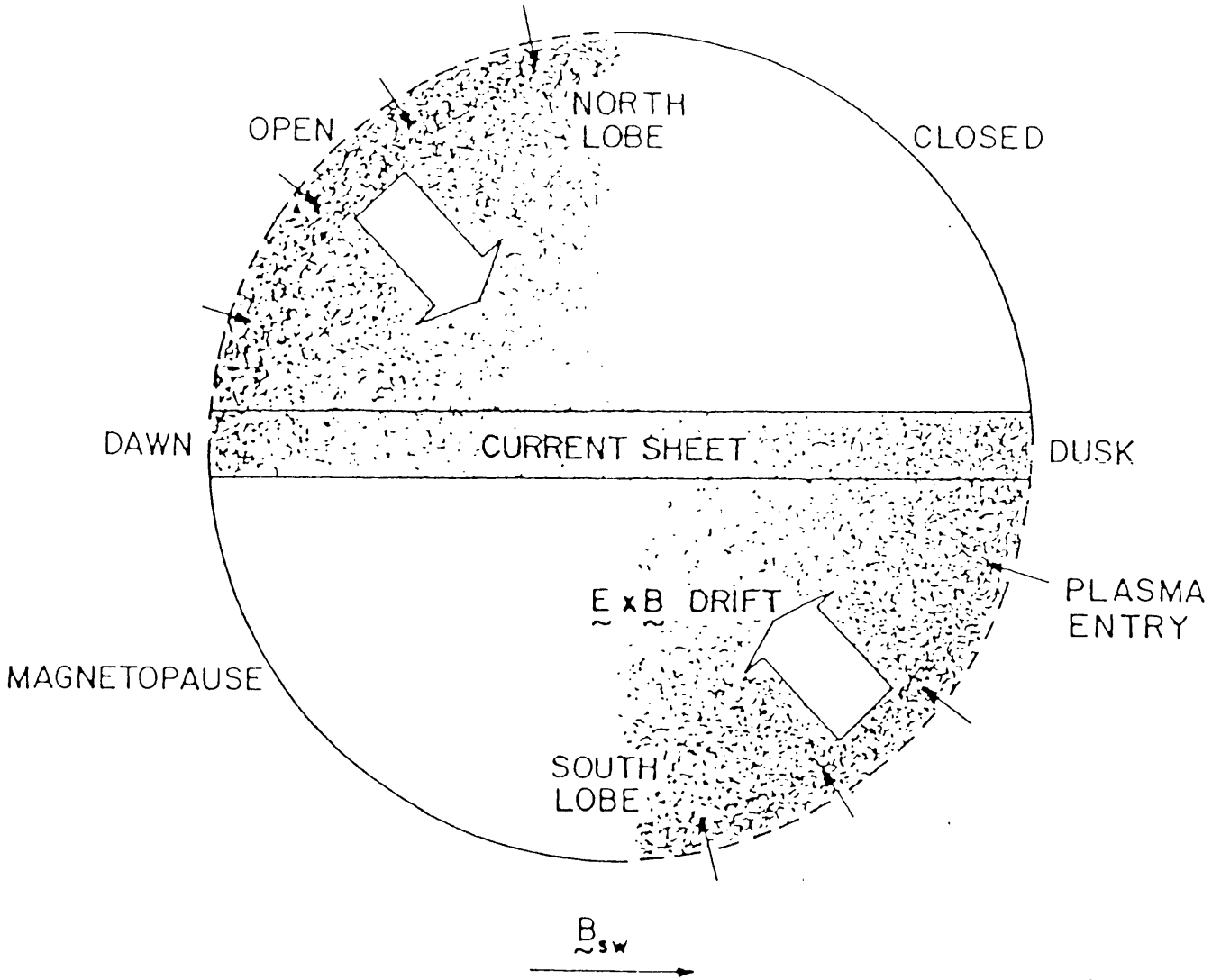


Figure 1.8) A cross section of the distant magnetotail, for IMF By positive. The regions of enhanced plasma density, in the lobes are shown shaded (after Gosling et al., 1985.).

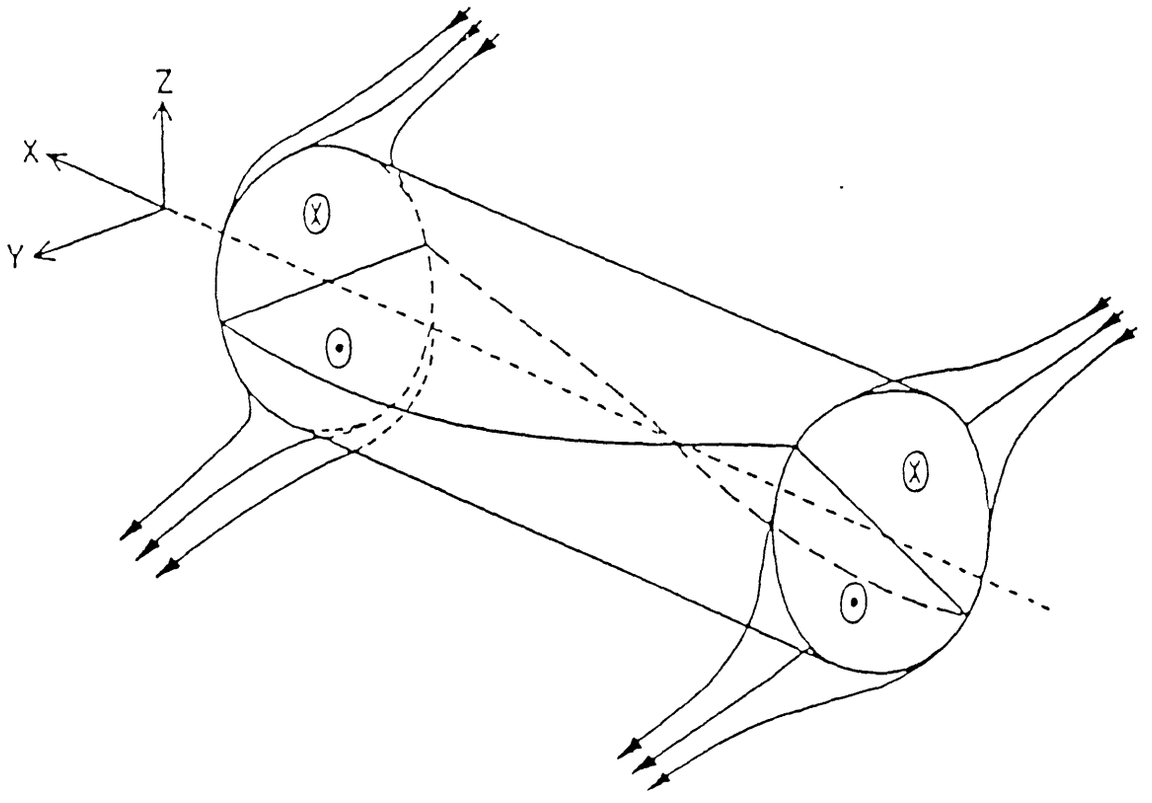


Figure 1.9) Shows the twist on the magnetotail resulting from the penetration of the IMF, when IMF By is positive. X, Y and Z refer to GSM coordinates (after Cowley 1981.).

magnetic field strength determined by Slavin et al., 1985 was 9.2 nT at this distance). These estimates attempt to find a ground state for the magnetotail, on which substorm activety is superimposed.

Plasma conditions in the magnetotail lobes have been extensively studied by Gosling, 1984 and Gosling et al., 1984, 1985. Thes studies found that the plasma distribution in the magnetotail lobes is asymetric, and depends on the sign of IMF By. This result is in agreement with predictions made in Jorgensen et al., 1972, Russell and Atkinson, 1973, and Cowley 1981. Figure 1.8) shows a schematic representation of a cross section of the distant magnetotail, for IMF By positive. The regions of preferential plasma entry through the magnetopause can be seen.

Sibeck et al., 1985 showed, by the examination of magnetopause crossings in the distant magnetotail, that the magnetotail is twisted. This twist is dependent on the direction of IMF By, as is predicted by Cowley, 1981. Figure 1.9) (after Cowley 1981) shows shows the theoretical twist in the magnetotail, for IMF By positive. Sibeck et al., 1985 also showed that, for strong IMF By, the magnetotail becomes flattened in the north-south direction, contrary to Tsurutani et al., 1984

who suggested that the magnetotail was elongated in the north-south direction.

The above work has shown that the earths magnetotail is a two lobe structure, extending to several thousand earth radii antisunward of the earth, separated by a magnetic neutral sheet, which is populated by energetic plasma. ISEE-3 based studies have shown that the magnetotail plays an important role in the dynamics of geomagnetic substorms, during which large (up to 100 R_E long) sections of the plasma sheet are ejected tailwards along the magnetotail as plasmoids.

Chapter 2

Instrumentation and analysis techniques.

The ISEE-3 payload.

The ISEE-3 spacecraft carried an integrated payload of instruments designed to study the solar wind and cosmic rays in orbit about the sun-earth Lagrangian point L_1. Only the instruments with a direct involvement in the present work will be described here, these include a vector helium magnetometer, a two dimensional plasma electron instrument, a plasma wave instrument and a three dimensional energetic proton anisotropy spectrometer (EPAS). These, and the remaining instruments, are detailed in IEEE Transactions on Geoscience Electronics vol GE-16 No. 3, July 1978.

The vector helium magnetometer was provided by the Jet Propulsion Laboratory, Pasedena, California (JPL) and its Principal Investigator is E.J. Smith. This instrument measures three orthogonal magnetic field components, with a maximum data resolution of 6 vectors per second. The data used in this study were provided in the form of 3 second average data plots, and numerical listings of 6 Hz data. This instrument is essentially identical to those carried by Pioneers 10 and 11, and further details can be found in Fransden et al., 1978.

The plasma electron instrument on ISEE-3 was provided by the Los Alamos National Laboratory (LANL); its Principal

Investigator is S.J. Bame. The plasma ion analyser on the plasma instrument failed in February 1980, and so for the entire duration of the Geotail mission plasma parameters were derived purely from the electron measurements. The electron energy range used by this instrument was from 5 eV to 2.5 keV, and measurements were taken in the plane perpendicular to the spacecraft spin axis, ie within 1^{O} of the GSE X-Y plane.

The plasma wave instrument was developed by TRW Systems Inc., and the Principal Investigator is F.L. Scarf. The instrument has 8 channels, with a 60 dB range, to detect magnetic field variations in the range 20Hz to 1kHz, and 16 80 dB channels to detect electric field variations in the range 20Hz to 100kHz. In this study data from the 16^{th} electric field channel, with a range of 56.2 to 100 kHz, were used as an indicator of auroral kilometric radiation, in the identification of substorm onsets (Voots et al., 1977).

Finally, the bulk of the analytical work presented here was carried out using data from the Energetic Proton Anisotropy Spectrometer (EPAS), carried on ISEE-3. The instrument design and construction was carried out by an international consortium, consisting of the Imperial College Cosmic Rays and Space Physics Group, London, The Space Science Department of ESA ESTEC, Noordwijk, The

Netherlands and the Space Research Laboratory of the University of Utrecht, The Netherlands. The Principal Investigator for this experiment is R.J. Hynds, Imperial College.

The EPAS instrument.

The EPAS instrument is designed to determine accurately the distribution function of protons in interplanetary space. In order to achieve this it is necessary to determine the angular distribution of proton fluxes and their energy spectrum. The energy range of the instrument is from 35 to 1600 keV; this range is divided into 8 logarithmically spaced, contiguous energy channels. The angular coverage of the instrument is provided by three particle telescopes, inclined at 30^{O}, 60^{O} and 135^{O} to the spacecraft spin axis. The use of several telescopes, each with a limited field of view, allows the determination of both azimuthal and polar variations in the particle distribution function (Sanderson and Hynds, 1977). Data are accumulated, for each energy channel, in 8 spin synchronized azimuthal sectors (only 4 sectors are used in the highest energy channel). The particular EPAS configuration of three telescopes allows the particle distribution function to be determined in terms of a spherical harmonic expansion, up to the second order. The nominal time resolution of

EPAS data is 16 seconds, however observations are spin synchronized, and each 16 second telemetry frame contains data accumulated over 5 or 6 spins (the spin period is approximately 3 seconds).

The choice of the number of telescopes, and their inclination to the spacecraft spin axis, was made in order to allow up to second order terms in the spherical harmonic expansion of the particle distribution function to be calculated. This means, that from EPAS data it is possible to calculate the omnidirectional ion flux (zeroth order term), the vector anisotropy (first order term) and the quadrupole anisotropy (second order terms), in each energy range of the instrument.

System design.

In a multi telescope system, small differences in the performance and construction of each telescope could lead to the observation of spurious anisotropies. In order to eliminate this problem each telescope should, ideally, be identical, and considerable effort was expended in minimizing differences between the three EPAS telescopes.

Discriminator	Proton threshold (keV)	Nominal dead layer (keV)	Nominally adjusted level (keV)	Event type derived
DA0	22	3.0	19	Noise + particles
DA1	35	4.0	31	Ions channel 1
DA2	56.5	5.0	51.5	Ions channel 2
DA3	91	5.0	86	Ions channel 3
DA4	147	4.0	143	Ions channel 4
DA5	238	3.0	235	Ions channel 5
DA6	384	2.0	382	Ions channel 6
DA7	620	1.0	619	Ions channel 7
DA8	1000	-	1000	Ions channel 8
DA9	1600	-	1750	α particles
DB	-		40	B-singles

Table 2.1 EPAS energy channel thresholds and associated discriminator levels. The nominal dead layers at each energy threshold are also shown. After van Rooijen et al., 1979.

Particle detectors.

The measurement of ion fluxes of a few tens of keV is facilitated by the use of silicon barrier detectors, since the amount of energy lost by a particle passing through the surface electrodes (the dead layer) is small (4 to 10 keV at proton energies of 50 to 90 keV). In most silicon barrier detectors the noise level, at room temperature, is too high to allow the accurate measurement of proton fluxes at 35 keV, hence the detectors must be cooled. This cooling is achieved, on the EPAS instrument, by use of a passive cold plate. This cold plate was at a temperature of -30 ^{O}C at launch, and was designed to operate at approximately -25 ^{O}C during the ISEE-3 mission.

One possible obstacle in the construction of three identical telescope systems is the variability of the detector dead layers. The dead layers of silicon barrier detectors are not predictable and so need to be determined experimentally. The silicon barrier detectors used in EPAS had one gold and one aluminium electrode on opposite sides, and each side exhibits different dead layer characteristics. The dead layers for each electrode were determined, and the gold electrode side of the detectors was found to have a lower dead layer than the aluminium electrode side. The dead layer, on the

gold electrode side, was also found to vary by less than ± 1 keV across the detector surface, and so it was decided that the EPAS detectors would be used with the gold electrode outwards. Table 2.1 (after van Rooijen et al., 1979) shows the EPAS energy channels, and the associated detector dead layers. The effects of radiation damage on the detector dead layers was examined, and it was found that after irradiation by 10^{13} protons/cm^2, of energy 10 keV, the dead layer increased by at most 1.5 keV (this level of irradiation is just less than that needed to cause electrical breakdown in the detectors). For the detector setup used in EPAS the dead layer was also found to be temperature independent.

Detector telescopes.

Figure 2.1 shows a schematic cross section of one of the three EPAS particle telescopes, whilst figure 2.2 shows a schematic diagram of the overall EPAS system (after van Rooijen et al., 1979). The major features of the telescope are, a light rejection collimator, an electron rejection magnet with anti scatter baffles, the detector stack, an in-flight calibration source, an amplifier chain for each detector and detector current monitoring circuits. The size and separation of apertures $ø_1$ and $ø_2$, seen in figure 2.1, define the counting geometry for particles in the EPAS energy range, and result in a

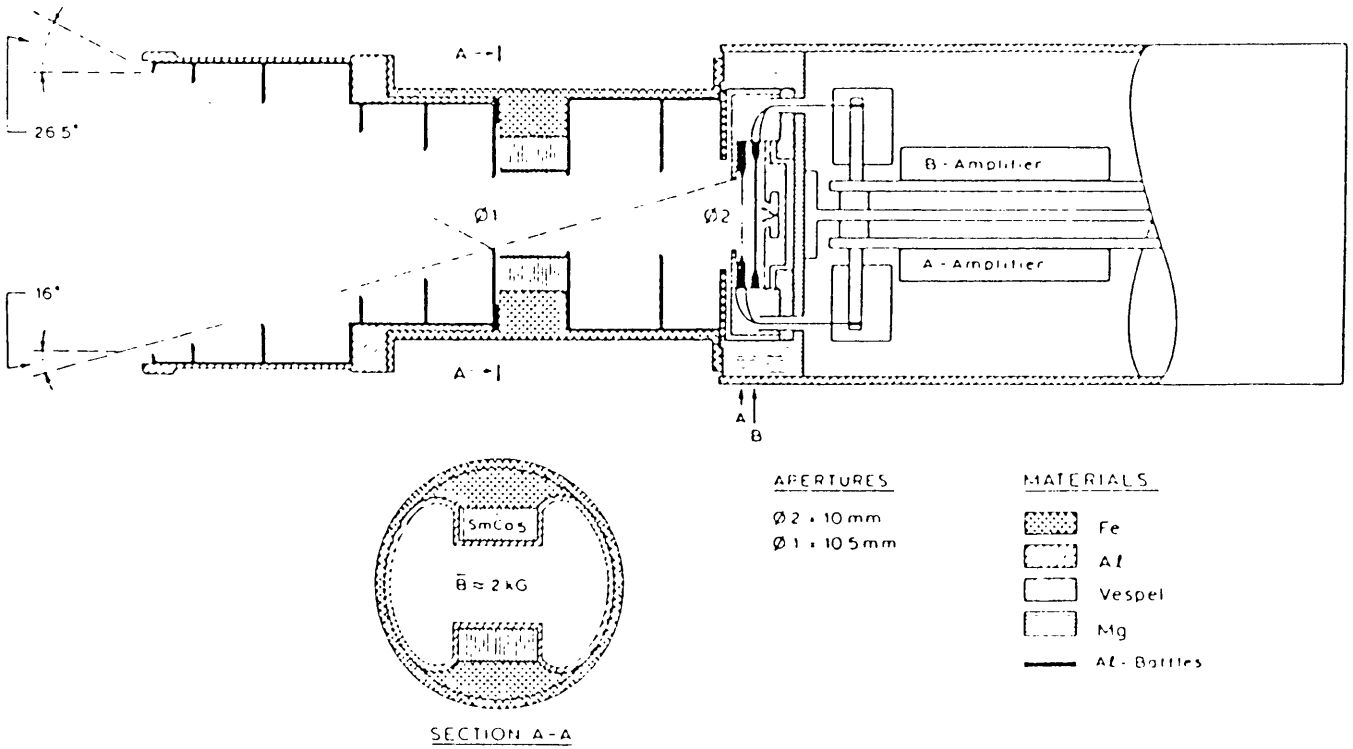


Figure 2.1 A schematic cross section of one of the EPAS telescopes. After van Rooijen et al., 1979.

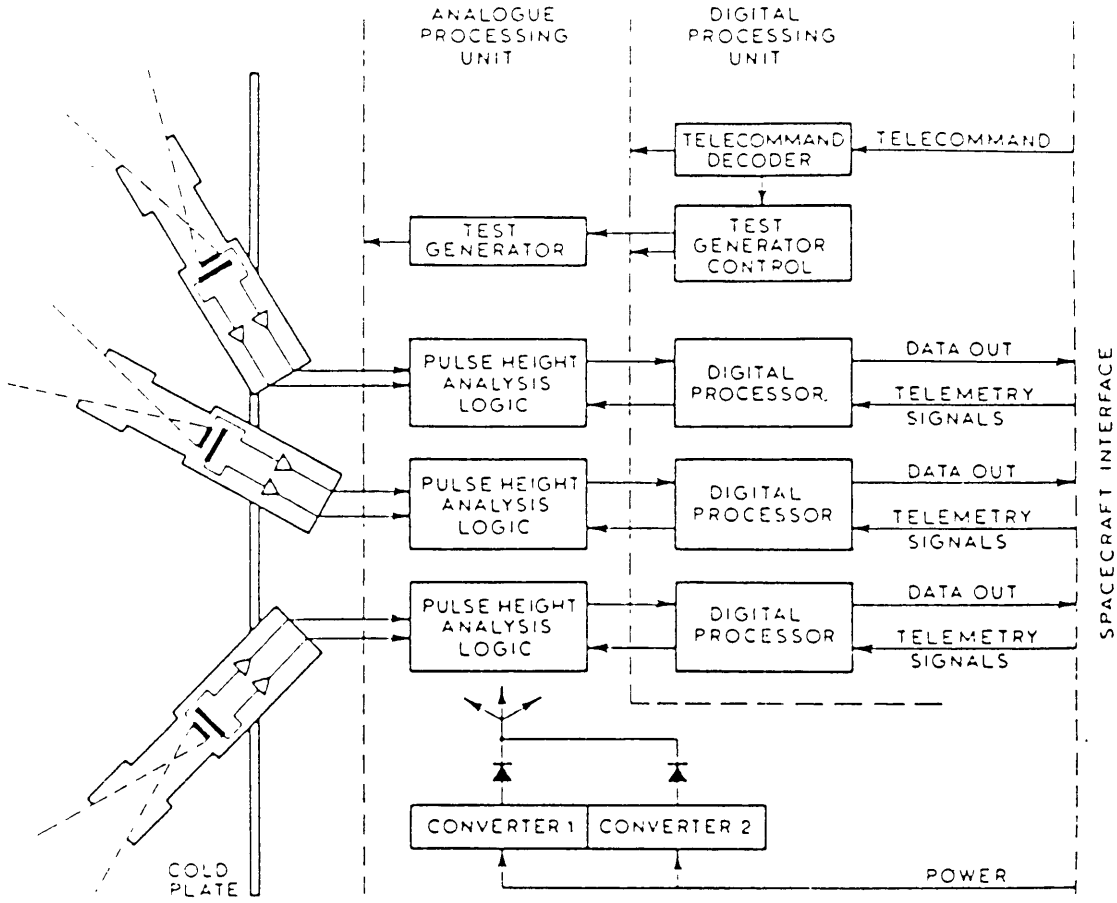


Figure 2.2 A block diagram of the overall structure of the EPAS experiment, showing the three independent telescope systems. After van Rooijen et al., 1979.

geometric factor, G, of 5×10^{-2} cm^2 sr. For high energy protons (of energy greater than 30 MeV) G approaches 2π times the detector area.

The detector stack comprises two silicon barrier detectors, A and B. The A detector is the outermost and has an effective area of 1 cm^2 with a thickness of 33 $\pm$ 1.5 μm. The B detector has an area of 2 cm^2 and is 150 μm thick; the detector spacing is 2mm. In the normal operation of the detectors particle counts are accumulated in anticoincidence mode, that is a count is registered if detector A is triggered and detector B is not triggered. The anticoincidence mode of operation allows active shielding of high energy protons (with energies above 30MeV), with an efficiency of around 90%. This mode of operation also defines the upper limit of the EPAS energy range.

The light rejection collimator is designed to eliminate directionally dependent noise, and any possible saturation of the detector system, caused by sunlight. The collimator effectively excludes sunlight, with a rejection factor of approximately 10^{-7}, provided that the spacecraft spin axis remains closely perpendicular (within 3^{O}) to the spacecraft earth line.

The electron broom magnets reject electrons with energies up to 400 keV entering the telescope viewing cone (rejection factors of better than 10^{-4} have been achieved for electron energies below 150 keV). Above 400 keV some increase in detector response is expected, but these electrons are expected to pass through the thin A detector triggering the B detector, and so can be eliminated through the anticoincidence operation of the detector stack. The broom magnets also eliminate protons with energies less than 1 keV.

The in-flight calibration source is the beta particle emitter, Cl^{36}, with an activity of approximately 50 nCi. The source is situated at the back of the B detector, on each telescope.

The amplifier chains for each detector were produced as thin film hybrids and positioned close to the detectors (figure 2.1). The required noise bandwidth of 12.5 keV, was achieved by operating the telescopes at -25 ^{o}C, and by the inclusion of an electric shield which surrounds the detectors and amplifier inputs. The outputs from the amplifier chains are fed into the pulse height analysis logic, here 11 pulse height discriminators are used to define the 8 energy channels. A noise channel is also defined which corresponds to protons in the 22-35 keV energy range. Counts in the individual energy ranges are

then passed to the data processing unit (DPU), which accumulates the counts corresponding to the eight azimuthal spin sectors. The noise channel data is also sectored, but with a reduced time resolution of 128 seconds; this serves two purposes, firstly any directional dependence of the system noise may be determined, and secondly, if the system noise remains small (less than 13 keV) and the proton fluxes are sufficiently large, the noise channel can be used to extend the energy range of EPAS down to 22 keV. Events triggering the highest energy threshold in the A detector (DA9 in table 2.1), in anticoincidence with the B detector are also accumulated as a measure of the alpha particle flux at energies greater than 1750 keV. Events triggering the B detector alone, and the total coincidence rate between the A and B detectors are also accumulated. These last three event types are recorded with a time resolution of 64 seconds.

Other possible sources of contamination in the proton energy channels.

High energy particles are mainly rejected by active shielding, in the normal anticoincidence mode, however, the trajectories of some particles may take them through the A detector but not the B detector. The rejection of such particles is provided, to a large extent, by passive

shielding, accomplished by choosing the telescope walls to be sufficiently thick. Large fluxes of high energy electrons capable of penetrating the telescope walls (energy greater than 4 MeV) may cause some contamination in the lowest energy channel, but this effect can, again, be predicted from the count rate in the B detector. The effect of solar X-ray bursts is expected to be negligible, because of the low detection efficiency of silicon barrier detectors. Any large X-ray flux may, in any case, be inferred from the count rate in the B detector.

Analysis techniques.

The method of analysis of EPAS data in this work is somewhat different to that employed in studies during the solar wind phase of the ISEE-3 mission; the full spherical harmonic analysis is not used to represent the data. Instead, use is made of the zeroth order spherical harmonic term, which is the omnidirectional ion flux, and further information is obtained about the particle distribution by considering the counts registered in individual telescope-sector combinations. This type of analysis is facilitated by knowledge of the overall geometry of the magnetotail, and in particular the orientation of the lobe magnetic field allows us easy access to a part of the ion pitch angle distribution.

As ISEE-3 spins about its axis each EPAS telescope sweeps out 8 azimuthal sectors. This will produce in total 24 viewing directions. Sectors 3 and 7 of each telescope will view in the GSE Y-Z plane (sector 3 towards dusk sector 7 towards dawn in the geotail). This means that for an earthward or tailward directed magnetic field (as in the magnetotail lobes) there will be 6 viewing directions which can see ions with a pitch angle of 90^0. Figure 2.3a (after Murphy et el., 1987) shows the three telescope directions which view in the positive GSE Y direction in the GSE Y-Z plane, and which correspond to sectors (1,3), (2,3) and (3,3). (ie telescope 1, sector 3 etc.). In the northern tail lobe, that is with the magnetic field directed earthward, these three sectors will detect ions with pitch angle 90^0 whose gyrocentres are above a plane parallel to the ecliptic plane, and passing through ISEE-3. Figure 2.3b (after Murphy et al., 1987) shows the corresponding three telescope directions which view in the direction of negative GSE Y in the GSE Y-Z plane, ie sectors (1,7), (2,7) and (3,7). In this case these sectors,in the northern tail lobe, will always detect ions of 90^0 pitch angle whose gyrocentres are below a plane parallel to the ecliptic plane, and passing through ISEE-3. The gyrocentres for ions of energy 45.5 keV (the centre of the lowest energy channel) entering the telescopes viewing in the GSE Y-Z

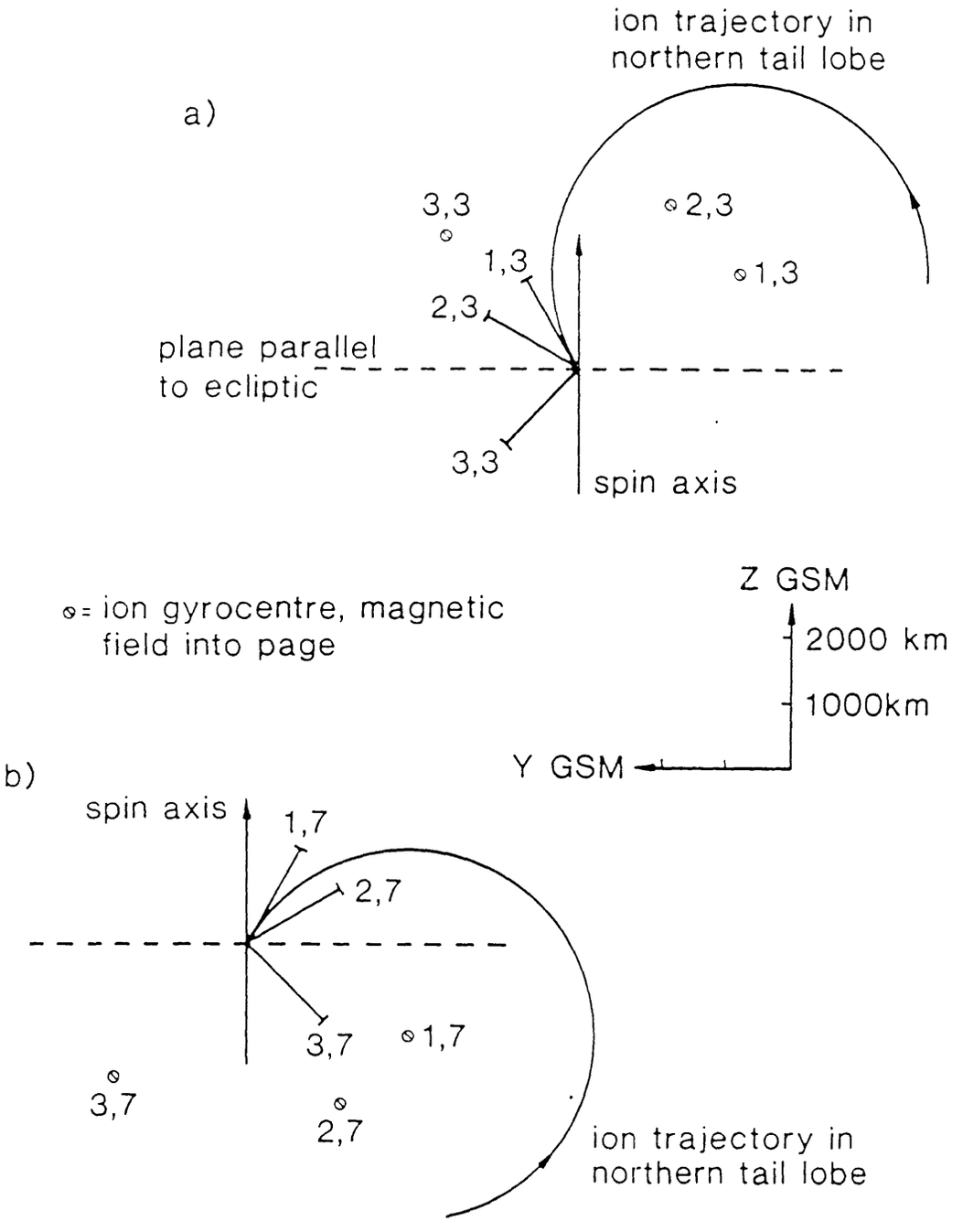


Figure 2.3 (a) The three telescope directions which view in the positive GSE Y direction, in the GSE Y-Z plane, corresponding to telescope sectors (1,3), (2,3) and (3,3) (ie, telescope 1, sector 3, etc.). The magnetic field is into the page. (b) The three telescope directions which view in the negative GSE Y direction, in the GSE Y-Z plane, corresponding to telescope sectors (1,7), (2,7) and (3,7). Again the magnetic field is into the page. In each case the three telescope sectors will see ions with pitch angles close to 90^{o}. After Murphy et al., 1987.

plane are shown, together with a sample ion trajectory, in each of the diagrams 2.3a and 2.3b.

Ions which have large pitch angles have been used to probe density gradients and boundary layers in many previous studies (eg., Andrews et al., 1981; Fritz et al., 1982; Daly et al., 1983, 1984 and Richardson and Cowley, 1985). In this work we use this technique in two ways. Firstly we are able to determine the orientation of density gradients and boundary layers, even if ISEE-3 does not completely cross the boundary in question. This can give us a useful insight into the geometry of the plasma regimes under consideration. Secondly, during the passage of ISEE-3 through an region of increased plasma density we can use the differences in the times at which a particular ion intensity is seen in each of the sectors in the GSE Y-Z plane to calculate the velocity of the plasma boundary relative to ISEE-3 (Richardson and Cowley, 1985).

In order to obtain information on the ion fluxes streaming along the magnetic field direction in the tail lobes, ie with pitch angles close to 0^0, measurements from telescope 2 sectors 1 and 5 were used (ie (2,1) and (2,5)). Sector (2,1) views at 30^0 above the ecliptic plane and will detect ions moving in the direction of negative GSE X, ie tailward streaming ions. Sector (2,5)

again views at 30^{O} above the ecliptic plane, but detects ions moving in the direction of positive GSE X, ie earthward streaming ions. Streaming ion data can give two possible pieces of information; in the plasma sheet, for example, where it is possible to assume that the rest frame ion distribution is isotropic (Daly et al., 1985) we can use the magnitudes of ion fluxes seen in sectors (2,1) and (2,5) to infer whether the bulk ion flow is earthward or tailward; in regions where the ions are obviously streaming along the magnetic field, eg, in the plasma sheet boundary layer, it is possible to determine the direction from which ions are being accelerated, and so infer the local magnetic field topology (ie, if the ions are streaming earthwards in the plasma sheet boundary layer it can be assumed that ISEE-3 is earthward of an active reconnection line and so on closed magnetic field lines).

The use of 90^{O} pitch angle ion fluxes allows us to derive information about both the magnetotail structure, local to ISEE-3, and the dynamics of that structure. Fluxes of ions with pitch angles close to 0^{O} or 180^{O}, allow us to make inferences about the bulk plasma flow, or, in certain cases, the local magnetic field topology.

CHAPTER 3

Travelling compression regions in the magnetotail lobes

Introduction

During the period of the geotail mission ISEE-3 observed a class of magnetic field compressions which occurred in the magnetotail lobes. These compressions lasted from 2-20 minutes, showed a 10%-30% increase in magnetic field strength and were found to be associated with substorms (Slavin et al. 1984). The characteristic signature of these Travelling Compression Regions (TCRs) was that the magnetic field tilted first northward and then southward, with the point of inflection near the maximum in magnetic field strength. Figure 3.1 shows the magnetic field data for a clear example of such a compression, which occurred on April 14 1983 (Day 104) at approximately 0315 UT, whilst ISEE-3 was 78 R_E tailward of the earth (this TCR is the largest recorded, in this data set, with a compression ratio of 30%). The maximum in the magnetic field magnitude is marked with a vertical line and, as can be seen, this maximum coincides with the point of inflection of a bipolar signature in Theta, the polar angle of the magnetic field. TCRs were interpreted by Slavin et al. as being the magnetotail lobe signatures of closed magnetic field regions (Plasmoids) released during substorm activity and propagating along the magnetotail, away from the earth.

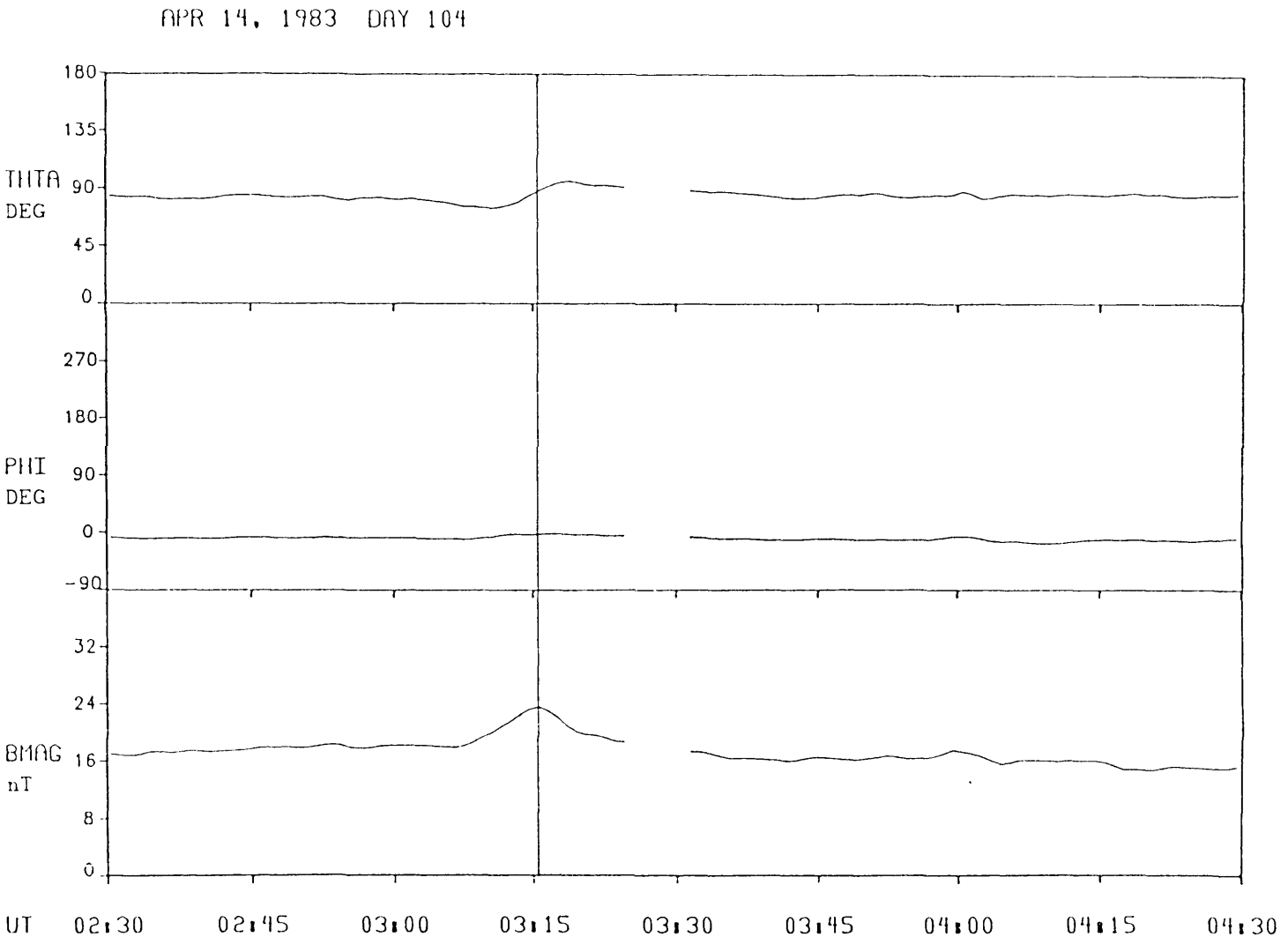


Figure 3.1. Magnetic field magnitude BMAG, polar angle THTA, and azimuthal angle PHI, in GSM coordinates, between 0230 and 0430 UT on April 14th 1983. The time of peak TCR compression is marked with a vertical line.

Geomagnetic data

In order to investigate the validity of Slavin's model of TCR's it is necessary to have some indicator of geomagnetic activity which we can relate to the detection of TCR's at ISEE-3. The parameter chosen for this study was the geomagnetic substorm onset time. The substorm onset time was used for two reasons, it is the most readily measured substorm parameter and it relates directly to the release of plasmoids in the magnetotail (Hones et al., 1984). Two methods of substorm onset timing are used in this study; auroral kilometric radiation (AKR) detected by the wave experiment on ISEE-3 (Voots and Gurnett, 1977) and Pi2 pulsations, detected by the Air Force Geophysical Laboratory (AFGL) mid latitude magnetometer network (Singer et. al. 1983).

AKR is electromagnetic radiation in the hundred kHz range, and although its generation mechanism is still unclear, its occurrence has been linked to the onset of geomagnetic substorms (Voots and Gurnett, 1977). The highest frequency band on the ISEE-3 wave instrument is at 100 kHz and so it is ideally suited to the detection of AKR. This method of substorm timing was used successfully in the TCR study by Slavin (Slavin et al. 1984) in conjunction with ground based magnetometer measurements and geosynchronous particle data. The main

method of substorm onset timing used in the present study is AKR. However, this is backed up in some cases by the use of Pi2 pulsations detected by the AFGL mid latitude magnetometer network. Pi2 pulsations are damped irregular waves seen in magnetograms. They have periods between 40 and 150s, and have long been associated with substorm onsets (Saito, 1969., Sakurai and Saito, 1976.) Using the formal definition of a geomagnetic substorm (Rostoker et al., 1980.) a substorm must include at least one Pi2 pulsation at its onset.

Properties of TCRs, as determined from the magnetic field and Geomagnetic data.

The TCR data set used in this study consists of 54 events taken from the first deep tail pass of ISEE-3 (between October 1982 and April 1983). The TCRs used to compile this data set are not all discrete events, in fact, approximately 50% of them consist of multiple compressions. In the events with multiple compressions, only the first TCR is used in this analysis, thus ensuring that the properties measured are relative to the pre-substorm lobe conditions. From consideration of the magnetic field data we can make two measurements concerning a TCR; the duration and the compression ratio. The latter is defined as the ratio of the peak magnetic field strength in the compression to the magnetic field strength before the compression. These two measurements serve to characterize the local properties of the TCR.

In 35 of the 54 events we can also ascribe a substorm onset time to the event, from which we can deduce a time delay between the substorm onset and the TCR observation. In the other events geomagnetic data is usually too disturbed to give a clear onset time. In order to interpret this delay we must make some assumptions about the substorm process; firstly we assume that the substorm reconnection point is at -20 R_E GSM X; secondly we assume

that the time between substorm onset and detection of AKR, and Pi2 pulsations, is negligible compared with the time delay between substorm onset and TCR detection; thirdly we assume that the plasmoid is released at the time of the substorm onset. Using the above assumptions and the measured substorm-TCR delay times we can calculate a time of flight velocity for each TCR, and using this velocity together with the TCR duration we can calculate a TCR length. The first assumption is unavoidable, as it is not possible to locate the reconnection point for each substorm, but will lead to errors in the calculation of the TCR velocity, especially for TCRs seen close to earth. The second and third assumptions will lead to errors in the measured substorm-TCR delay time, but their effects will be in the opposite sense, and so tend to cancel each other out.

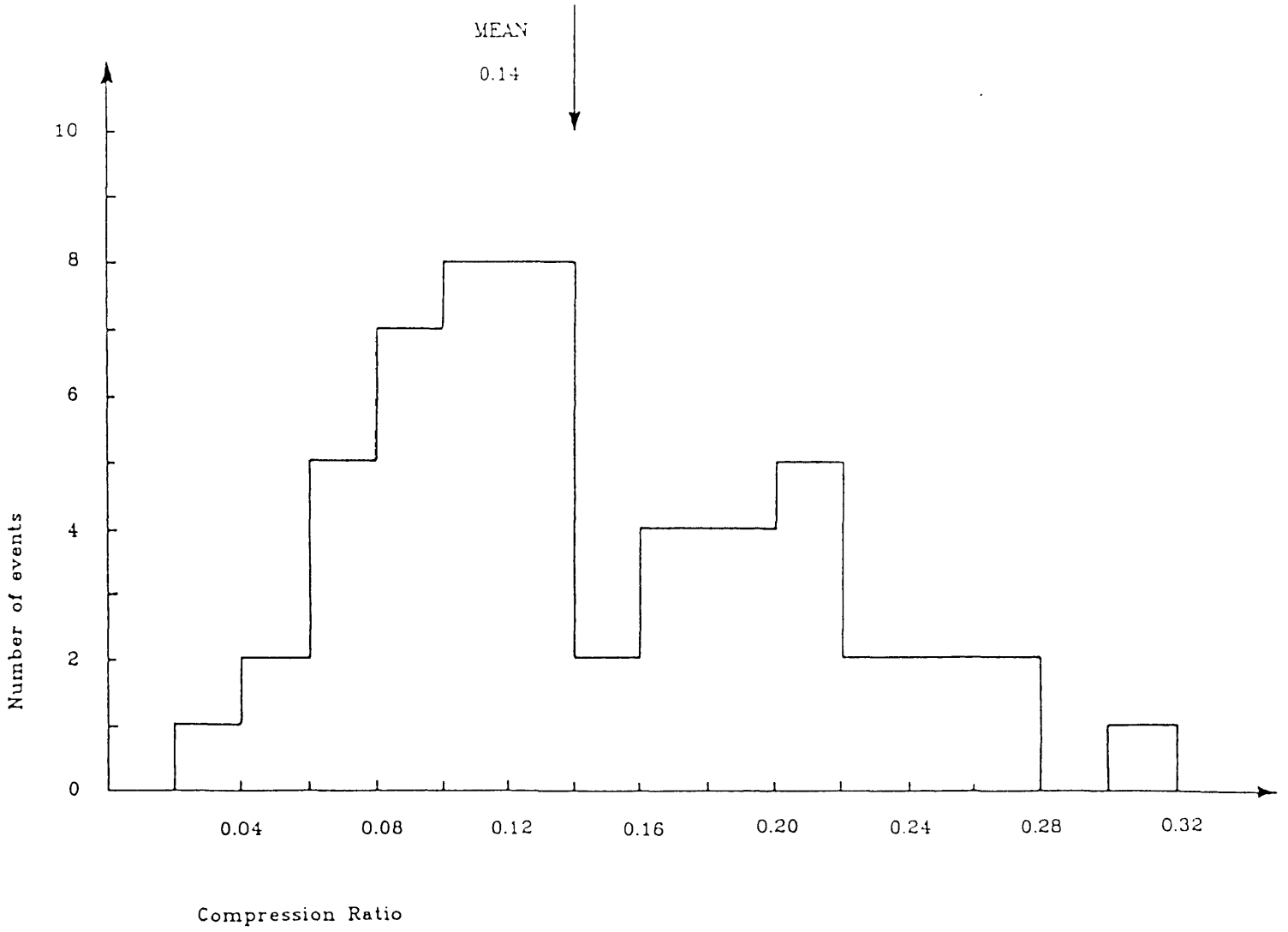


Figure 3.2a. Frequency histogram of TCR compression ratio. The average compression ratio is marked.

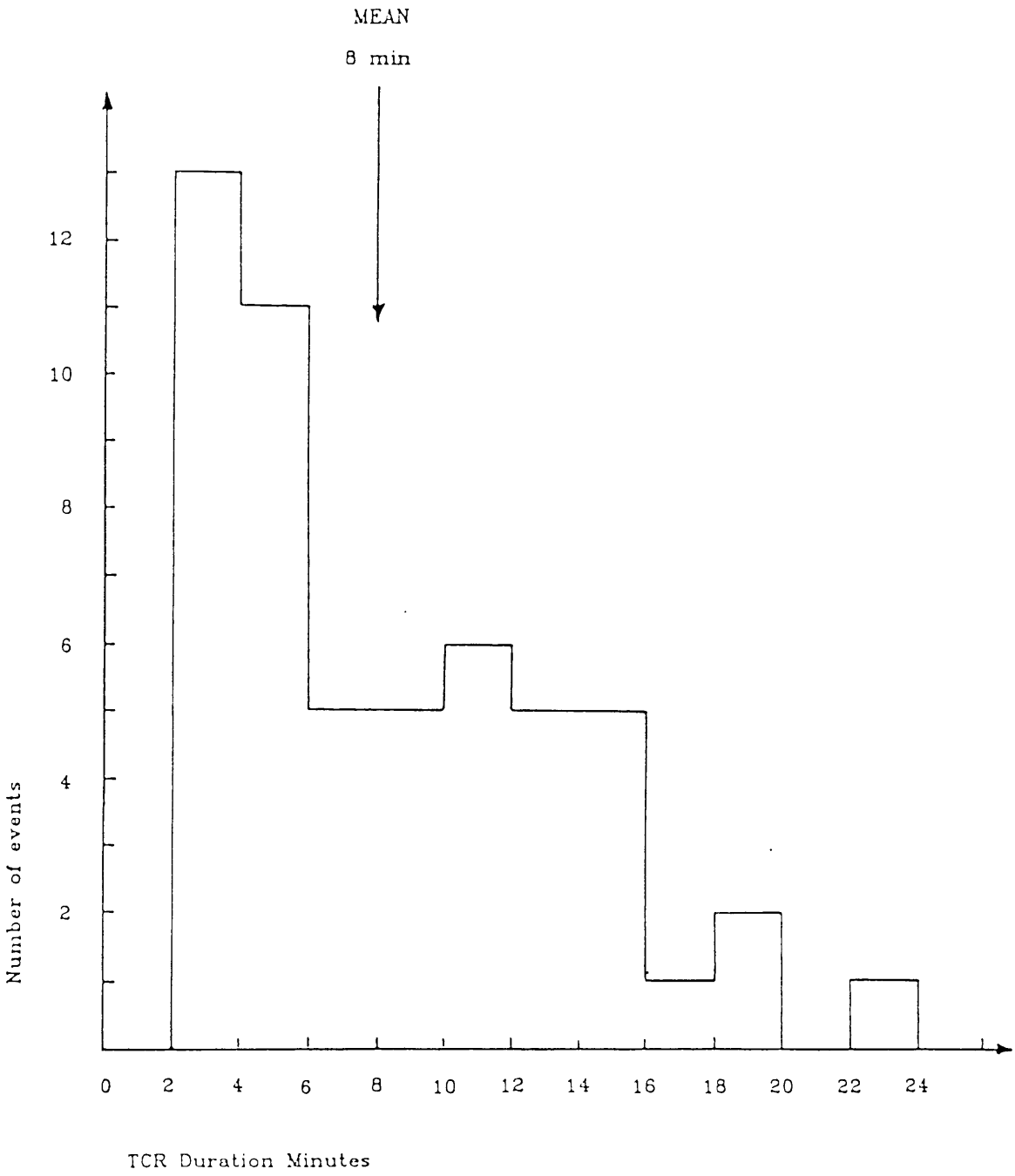


Figure 3.2b. Frequency histogram of TCR duration, in minutes. The average duration is marked.

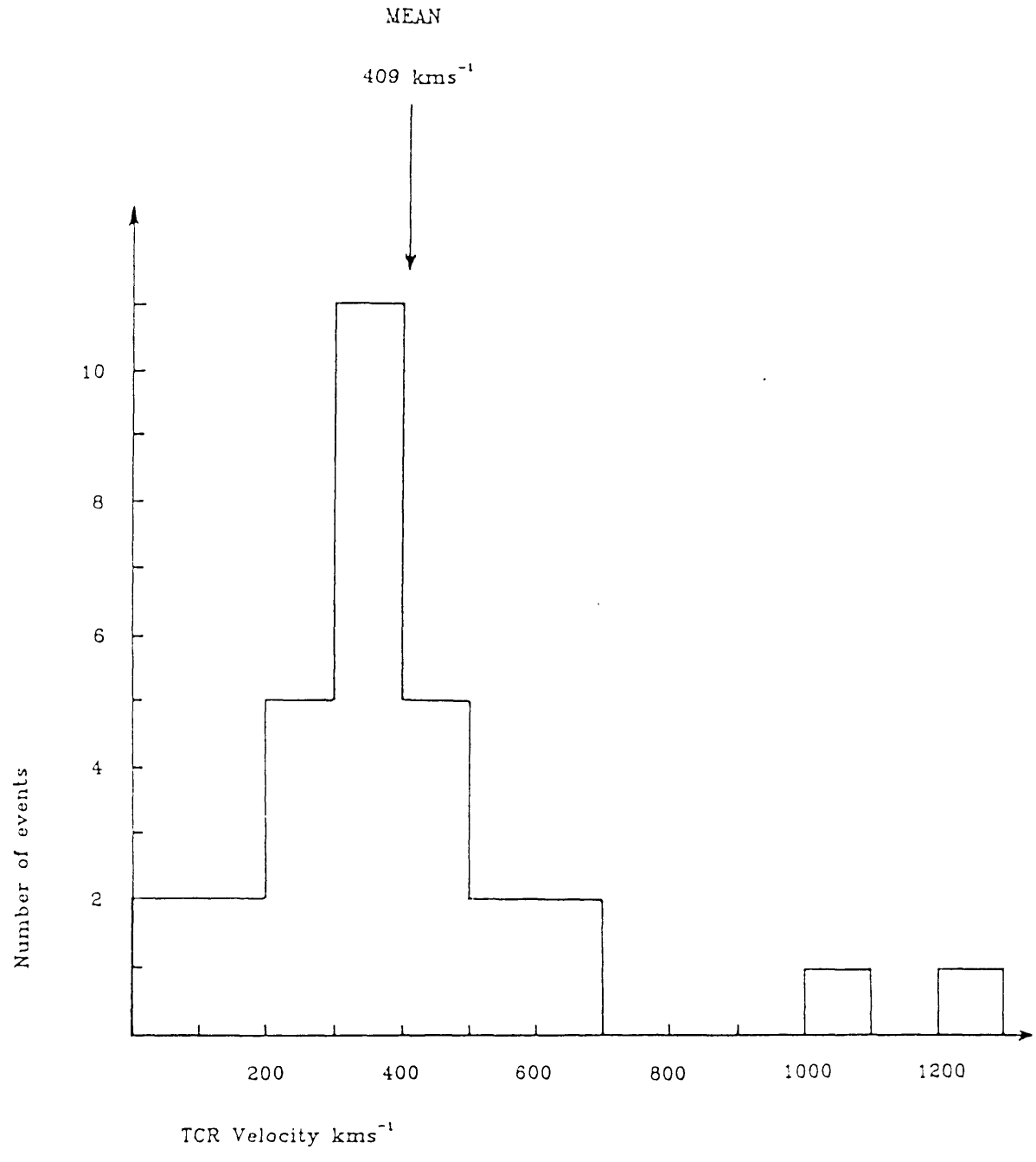


Figure 3.2c. Frequency histogram of TCR tailward velocity, in kms^{-1}, derived from time of flight calculation. The average velocity is marked.

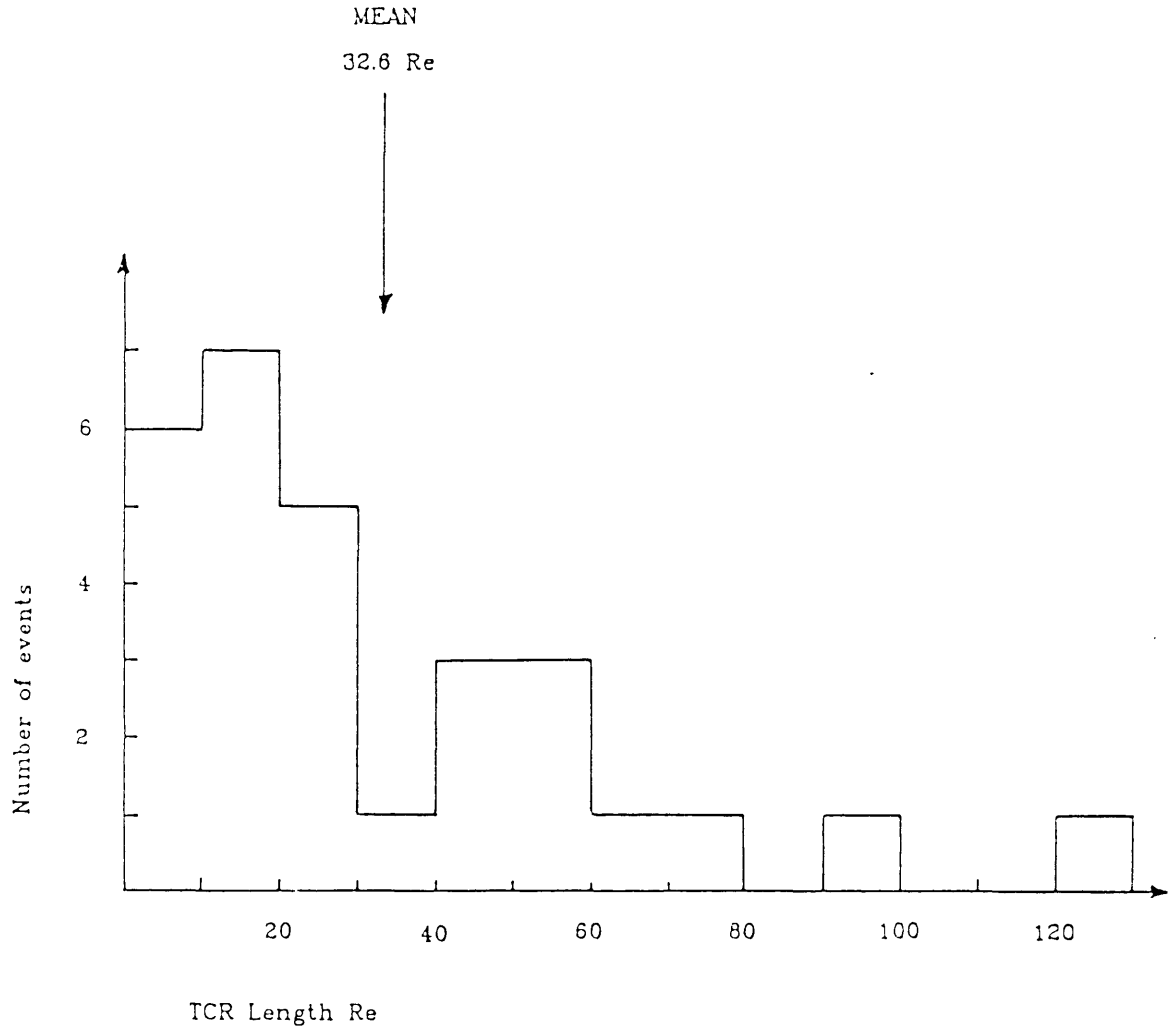


Figure 3.2d. Frequency histogram of TCR length, in R_E, derived from duration and time of flight velocity. The average value is marked.

Frequency distribution of TCR properties

Figures 3.2a), b), c) and d) show frequency histograms of TCR compression ratio, duration, tailward velocity and length respectively. The histograms of compression ratio and velocity (Figures 3.2a and c) show distributions which would be expected from the random sampling of data, that is, there is a peak at approximately the position of the mean, as would be expected with a normal distribution. The distributions shown for TCR duration and length (Figures 3.2b and d), however, have a markedly different form from that which would be expected for a normal distribution of data samples. As the TCR length is calculated from the duration we can consider the distribution of TCR durations to be the cause of this anomaly. Two possible causes of the asymmetry in figure 3.2b) are that we are not sampling the full range of TCR durations, ie, the selection procedure has excluded TCRs of very short duration, or that we are in fact sampling two distributions of data with different causes. This point will be dealt with later.

Variation of TCR properties with position

In order to examine how the properties of TCRs vary with position it is first necessary to choose a coordinate

system in which to express the position. A commonly used coordinate system in magnetospheric studies is the Geocentric Solar Magnetospheric (GSM) coordinate system. This system has the earth at its centre and the X axis pointing in the direction of the sun. The GSM Y and Z directions define a plane at right angles to the X direction, the Z direction is a projection of the earths magnetic dipole onto this plane, and the Y direction is chosen so as to form the third vector in a right handed system (ie, it will point approximately in the duskward direction). This choice of coordinate system means that the Y and Z directions will 'wobble' about X as the earth rotates. The GSM coordinate system has a major limitation when used to order data in the earth's magnetotail; due to the earths orbital motion about the sun the magnetotail is aberrated away from the GSM X line in the X-Y plane. The angle of this aberration is usually estimated to be on average 4^{O} in the direction of negative Y. For analysis of data collected in the distant magnetotail the effect of this aberration is large ($14R_E$ at GSM X = $-200R_E$, compared with a mean tail radius of $30R_E$ at this distance.) and so must be compensated for. To do this the position of the spacecraft is first expressed in GSE, then the coordinates are aberrated in the GSE Y direction (which is in the ecliptic plane), this aberrated GSE is then rotated about the new GSE X axis so that the Z axis is

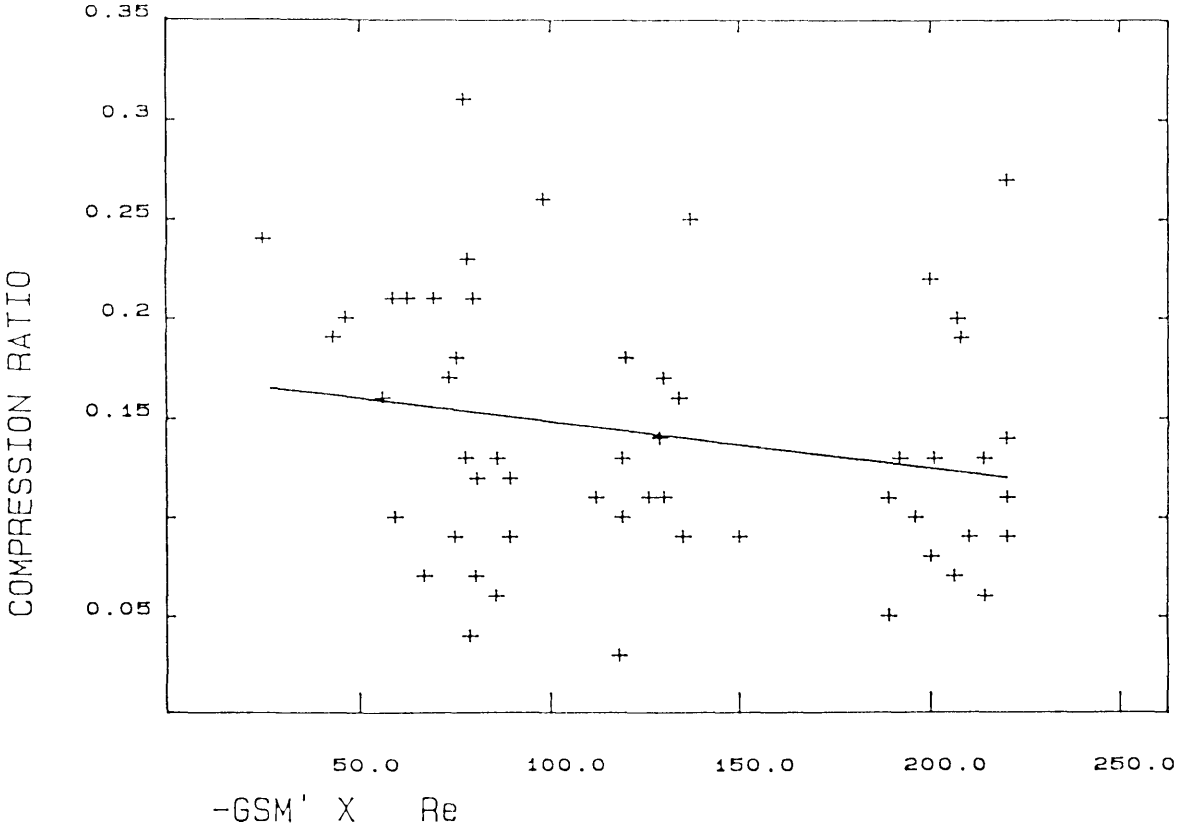


Figure 3.3a. TCR compression ratio, plotted against -GSM' X, in R_E. Linear regression gives a correlation coefficient, r, of -0.22 from 54 points. The regression line is shown.

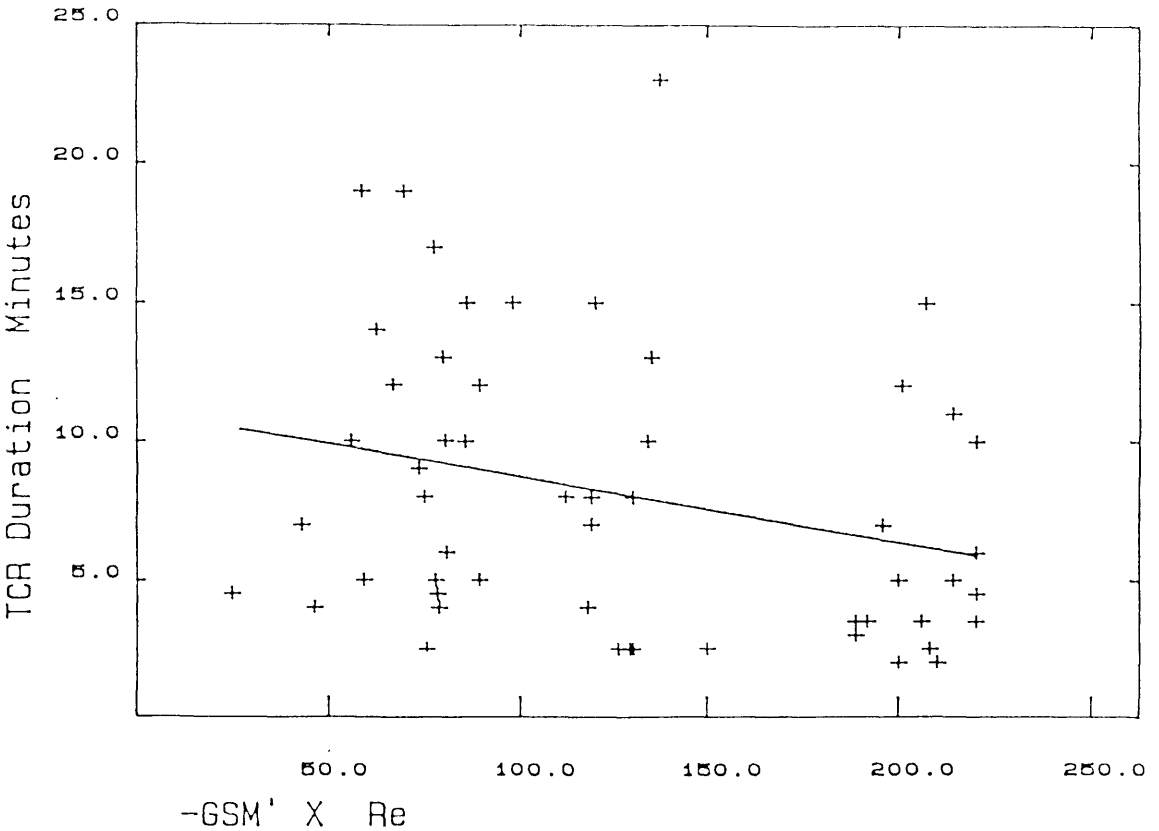


Figure 3.3b. TCR duration, in minutes, plotted against -GSM′ X, in R_E. Regression analysis gives r=-0.27 from 54 points. The regression line is shown.

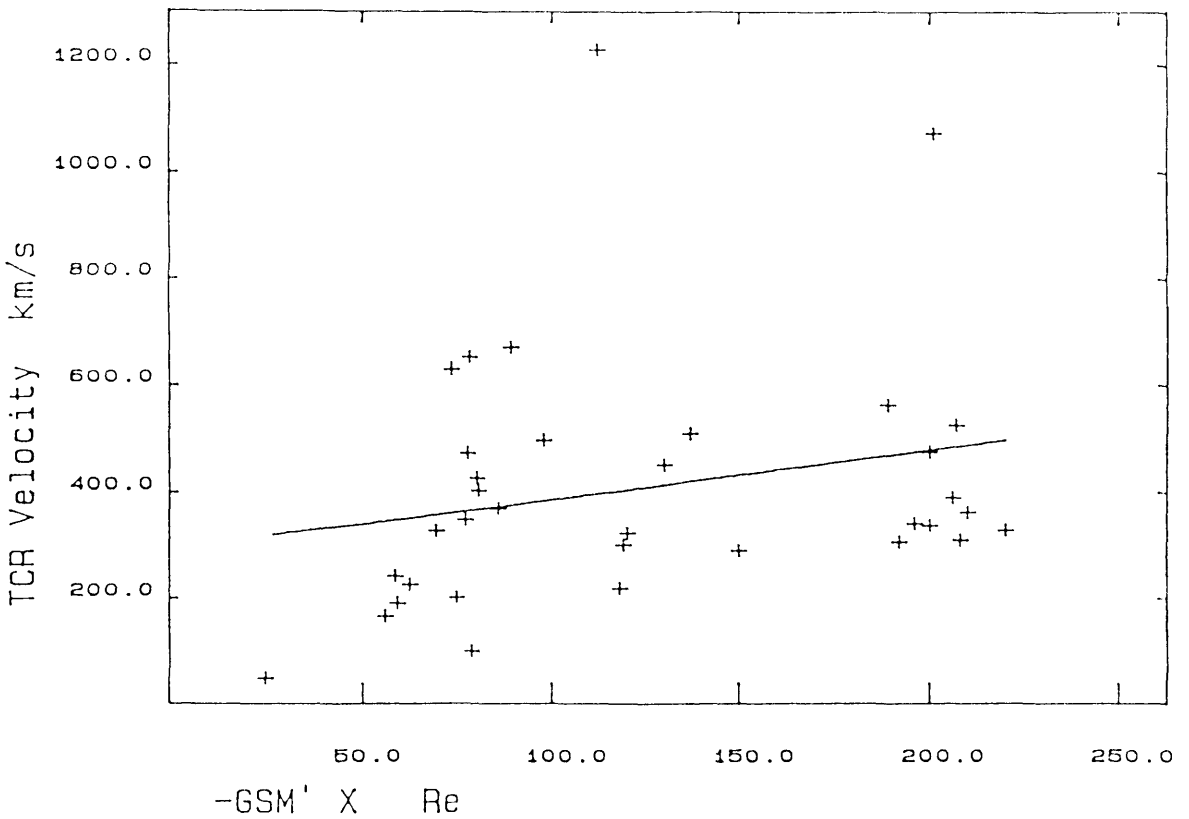


Figure 3.3c. TCR time of flight velocity, in kms^{-1}, plotted against -GSM' X, in R_E. Regression analysis gives r=0.23 from 35 data points. The regression line is shown.

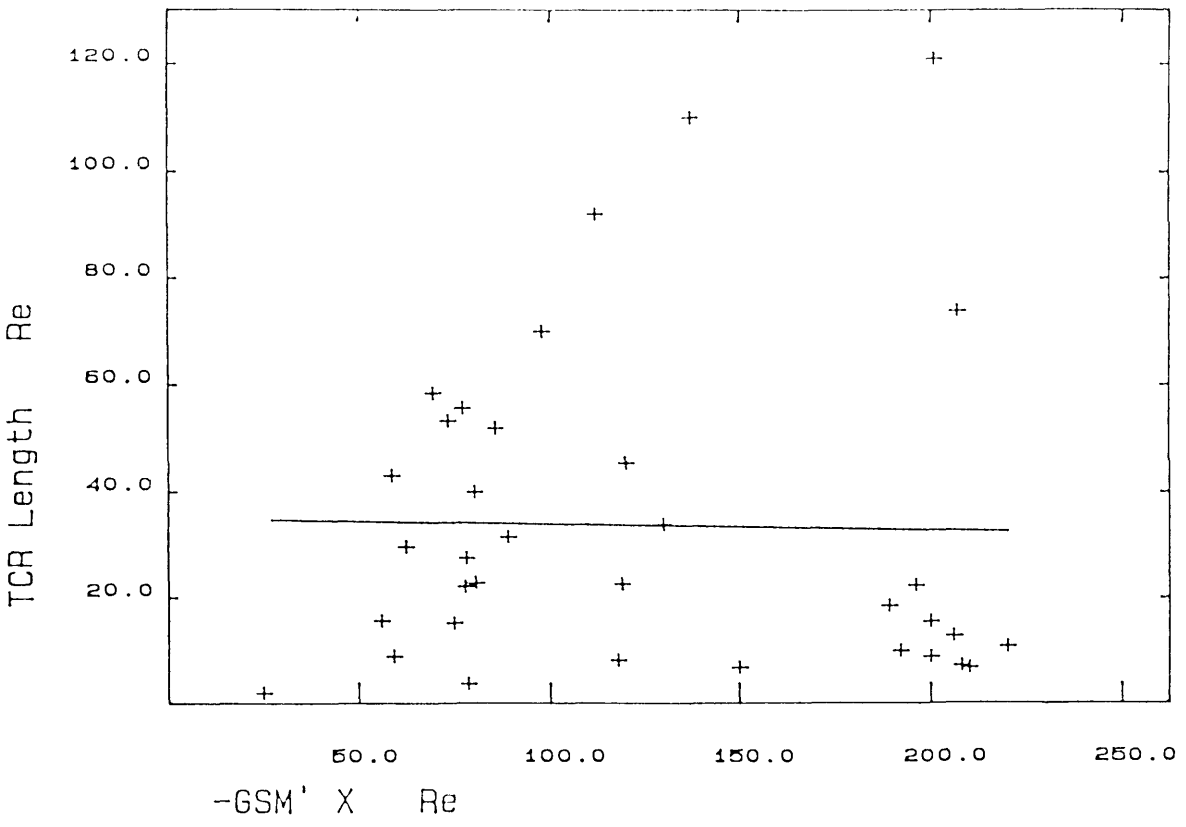


Figure 3.3d. TCR length, in R_E, plotted against -GSM' X, in R_E. Regression analysis, from 35 data points, gives r=-0.02; the fitted line is shown for reference.

aligned with the earths magnetic dipole. The resultant coordinate system is an aberrated GSM system and will be denoted by GSM'.

Figures 3.3a), b), c) and d) show various TCR properties plotted against -GSM' X. Figure 3.3a) shows compression ratio plotted against -GSM' X. There is a large amount of scatter in the data and regression analysis gives a correlation coefficient of r = -0.22, which is only significant at the 10% level. From this we can imply no trend in compression ratio with GSM' X. Figure 3.3b) shows TCR duration (Dt) plotted against -GSM' X. Regression analysis of this data gives r = -0.27, which is just significant at the 5% level, this implies that there is a trend for TCR duration to be shorter at larger distances downtail. Figure 3.3c) is a plot of TCR tailward velocity (Vx) against -GSM' X. The regression coefficient for this plot is 0.23, which for 35 points is only significant at the 15% level, and so from this we can deduce no relationship between -GSM' X and Vx. On examination of the plot we can see that the main cause of this lack of correlation is the large amount of scatter in Vx for GSM' X between -50 and -100 R_E, this is of course the region in which the most error in measurement of the TCR velocity will occur. Figure 3.3d) shows TCR length plotted against -GSM' X, and again, from this plot

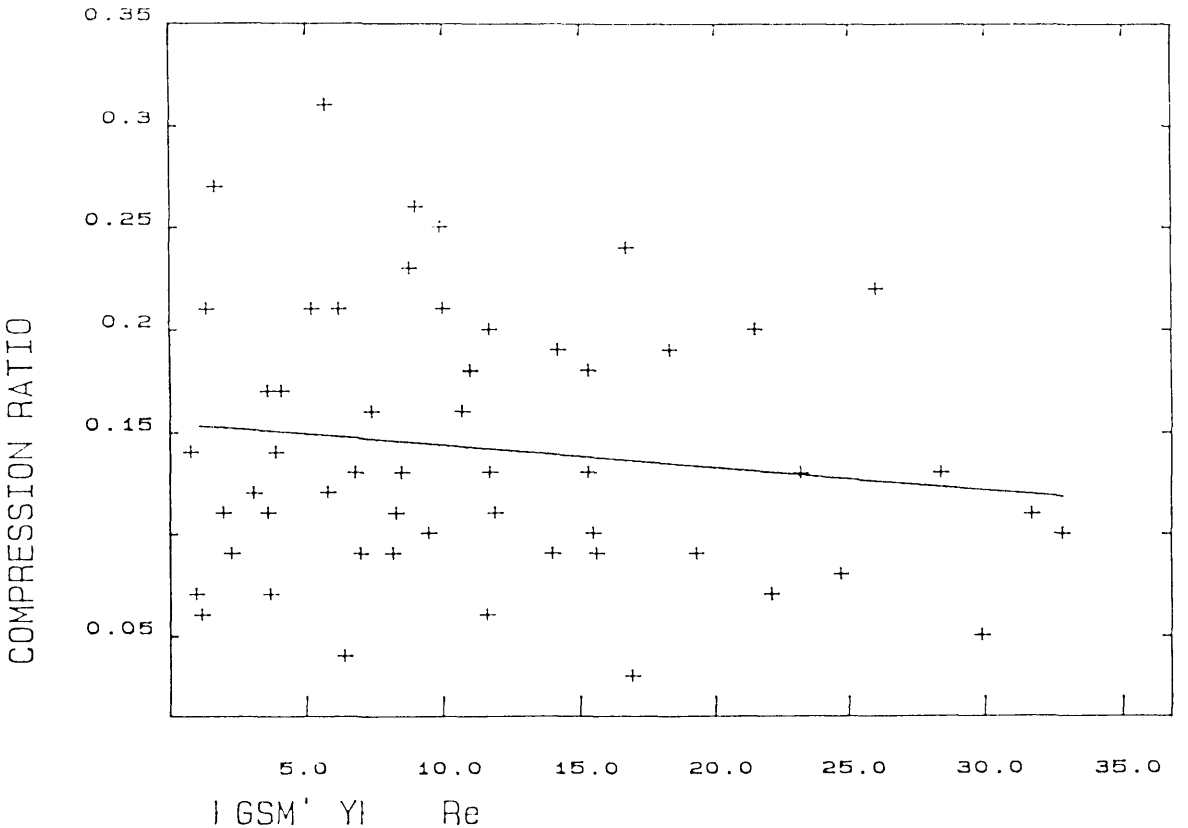


Figure 3.4a. TCR compression ratio, plotted against |GSM' Y|, in R_E. Regression analysis gives r=-0.14 from 54 points. The fitted line is shown.

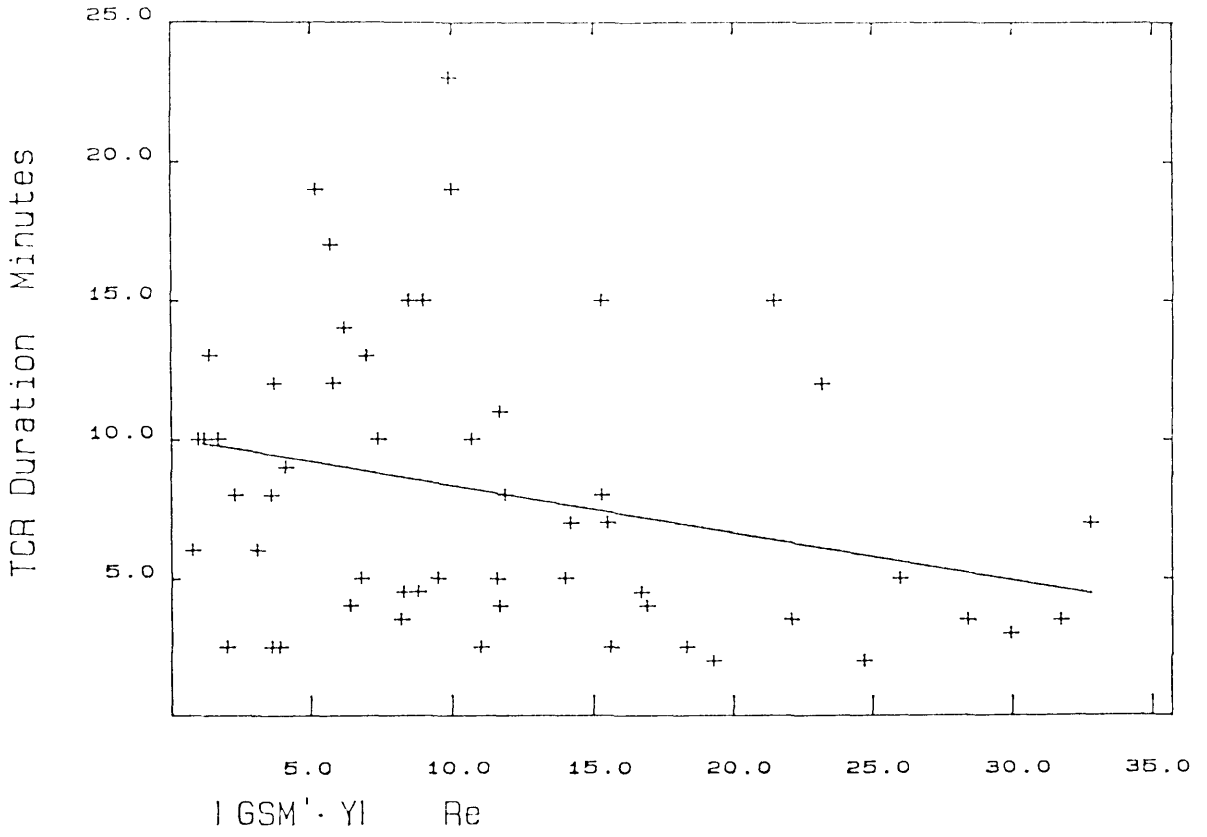


Figure 3.4b. TCR duration, in minutes, plotted against |GSM' Y|, in R_E. Regression analysis gives r=-0.28 from 54 points. The fitted line is shown.

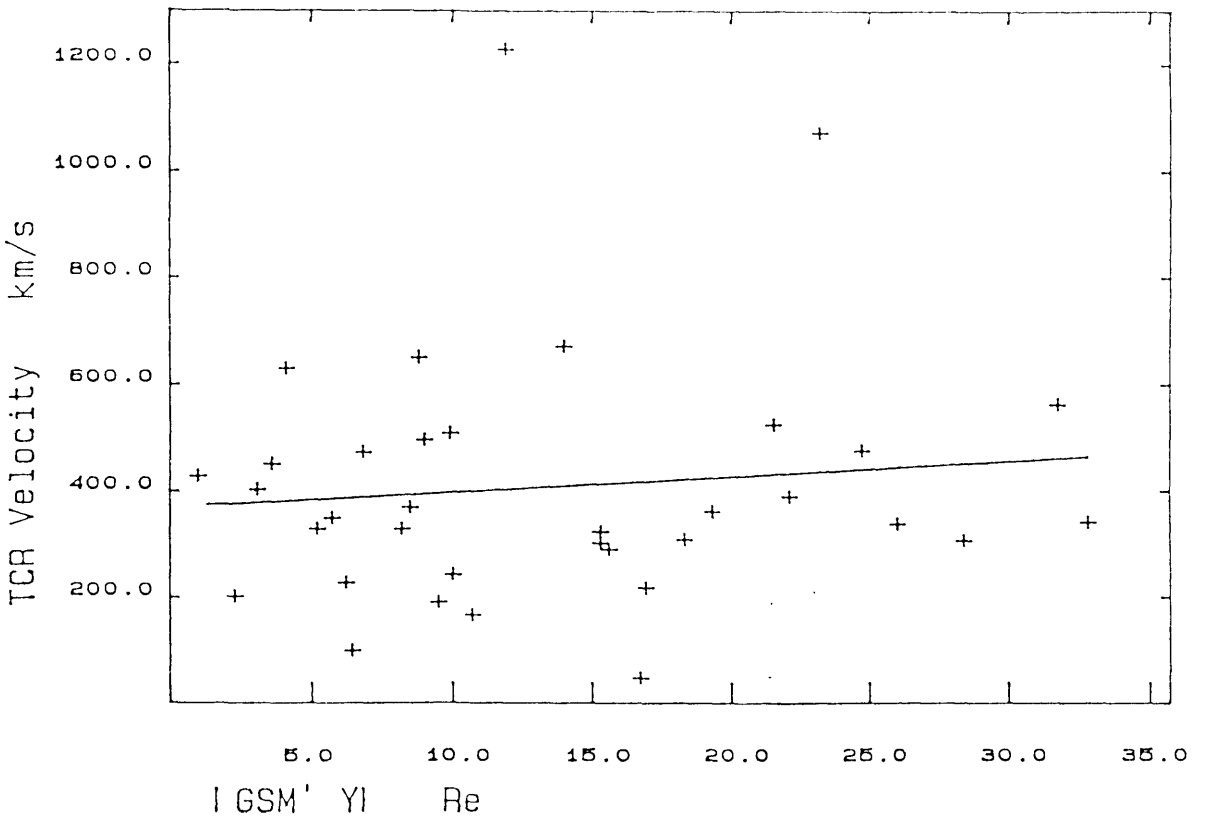


Figure 3.4c. TCR time of flight velocity, in kms^{-1}, plotted against |GSM' Y|, in R_E. Regression analysis gives r=0.11 from 35 data points. The regression line is shown.

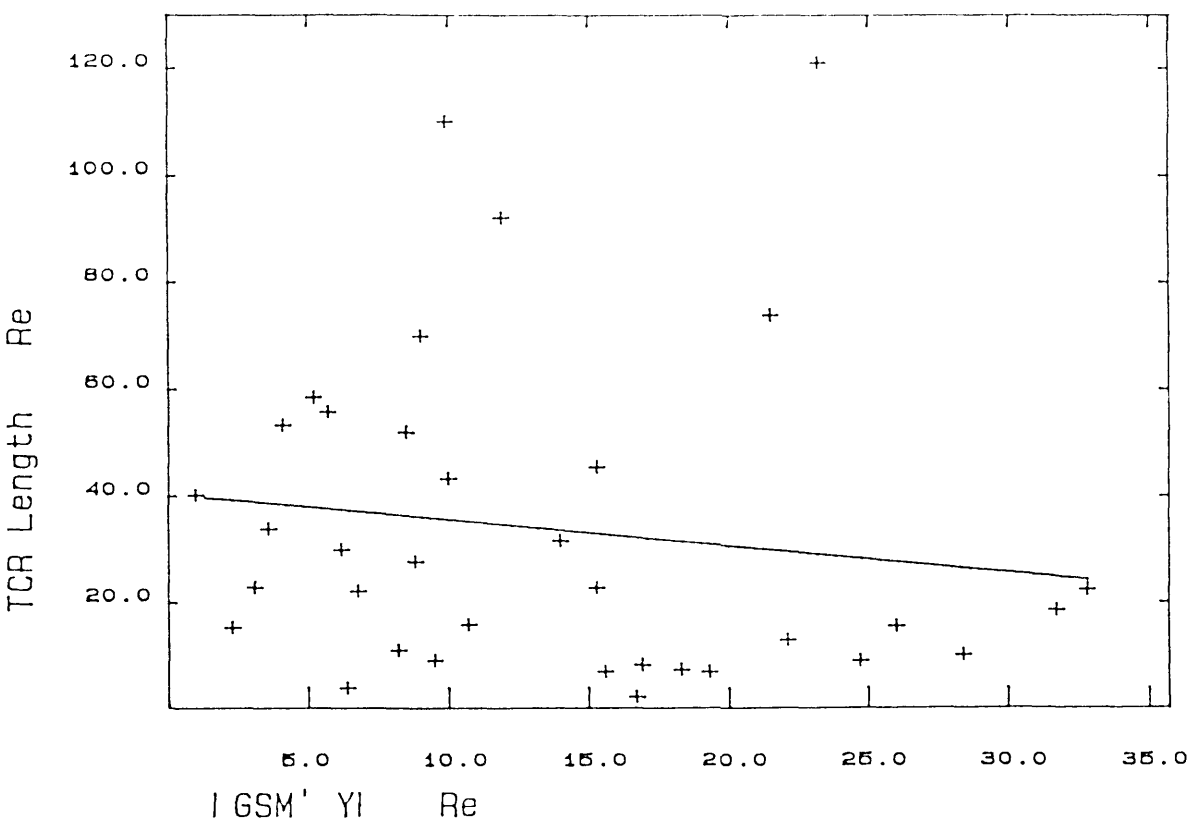


Figure 3.4d. TCR length, in R_E, plotted against |GSM' Y|, in R_E. Regression analysis, from 35 data points, gives r=-0.14; the fitted line is shown for reference.

there is no evidence to suggest that TCR length varies with GSM' X (r = -0.02).

Figures 3.4a), b), c), and d) show the same TCR properties plotted against the magnitude of GSM' Y(|GSM' Y|). Figures 3.4a) and c) show compression ratio and velocity Vx, respectively, plotted against |GSM' Y| neither of these plots show any significant trend. Figure 3.4b) shows TCR duration plotted against |GSM' Y|. Regression analysis gives r = -0.28, which for 54 points is significant at less than the 5% level, thus implying that there is a negative correlation between the magnitude of GSM' Y and TCR duration. Figure 3.4d) shows TCR length plotted against |GSM' Y|, and again regression analysis does not suggest a significant trend in the data (r = -0.14).

Figures 3.5a), b), c) and d) show TCR properties plotted against |GSM' Z|. Figure 3.5c) has TCR velocity Vx plotted against |GSM' Z|; regression analysis gives r = 0.31 which implies a correlation which is significant at less than the 10% level. The remaining three plots, 5 a), b) and d), show compression ratio, duration and length respectively, plotted against |GSM' Z|; in each case the regression coefficient is almost 0 and so we can conclude that there is no trend between these variables and |GSM' Z|

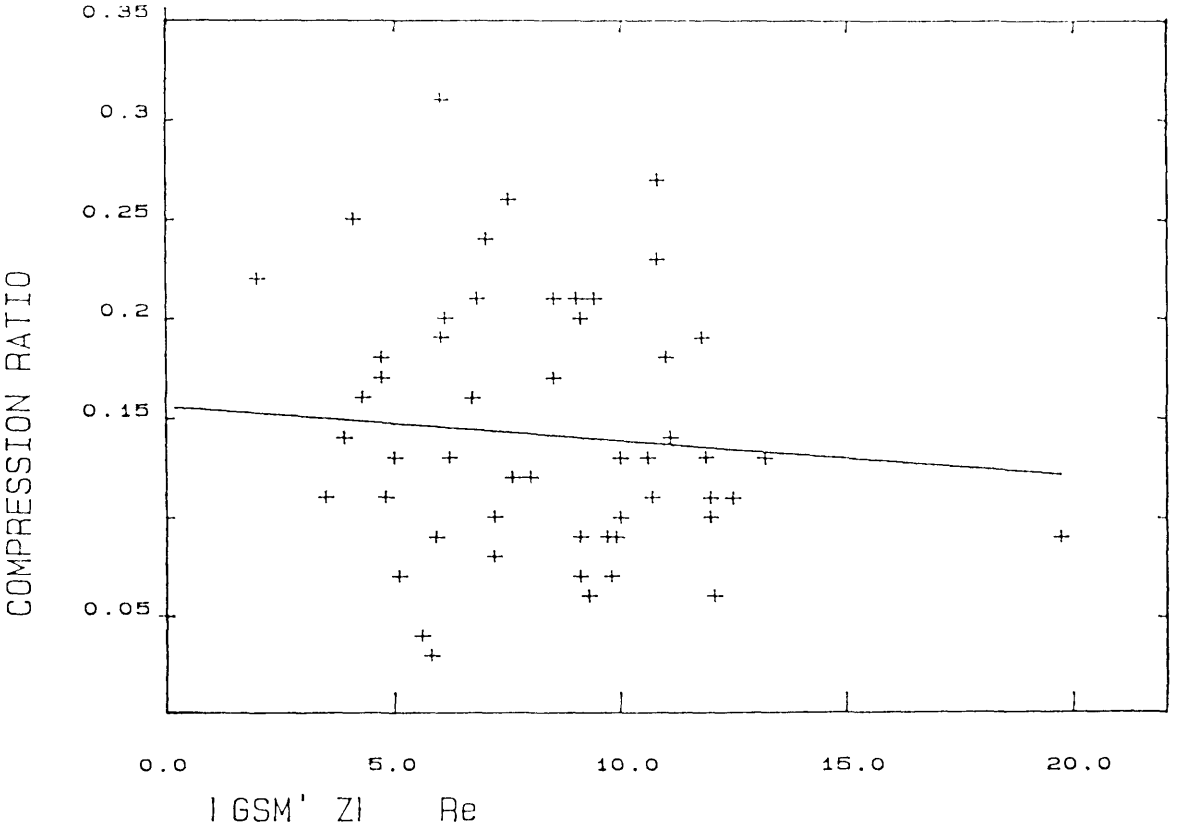


Figure 3.5a. TCR compression ratio, plotted against |GSM' Z|, in R_E. Regression analysis gives r=-0.09 from 54 points. The fitted line is shown.

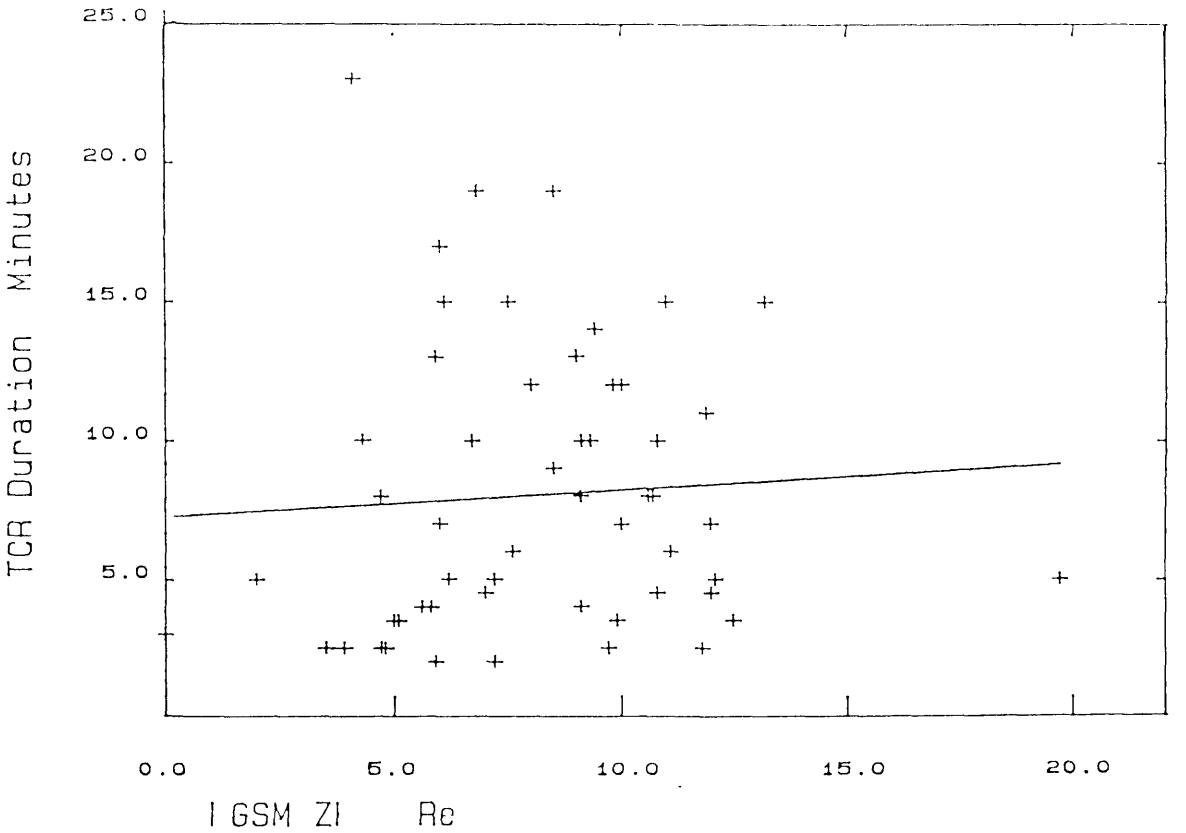


Figure 3.5b. TCR duration, in minutes, plotted against |GSM' Z|, in R_E. Regression analysis gives r=0.06 from 54 points. The fitted line is shown.

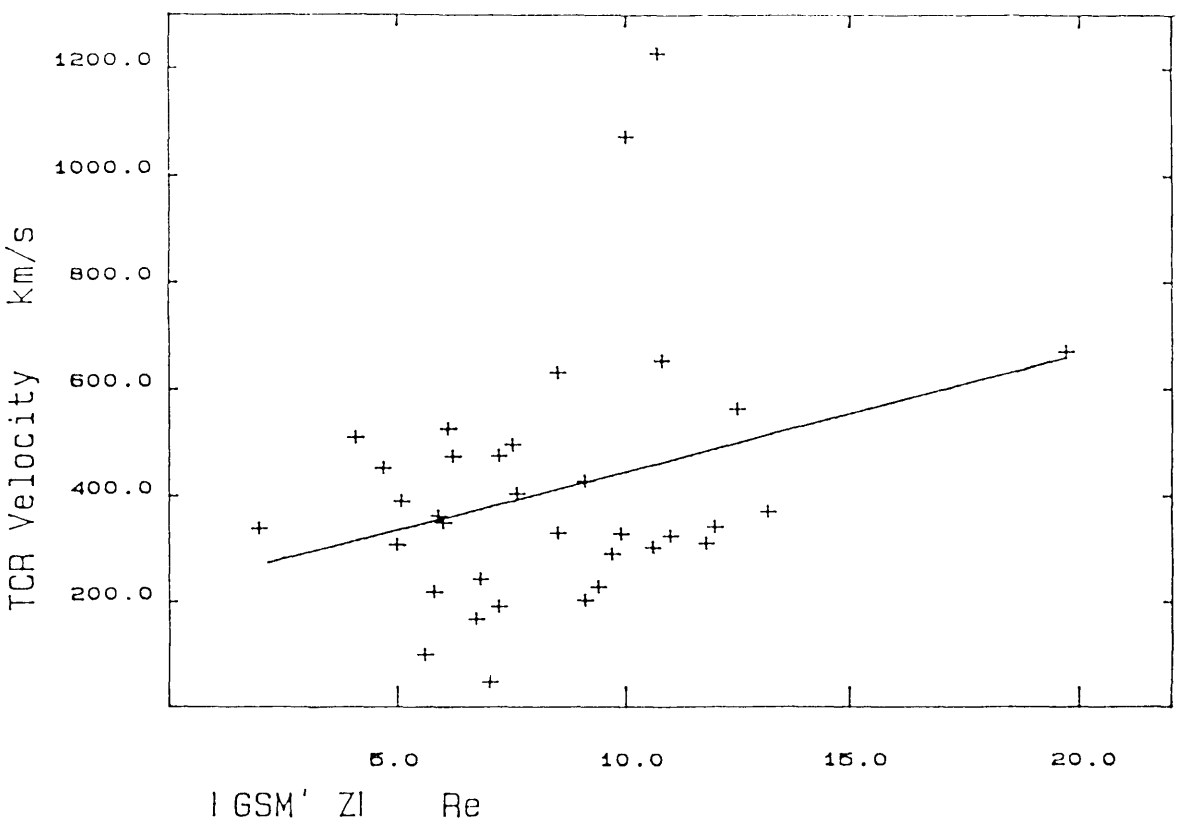


Figure 3.5c. TCR time of flight velocity, in kms^{-1}, plotted against |GSM' Z|, in R_E. Regression analysis gives r=0.31 from 35 data points. The regression line is shown.

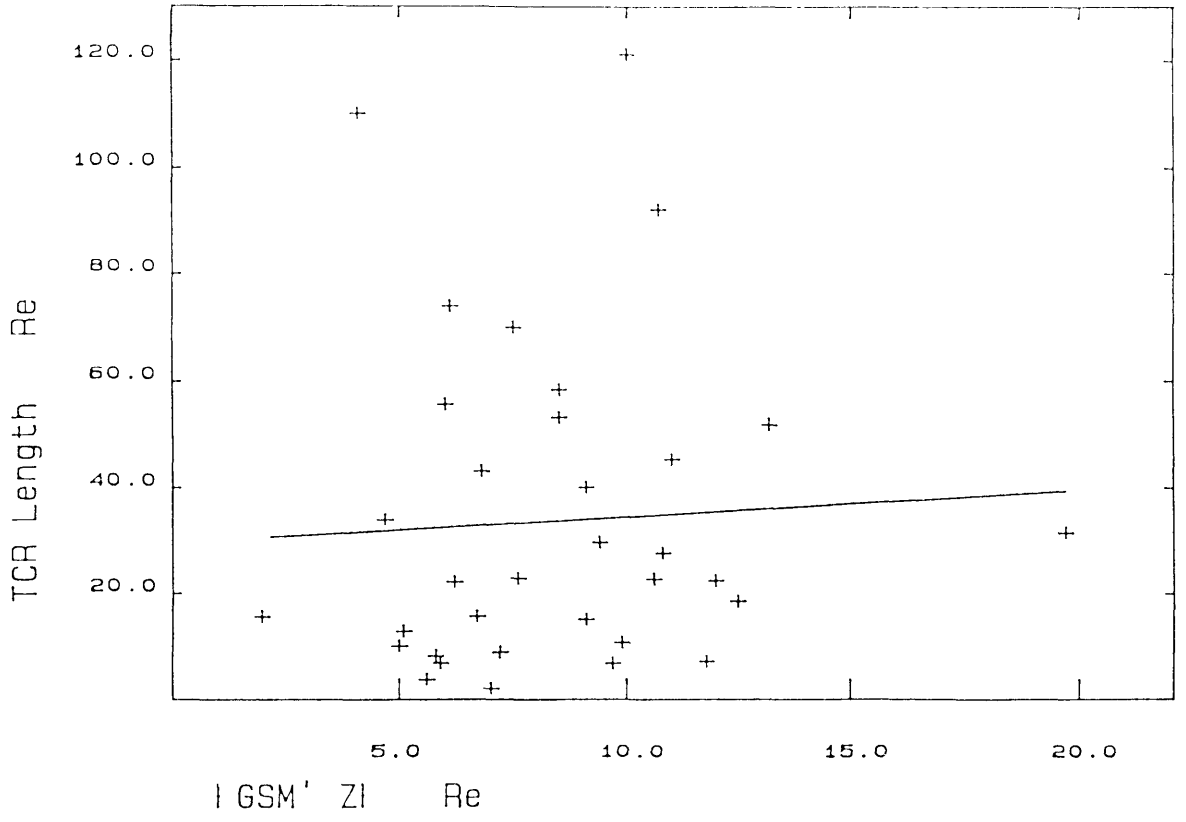


Figure 3.5d. TCR length, in R_E, plotted against |GSM' Z|, in R_E. Regression analysis, from 35 data points, gives r=0.06; the fitted line is shown for reference.

Before trying to interpret the variation in TCR properties with position it is instructive to examine the spatial coverage of ISEE-3 in the GSM' coordinate system. Figures 3.6a), b) and c) show the positions of the TCR observations contained in this data set, in the GSM' X-|Z| plane, the GSM' |Y|-|Z| plane and the GSM' X-|Y| plane respectively. Figures 3.6a) and b) show a reasonably uniform distribution of |GSM' Z| with GSM' X and GSM' |Z| with GSM' |Y|, however figure 3.6c) shows that we only have coverage of GSM' |Y| values greater than 20 R_E for GSM' X tailward of -175 R_E.

In considering the variation of TCR properties with position, we immediately encounter a problem, from Figure 3.3b) we deduced that there was a trend for TCRs with shorter durations to be seen further downtail, also from Figure 3.4b) we deduced that shorter duration TCRs to be seen for larger |GSM' Y| values. Figure 3.6c) shows us that large |GSM' Y| values occur only for large -GSM' X values, and so it is not possible to decide whether TCR duration varies with GSM' X or GSM' Y, or with both.

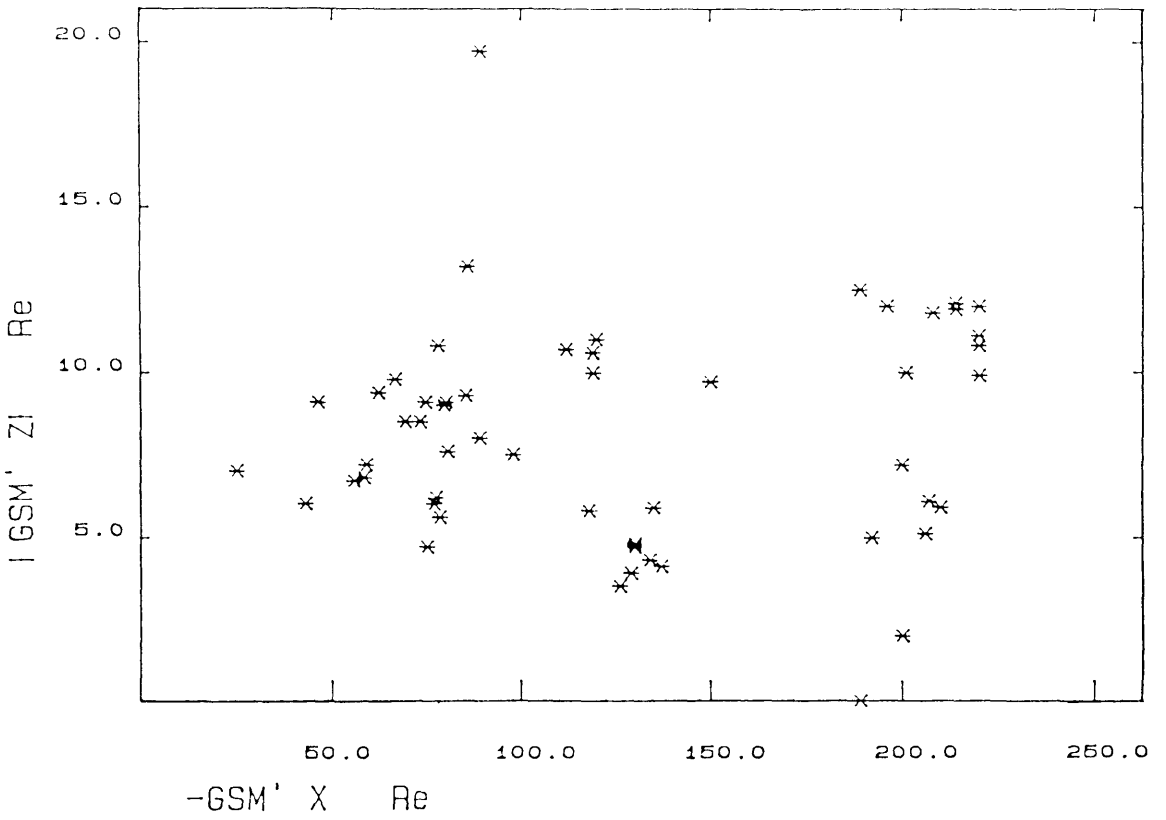


Figure 3.6a. The positions of the 54 TCR observations in the current data set, in the GSM' X-|Z| plane.

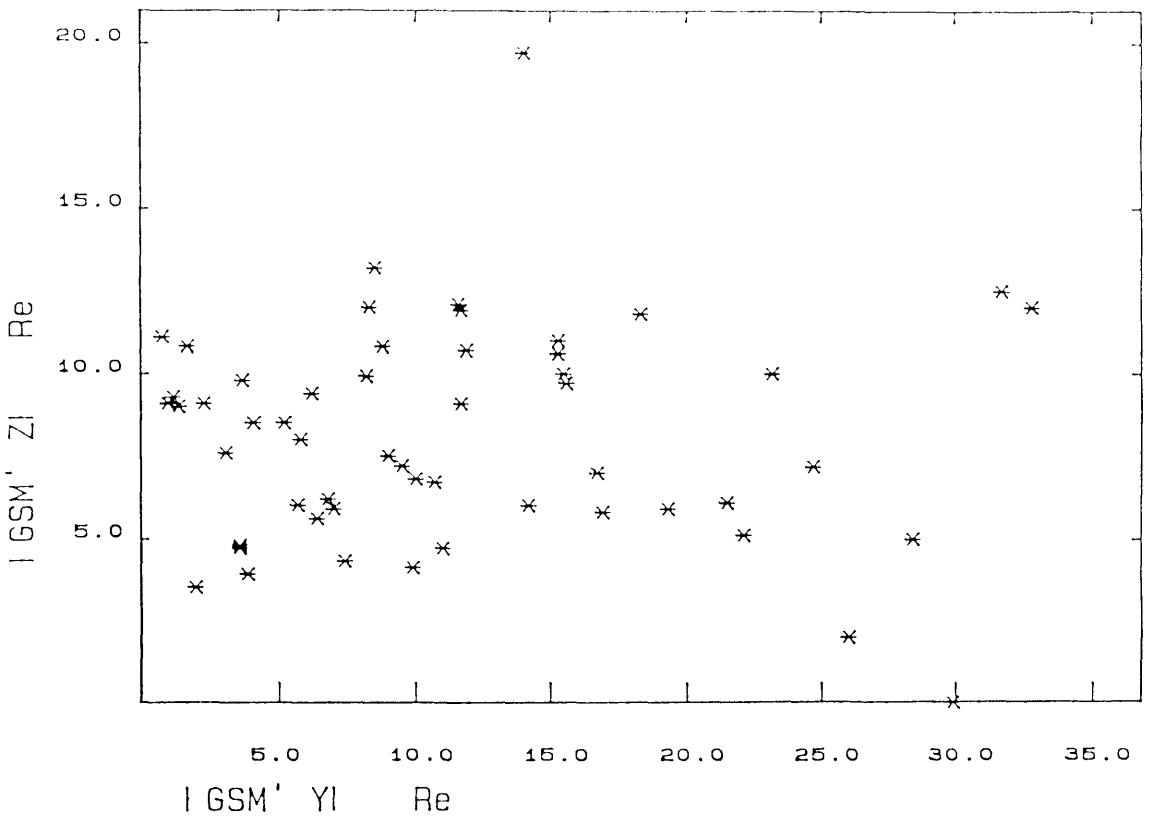


Figure 3.6b. The positions of TCR observations in the GSM' |Y|-|Z| plane.

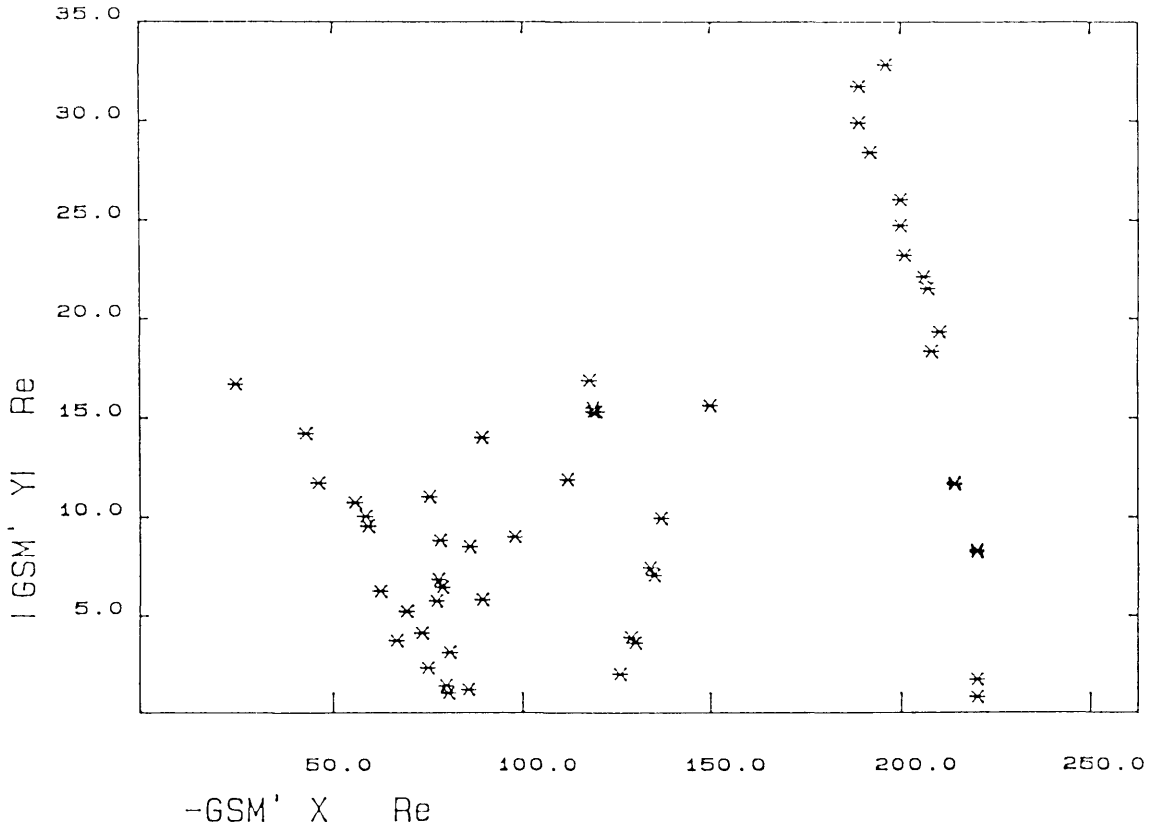


Figure 3.6c. The positions of TCR observations in the GSM′ X-|Y| plane.

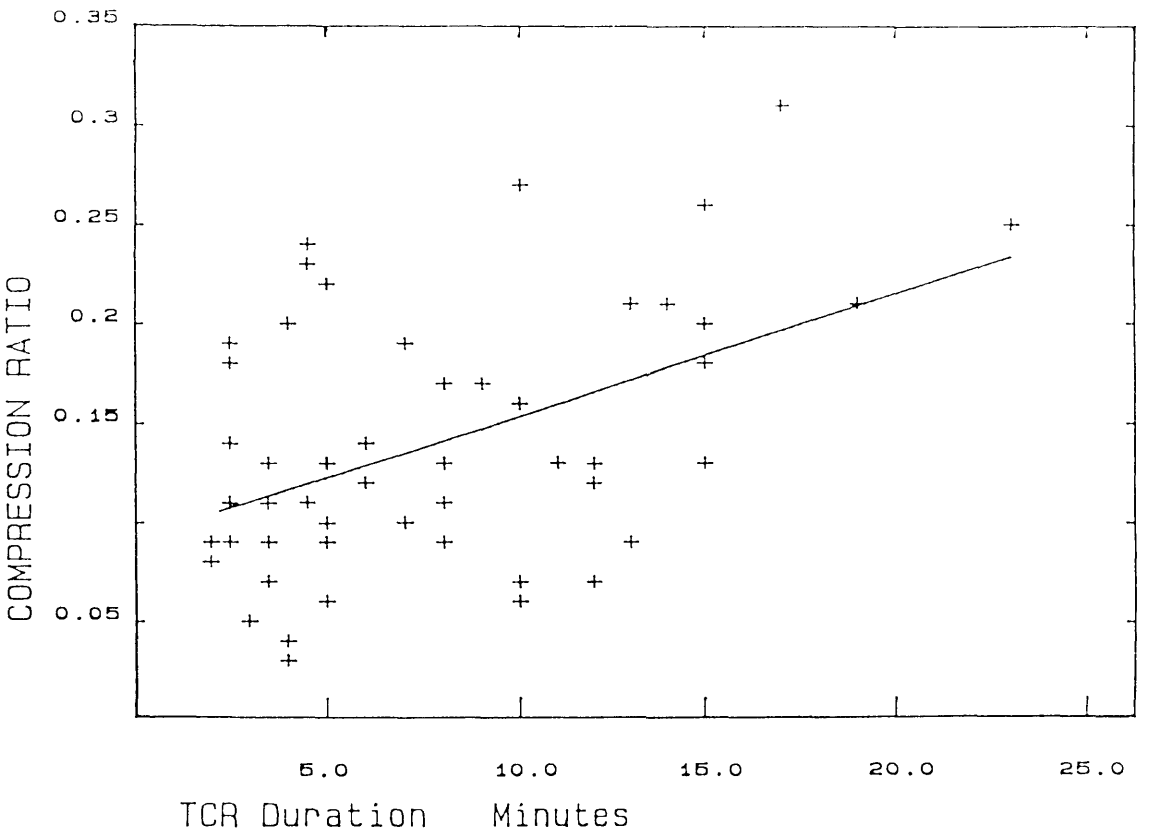


Figure 3.7a) Compression ratio plotted against TCR duration, in minutes. Linear regression analysis gives a correlation coefficient, r, of 0.49 for 54 points. The regression line is shown.

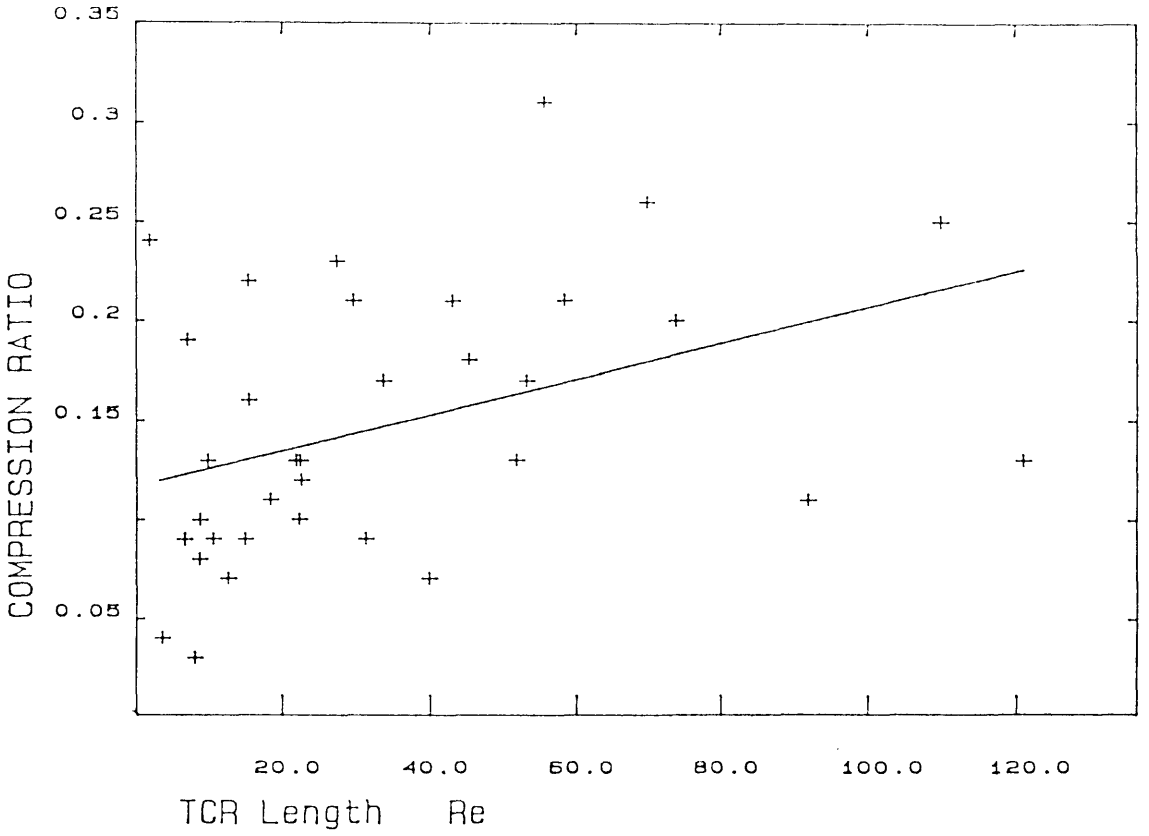


Figure 3.7b) Compression ratio plotted against TCR length, in R_E. From regression analysis we have r=0.4, for 35 points. The fitted line is shown.

Variations in TCR properties not dependent on position

Figure 3.7a) shows TCR duration plotted against compression ratio; regression analysis gives r = 0.49, which for 54 points is significant at less than the 0.1% level. This means that there is a trend for longer duration TCRs to have larger compression ratios. Figure 3.7b) is a plot of TCR length against compression ratio, and again we can see that there is a trend for longer TCRs with larger compression ratios (r = 0.4 for 35 points, this gives a significant correlation at less than the 2% level.). This is as we would expect, because the TCR length is directly proportional to the duration.

Effects of TCRs on energetic ion fluxes

In this section we will consider the effects that the passage of Travelling Compression Regions have on energetic ion fluxes in the magnetotail lobes. These effects fall into three categories, i) there is an enhancement in ion flux as the TCR passes ISEE-3, ii) the TCR produces no detectable effect in the ion flux and iii) there is a decrease in ion flux as the TCR passes.

Energetic ion enhancements associated with TCRs

In 26 of the 54 events in the data set an ion enhancement is seen associated with the passage of a TCR. For these events we will try to determine the possible causes of the ion enhancement, and whether observation of these enhancements is due to a temporal or spatial effect. Four examples of ion enhancements are presented, with varying degrees of complexity in both magnetic field and ion signatures. All four of these examples occurred whilst ISEE-3 was in the northern tail lobe, tailward of the expected position of a substorm neutral line.

Figure 3.8a) shows the omnidirectional ion flux in the lowest three energy channels (35-56,56-91 and 91-147 keV) compared with the magnetic field magnitude and direction, between 1730 and 1830 UT on 21 October 1982 (Day 294). At this time ISEE-3 was at -75 R_E GSM X. No substorm data is available for this event.

From the magnetic field data we can see that a double TCR is observed with peaks in compression occurring at 1759 and 1803 UT (There is a data gap prior to these events which ends at 1756 UT.), followed by a second double compression with peaks at 1814 and 1817 UT. Prior to the TCRs observed during this period the energetic ion flux in energy channel 1 is 0.3 cm^{-2} s^{-1} sr^{-1} keV^{-1}, which is

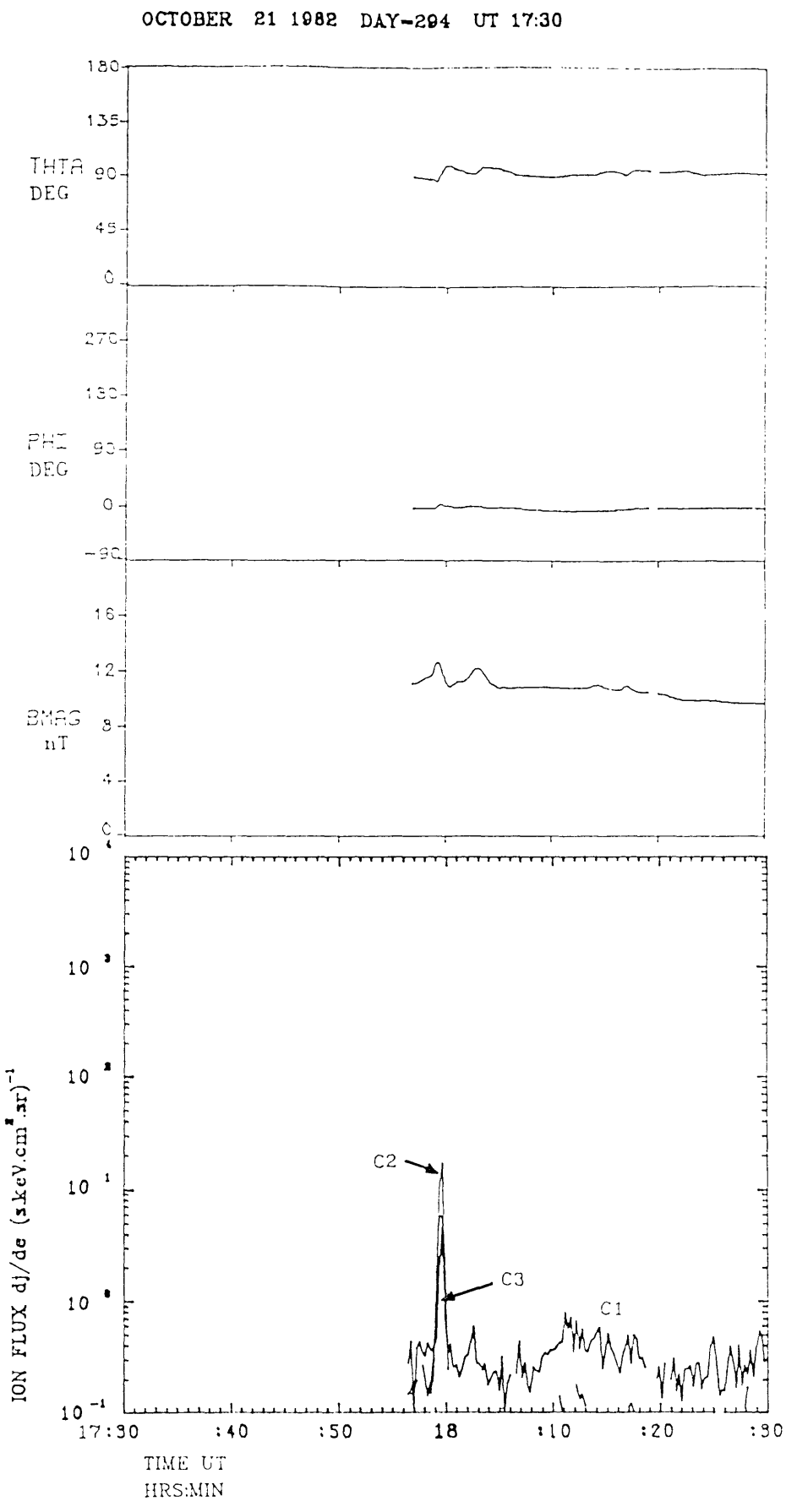


Figure 3.8a) Omnidirectional ion flux in the three lowest energy channels, (35-56, 56-91 and 91-147 keV) compared with the magnetic field magnitude, BMAG, polar angle THTA and azimuthal angle PHI, for the period between 1730 and 1830 UT on October 21st 1982. The energy channels are marked C1, C2 and C3 respectively. A data gap occurs prior to 1756 UT.

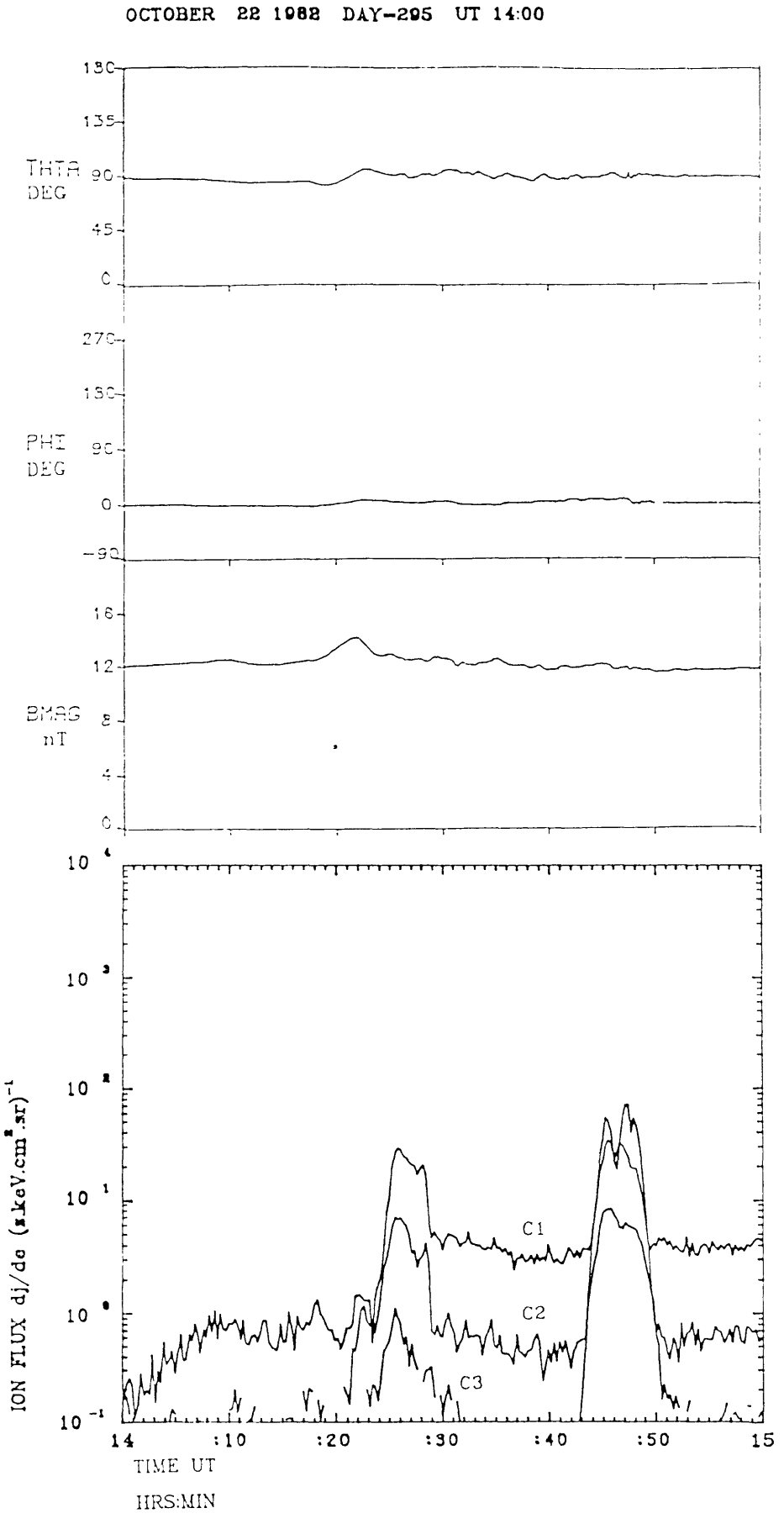


Figure 3.8b) The omnidirectional ion flux in the three lowest energy channels, compared with the magnetic field magnitude, BMAG, polar and azimuthal angles THTA and PHI (as figure 3.8a), for one hour, between 1400 and 1500 UT on October 22nd 1982.

consistent with ISEE-3 being in the magnetotail lobe (Cowley et al., 1984). Coincident with the first TCR at 1759 UT there is a short burst of energetic ions, lasting from 1748:30 to 1800 UT. Velocity dispersion is seen on the leading edge of the enhancement (ie. the most energetic particles are observed first), and reverse velocity dispersion is seen on the trailing edge. This is consistent with dispersions seen in previous observations of the plasma sheet boundary layer (Richardson and Cowley, 1985). This ion enhancement is unusual in that there is an apparent inversion in the ion spectrum, with both channels 2 and 3 detecting a higher flux than channel 1. Following this enhancement the energetic ion flux returns approximately to its previous level. There is no significant change in ion flux coincident with the second compression at 1803 UT, nor do the third and fourth compressions (1814 and 1817 UT) show any obvious effects in the energetic ion data.

Figure 3.8b) shows the omnidirectional ion flux for the lowest three energy channels, compared with the magnetic field magnitude and direction, between 1400 and 1500 UT on 22 October 1982 (Day 295). During this interval ISEE-3 was at approximately -80.5 R_E GSM Xm, and as in the previous event it was not possible to determine a substorm onset time.

A single TCR can be seen in the magnetic field plot lasting from 1418 to 1424 UT, with a maximum in amplitude at 1422 UT. Following this TCR the magnetic field becomes disturbed until approximately 1450 UT. If we now examine the energetic ion data in figure 3.8b) we see that the flux is more variable than the previous example. There is no clear effect seen in channel 1 until after the passage of the TCR, however channel 2 shows a small ion enhancement which coincides with the TCR at 1422 UT. At 1423:30 UT an enhancement in ion flux occurs in energy channels 1,2 and 3. This enhancement subsides at 1429 UT, but the fluxes in channels 1 and 2 remain higher than their value prior to the arrival of the TCR (4 cm^{-2} s^{-1} sr^{-1} keV^{-1} and 0.6 cm^{-2} s^{-1} sr^{-1} keV^{-1} respectively). There is no measurable velocity dispersion seen on either the leading or trailing edge of the ion enhancement. A second, larger, ion enhancement occurs between 1443 and 1450 UT, although there is no obvious magnetic field signature relating to this event. Velocity dispersion can be seen on both the leading and trailing edges of the enhancement.

Figure 3.8c) again shows a comparison between energetic ion data and magnetic field magnitude and direction. The plot shows two hours of data between 0230 and 0430 UT on April 14 1983 (this is the same period as shown in figure 3.1). At the time these observations were made ISEE-3

was at -77.4 R_E GSE X. A substorm onset at 0257:30 UT was reported by Slavin et al., and identified by an enhancement in AKR and a particle injection seen by spacecraft 1982-019 in geostationary orbit.

The magnetic field data is dominated by a large TCR which is observed between 0307 and 0324 UT (the exact time at which the TCR ends is difficult to judge due to the data gap which occurs between 0325 and 0331 UT). Several small ripples can be seen in the magnetic field magnitude after this first TCR, but they do not show a clear north-south bipolarity in the polar angle. If we assume that the TCR was released at -20 R_E GSE X and at the same time as the substorm onset, then a simple time of flight calculation gives a tailward velocity for the TCR of 349 kms^{-1} and a length of 56 R_E.

An energetic ion burst occurs between 0313 and 0320 UT, coincident with the peak compression of the TCR, which shows velocity dispersion on the leading edge and reverse velocity dispersion on the trailing edge. The energetic ion flux is, on average, the same before and after the TCR (3 cm^{-2} s^{-1} sr^{-1} keV^{-1} in energy channel 1), but after the compression the ion flux appears to be more variable. After the initial TCR there is no obvious correlation between the magnetic field data and the energetic ion flux.

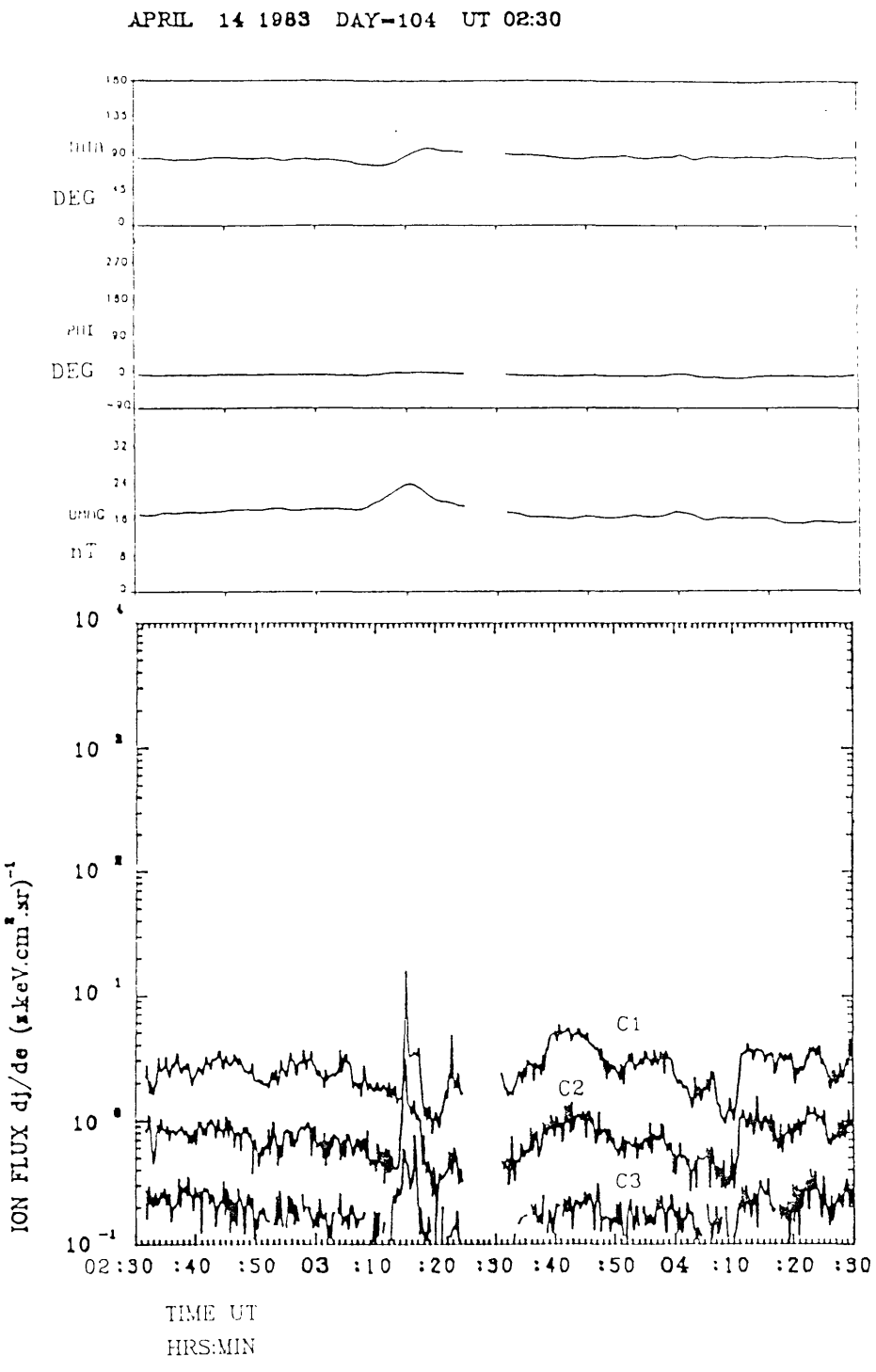


Figure 3.8c) As for figures 3.8a and b, for two hours, between 0230 and 0430 UT on April 14th 1983.

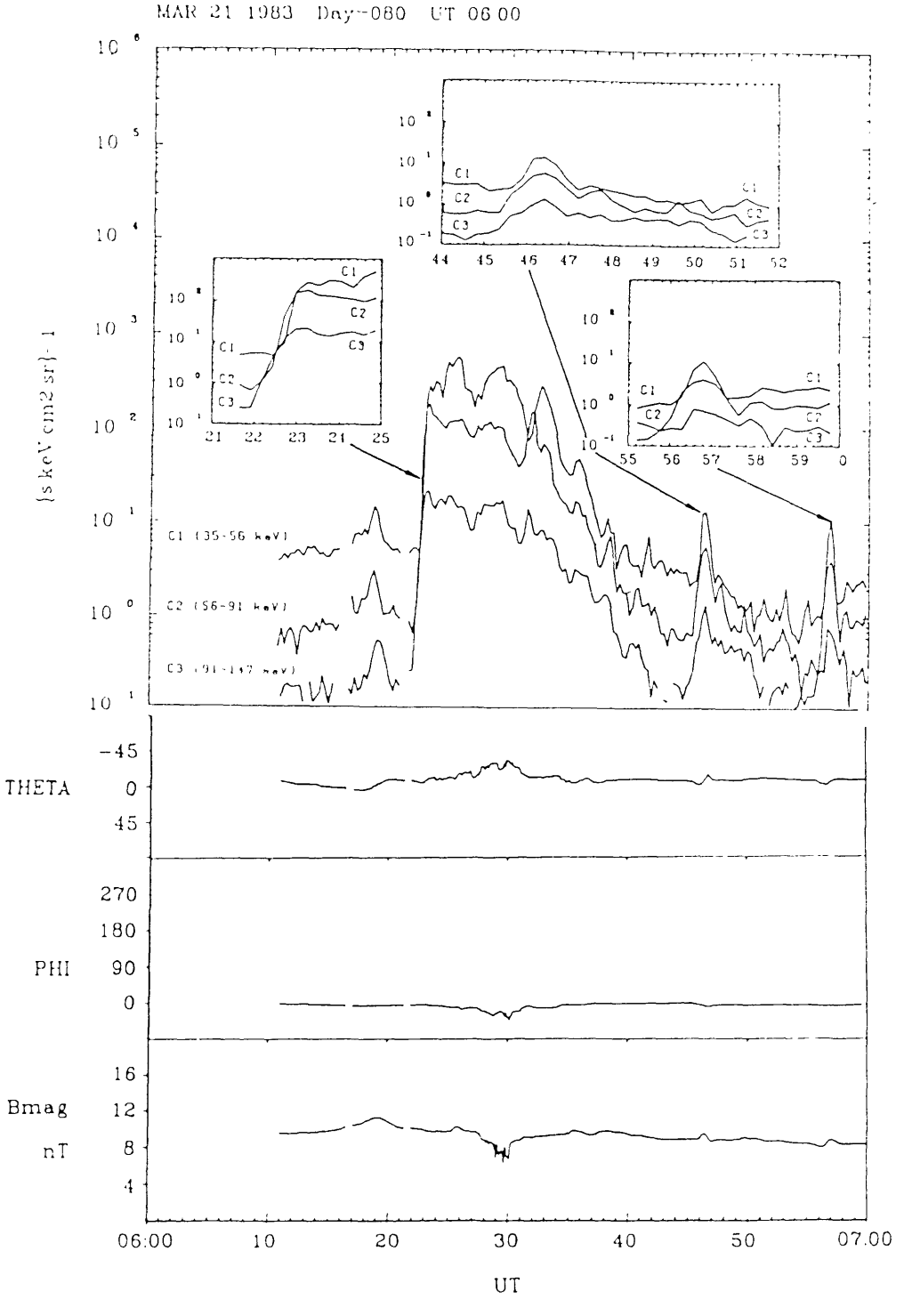


Figure 3.8d) Omnidirectional ion flux, in the lowest three energy channels, compared with the magnetic field magnitude and direction, for one hour between 0600 and 0700 UT on March 21st 1983. The three insets, in the upper panel, show velocity dispersion associated with rapid changes in ion flux.

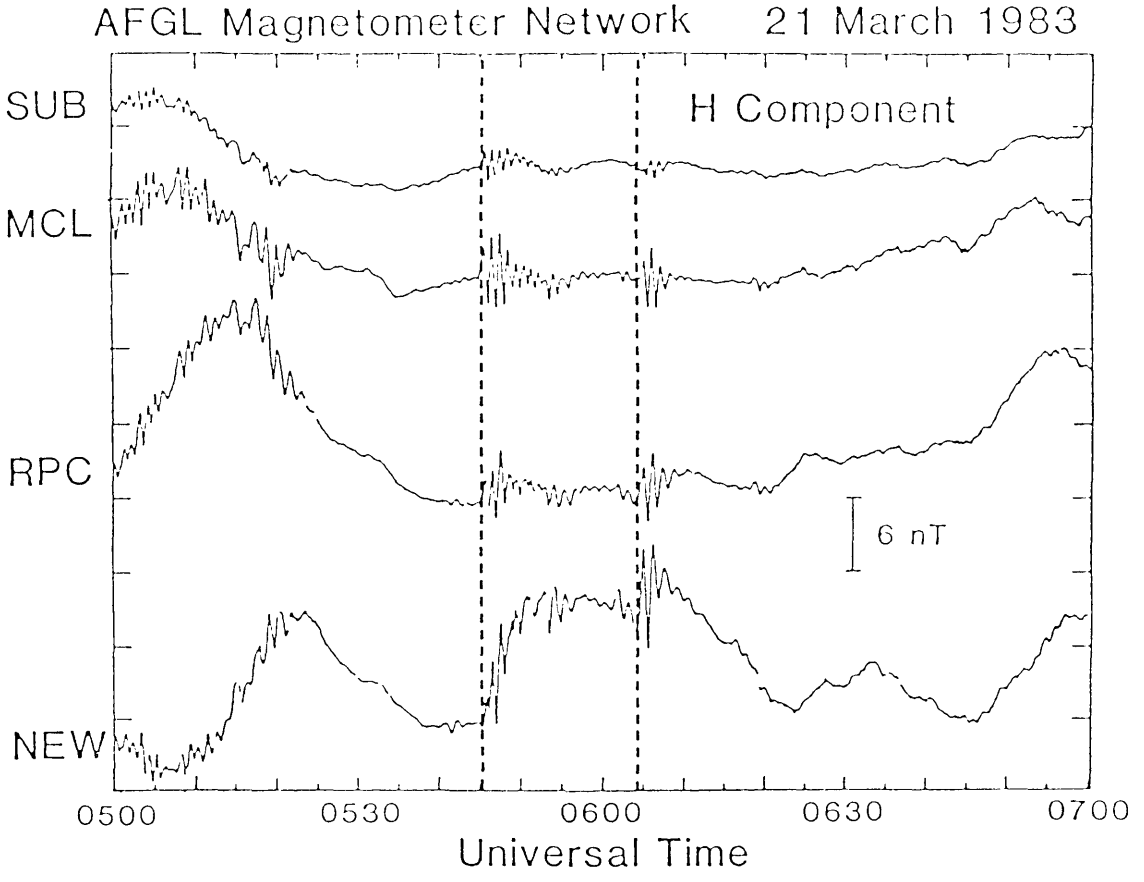


Figure 3.8e) Magnetogram, from the AFGL magnetometer network, for the period 0500 to 0700 UT on March 21st, 1983. The times of two substorm onsets are indicated by Pi 2 bursts and marked by vertical lines.

Figure 3.8d) shows a more complicated event which was observed between 0600 and 0700 UT on 21 march 1983. Again magnetic field strength and direction are compared with the omnidirectional ion flux in the lowest three energy channels.

The early hours of 21 March 1983 were geomagnetically active, with several large substorms before 0600 UT. Figure 3.8e) shows data between 0500 and 0700 UT from four magnetometer stations, on the AFGL magnetometer network. The substorm believed to be responsible for the TCR seen by ISEE-3 from 0616 to 0621 UT occurred at 0545 UT, and was identified from Pi2 bursts marked by a vertical line on figure 3.8e). The substorm onset was verified from a dispersive particle injection, with higher energies detected first, seen by spacecraft 1982-019 in geostationary orbit. The spacecraft local time was 0125. Pi2 bursts also indicate a second substorm onset at 0604 UT and are again marked by a vertical line on figure 3.8e).

Initially the ion flux in channel 1 (35-56 keV) is low, at 4.6 cm^{-2} s^{-1} sr^{-1} keV^{-1}. A small ion enhancement is seen between 0618 and 0620 UT, which is coincident with a magnetic field compression lasting for 5 minutes, and showing the signature of a TCR. At 0622:30 UT there is a

large ion enhancement which lasts for 20 minutes. This enhancement shows a velocity dispersion on the leading edge, with ion flux in energy channel 2 (56-91 keV) increasing 32 seconds before channel 1, (see inset on figure 3.8d)). During this ion enhancement the magnetic field shows several interesting features. At 0630 UT there is a large decrease in magnetic field magnitude, which is probably caused by a brief incursion from the boundary layer region into the plasma sheet, caused by a bulk motion of the magnetotail. Small increases in magnetic field strength occur at 0625:30 UT, 0635:30 UT, and 0638 UT. While these compressions appear to coincide with modulations in the omnidirectional ion flux, they lack the clear north then south tilting of the magnetic field direction which characterizes TCRs. During the short duration entry of the spacecraft into the plasma sheet, at 0630 UT the magnetic field direction is tilted southward, which suggests that ISEE-3 is on magnetic field lines which are open to the interplanetary magnetic field. This type of plasma sheet entry could be caused by bulk motion of the tail due to changes in solar wind speed or direction. The particle enhancement decreases from 0630 UT over a period of 15 minutes, to a flux of 3 cm^{-2} s^{-1} sr^{-1} keV^{-1} in channel 1, until at 0646 UT there is a short ion burst, followed at 0657 UT by another short ion burst. Both bursts have a duration of 1.5 minutes in channel 1, and show a velocity dispersion

on the leading edges with reverse velocity dispersion on the trailing edges (see insets on figure 3.8d)). These ion enhancements coincide with small magnetic field compressions, showing typical TCR signatures.

The four events presented here show the types of energetic ion enhancements associated with TCRs. As has been seen, the ion enhancement need not coincide exactly with the TCR, nor does the presence of more than one TCR in an event guarantee that each individual compression will be accompanied by an ion enhancement. In order to gain some insight as to why this is so it is useful to examine the fluxes of 90^{O} pitch angle ions and ions with pitch angles close to 0^{O}, associated with the preceding events.

Figure 3.9a) shows the earthward and tailward streaming ion fluxes (ie ions with pitch angle close to 0^{O} or 180^{O}) together with fluxes of ions with 90^{O} pitch angles, for the 35-56 keV energy channel, between 1730 and 1830 UT on 21 October 1982. The magnetic field magnitude is shown for reference. From figure 3.8a) we saw that there was a single burst of ions, centred on the first compression in a double TCR, at approximately 1800 UT. If we now examine figure 3.9a) we can see that this ion enhancement only shows a significant effect in the ion fluxes streaming tailwards, and the ion fluxes detected in

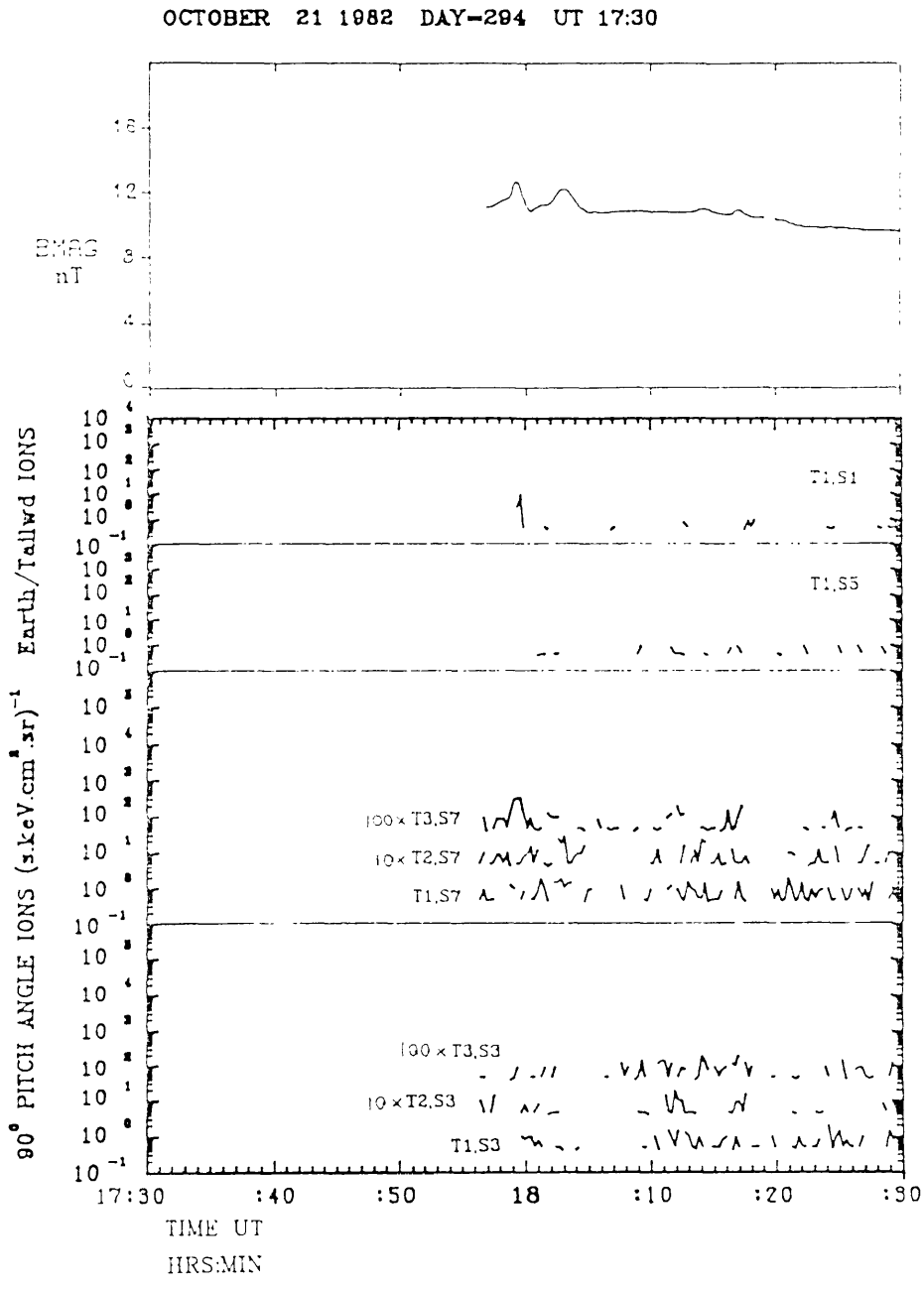


Figure 3.9a) Shows streaming ion and 90^{O} pitch angle ion data, for the 35-56 keV energy channel, between 1730 and 1830 UT on October 21 1982, compared with the magnetic field magnitude. The top panel shows the magnetic field magnitude, the next two panels show the energetic ion fluxes directed tailward and earthward respectively (T1,S1 and T1,S5), whilst the lower two panels show energetic ion fluxes from the 6 sectors detecting ions with pitch angle 90^{O} (T3,S7 T2,S7 T1S7 from below ISEE-3 and T3,S3 T2,S3 T1,S3 from above ISEE-3, in the northern tail lobe.). The terminology Tn,Sm refers to telescope n sector m where n ranges from 1 to 3 and m from 1 to 8. A data gap occurs prior to 1756 UT. The gaps seen in the ion data occur when no ions are detected in a particular telescope sector.

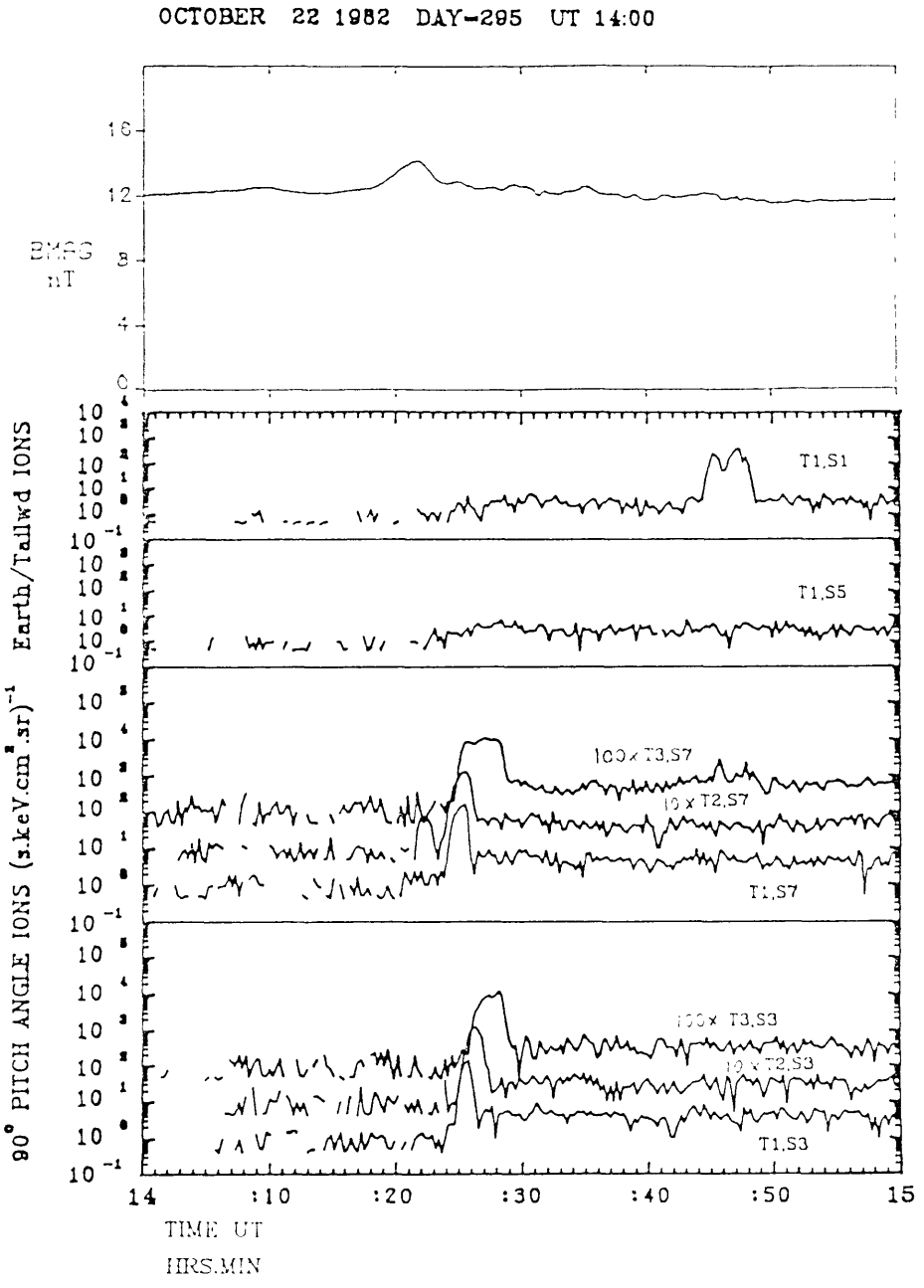


Figure 3.9b. As figure 3.9a, for the period between 1400 and 1500 UT on October 22nd 1982.

sector (3,7). The ion enhancement in sector (3,7) indicates that the ions detected are gyrating around a gyrocentre which is southward of the spacecraft (ie in the -GSE Z direction, relative to the spacecraft). This can be interpreted as a shallow entry in to the plasma sheet energetic ion boundary layer from the northern tail lobe. Fluxes of energetic ions with pitch angles close to 0^{O} can give some indication of the local field topology; in this case the tailward streaming ions suggest that ISEE-3 is tailward of an active reconnection site (neutral line) at the time of the observations.

Figure 3.9b) shows the 90^{O} pitch angle and streaming ion data, taken from the 35-56 keV energy channel, for the event observed between 1400 and 1500 UT on 22 October 1982, again the magnetic field magnitude is shown for reference. This event has a more complex ion signature than the previous event; from figure 3.8b) we saw that there were two ion enhancements, one associated with the TCR at 1422 UT and one which did not seem to be associated with any field disturbance at all. Examining figure 3.9b) it is clear that the two ion enhancements have markedly different effects in the streaming ion and 90^{O} pitch angle ion data. There is an increase in both earthward and tailward streaming ions which begins at 1422 UT (where the maximum magnetic field compression occurs). Following this increase, between approximately

1423 and 1430 UT, there is an enhancement in ion flux seen in all six sectors detecting ions with 90^{o} pitch angles. This enhancement suggests that ISEE-3 is detecting ions from gyrocentres from both above and below. Between 1422 and 1444 UT tailward and earthward ion fluxes are approximately equal and constant at 3.0 cm^{-2} s^{-1} sr^{-1} keV^{-1}. At 1444 UT there is a large enhancement in the flux of ions streaming tailwards (to approximately 200 cm^{-2} s^{-1} sr^{-1} keV^{-1}). This ion burst is coincident with the second increase in omnidirectional ion flux shown in figure 3.8b). The fluxes of ions with pitch angles of 90^{o} show no enhancement in any sector during this period. Returning to the enhancement in 90^{o} pitch angle ions, as was shown in chapter 2, it is possible, from the times of the onset and turn off of ion enhancements in each of the sectors in the GSE Y-Z plane, to determine a velocity for the energetic ion boundary layer during the increase and decrease of the ion enhancement. In this case the boundary layer moves upwards past ISEE-3 at 42 kms^{-1} and at an angle of 34^{o} to the GSE Z axis (angles are measured as positive rotating towards GSE Y). This motion is consistent with a movement of the plasma sheet boundary layer past ISEE-3 when in the northern tail lobe. The boundary layer recedes past ISEE-3 with a speed of 23 kms^{-1} at an angle of 80^{o} to the GSE Z axis. The direction of motion suggested by this boundary layer exit is not as might be

expected in the northern tail lobe, ie it is not downwards with respect to ISEE-3, so this implies that large amplitude waves are present on the surface of the plasma sheet during this period. Such perturbations of the plasma sheet surface have been implied in previous work by Daly et al. 1984.

Figure 3.9c) shows the streaming ion and 90^{O} pitch angle data in the 35-56 keV energy channel, together with the magnetic field magnitude, for two hours between 0230 and 0430 on April 14 1983 (day 104). From figure 3.8c) we saw that this event consisted of a single large TCR, with a peak at 0315 UT, which was associated with sharp enhancement in energetic ion flux. On examining figure 3.9c) we see that the TCR causes no change in streaming ion fluxes, either earthward or tailward. The fluxes of 90^{O} ions show an enhancement in sectors (1,7), (2,7) and (3,7), between approximately 0314 and 0319 UT, which again suggests an encounter with an energetic ion layer below ISEE-3 (in the -GSE Z direction), where we would expect the plasma sheet boundary layer to be located. Because ion enhancements are only seen in three of the sectors in the GSE Y-Z plane it is not possible to calculate a reliable velocity for the boundary layer.

After the data gap ending at 0331 UT both streaming ion fluxes and fluxes of ions with pitch angles of 90^{O} show

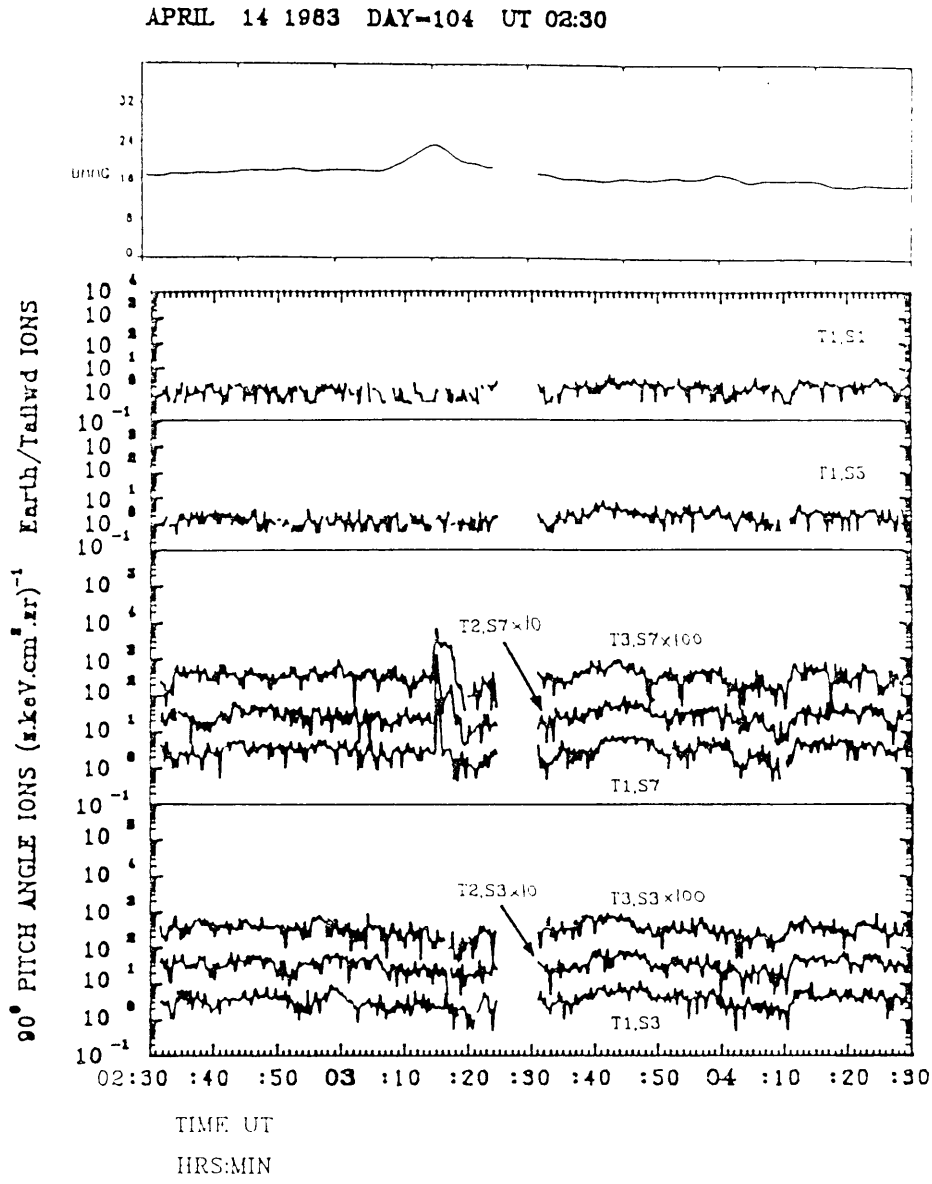


Figure 3.9c. As figure 3.9a, for a two hour period, between 0230 and 0430 UT on April 14th 1983.

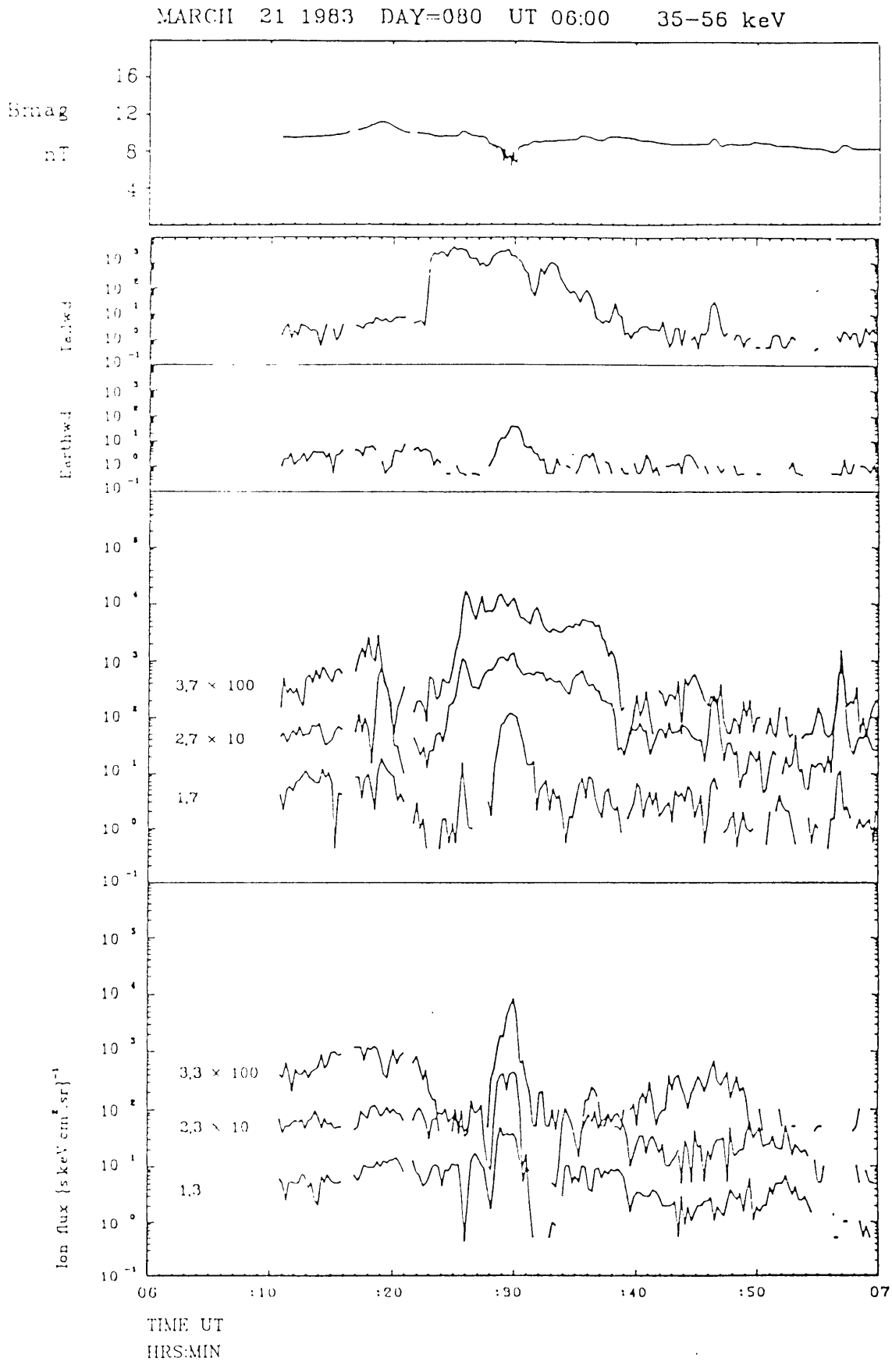


Figure 3.9d. As for figure 3.9a for the period between 0600 and 0700 UT on March 21st 1983.

greater variability, which may be due to a close proximity to the plasma sheet boundary layer.

Figure 3.9d) shows one hour of streaming ion and 90^{o} pitch angle ion data, in the 35-56 keV energy channel, between 0600 and 0700 UT on March 21 1983 (day 80), with the magnetic field magnitude for reference. Considering first the three ion enhancements associated with field compressions, we see that during the 0619 UT compression there is no significant increase in the ion flux streaming tailward, but there is a marked increase in ion fluxes from sectors (2,7) and (3,7), ie from below ISEE-3, (ion fluxes increase from 10 to 100 cm^{-2} s^{-1} sr^{-1} keV^{-1} in the 35-56 keV energy channel). This can be interpreted as a shallow entry into the plasma sheet boundary layer, which is below the spacecraft. The two magnetic field compressions at 0646 and 0657 UT show similar signatures in the magnetic field data, but have very different effects on the energetic ion fluxes. Whilst both these compressions produce a similar increase in omnidirectional flux (figure 3.8d)), they have markedly different effects on the ions with pitch angles of 90^{o} and the ions streaming along the magnetic field. Both compressions have an effect on the particles detected in the GSE Y-Z plane, ie at 90^{0} to the magnetic field; The first affects mainly sector (2,7), the second quite clearly affects sectors (1,7), (2,7) and (3,7).

This suggests that the second compression produces the deepest penetration into the boundary layer. When we look at the fluxes of ions streaming along the magnetic field, we see that the 0646 UT magnetic field compression is coincident with an increase in tailward streaming in the 35-56 keV energy channel, but the 0657 UT magnetic field compression is similar to the magnetic field compression between 0616 and 0621 UT, in that it has no effect at all on the streaming ions. These differences suggest that there has been a temporal change in the boundary layer during the observation of the compressions.

We now consider the large non TCR associated ion enhancement, which starts at 0622 UT in the omnidirectional flux. From the ion fluxes seen in the sectors in the GSE Y-Z plane (ie with pitch angles of 90^{O}), as shown in figure 3.9d), it is possible to calculate the velocity of the ion layer as it passes ISEE-3, as was shown in chapter 2. As the energetic ion fluxes are so high in this event it is possible to repeat this calculation for the 56-91 and 91-147 keV energy channels (data not shown), which allows us to sense gyrocentre positions at three different radii for each telescope viewing direction, ie 18 gyrocentres in all, and to observe a network of positions around the spacecraft past which the motion of the energetic ion

boundary layer can be sensed. Using the above calculations it is possible to calculate an average velocity for the boundary layer during expansion and contraction. During the expansion the average velocity is 21 $\pm$ 7 km s^{-1} at $2^0 \pm 8^0$ to the Z-axis (angles are positive rotating towards the +ve GSE-Y, ie. dawnwards), during contraction the velocity is 13 $\pm$ 3.5 km s^{-1} at $175^0 \pm 14^0$ in the same sense as above. As can be seen the direction of these velocities is as would be expected for movement of the plasma sheet boundary layer from beneath the spacecraft, whilst in the northern tail lobe. It is not possible to calculate velocities for the 0646 and 0657 UT ion enhancements, nor the ion enhancement between 0616 and 0621 UT, because they are seen in only a few of the sectors in the GSE Y-Z plane and so do not provide enough timings for a good velocity fit.

Conclusions

Three possible explanations for the ion enhancements associated with TCRs are; (1) A burst of energetic ions is produced earthward of the spacecraft and injected onto a bundle of field lines surrounding the spacecraft. (2) The plasma sheet boundary layer thickens, due to an increase in the rate of magnetic field line reconnection, and this causes the boundary layer to engulf the

spacecraft. The rate of magnetic field line reconnection then decreases, thinning the boundary layer, and again leaving the spacecraft wholly in the tail lobe. (Scholer et al., 1984). (3) Bulk movement of the plasma sheet relative to the spacecraft, caused for example by the tailward motion of a plasmoid, moves the energetic ion boundary layer past the spacecraft. Explanation (1) is not consistent with the observations for a number of reasons. Firstly, positive velocity dispersion, (The highest energy particles arrive first) would be expected on both leading and trailing edges of the ion enhancements, but, whilst positive velocity dispersion is seen on the leading edge of the ion enhancements, reverse velocity dispersion (The highest energy ion fluxes decrease last) is seen on the trailing edges. Secondly, due to the finite opening angle (32^0) of each particle telescope, and the 45^0 azimuthal sweep over which data are collected by EPAS, a range of pitch angles is integrated over in each telescope viewing direction. This produces a range of propagation delay times for ions seen in any one telescope, thus smearing out the effect of any rapid temporal change in ion production at a distant source. An impulsive increase in ion intensity at 20 R_E from earth would, if detected by a telescope in the GSE Y-Z plane, have a rise time of over 30 minutes at 133 R_E from earth (the GSE -X position of the March 21 event). Thus this would suggest that short bursts of ions, as

seen at 0646 UT and 0657 UT on March 21 1983, and rapid ion onsets, as seen at 0622 UT on the same day, are either spatial in nature or are produced in very close proximity to the spacecraft. Ion enhancements produced by thickening of the plasma sheet boundary layer, possibility 2, would again be subject to the above dispersion of pitch angles. This is not consistent with the 90^{o} pitch angle data presented for any of the four events discussed above. Thus, whilst it is probably a feature of the substorm process, boundary layer thickening is not thought to play a dominant role in the TCR ion enhancements. We are left with the third explanation, that is, bulk motion of the boundary layer, as the cause of the ion enhancements seen. As has already been shown the 90^{o} pitch angle data fully supports this idea, and so we conclude that the TCR ion bursts are caused by motion of an energetic ion boundary layer past the spacecraft.

The fluxes of ions with pitch angles of 90^{o} and ions with pitch angles close to 0^{o} provide important information about the nature and cause of ion enhancements associated with TCRs. In each event presented the enhancement in omnidirectional ion flux was accompanied by an increase in fluxes of ions with a 90^{o} pitch angle. The directions from which these ions were detected suggest that they originate in the plasma sheet boundary layer, which in

the cases described was below the spacecraft. Fluxes of ions streaming along the magnetic field were not always seen during omnidirectional ion enhancements, and in events in which they were observed their intensity relative to ions with 90^{O} pitch angle was not always constant throughout an event (cf the two ion enhancements on October 22, and the ion enhancements at 0646 and 0657 UT on March 21). This may suggest that the pitch angle distribution in the plasma sheet boundary layer can show a large temporal variation.

Figure 3.10) shows a possible scenario for the production of the energetic ion and magnetic field signatures seen between 0600 and 0700 UT on March 21 1983. This figure shows two plasmoids, one single loop and one double loop structure, corresponding to the TCRs seen between 0619 and 0621 UT and the two TCRs seen at 0646 and 0657 UT. A possible trajectory for ISEE-3 is shown and the times of the TCRs and the incursion into the plasma sheet are marked. If we assume that the first plasmoid is released by the substorm at 0545 UT, then from a time of flight calculation its speed would be 355 kms^{-1} (assuming it was released at 20 R_E from earth). From the TCR duration of 5 minutes, we can calculate a minimum plasmoid length of 16 R_E. If we then assume that the second, double, plasmoid was released by the substorm at 0604 UT, its

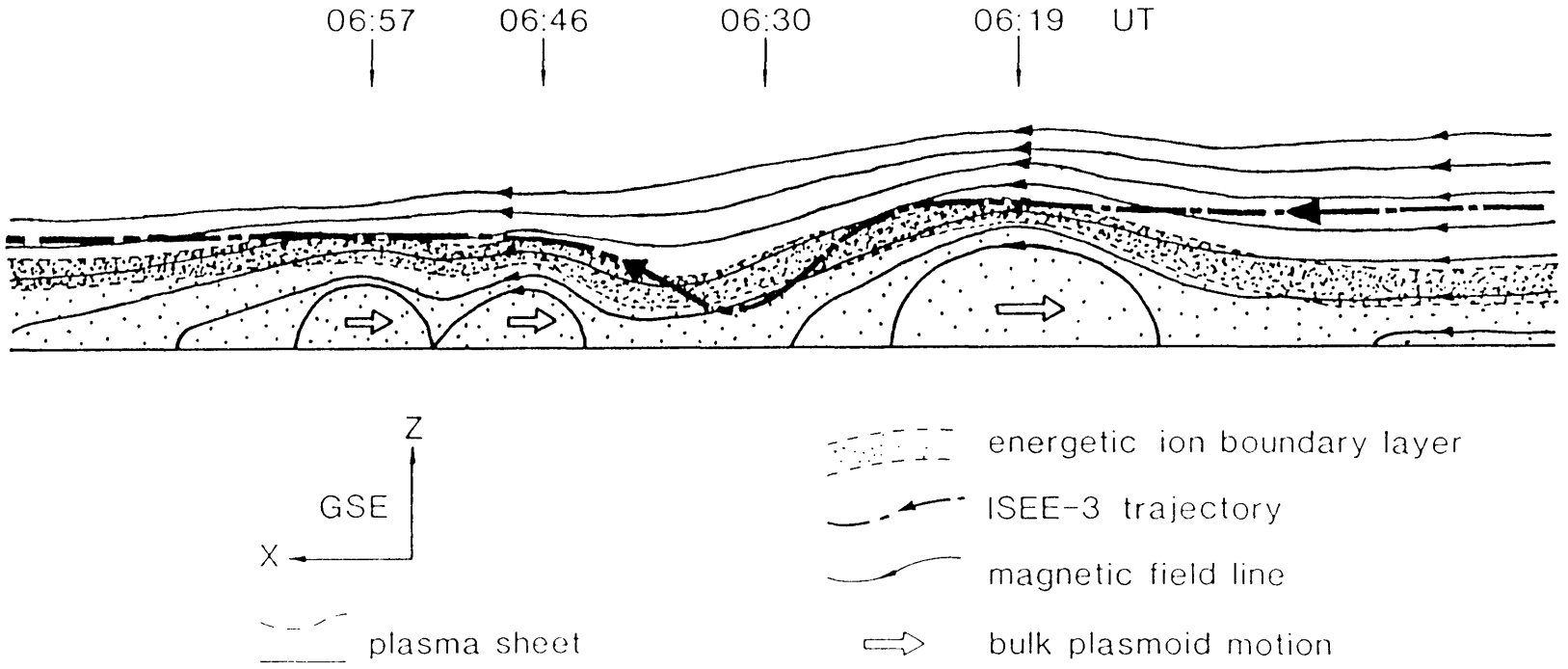


Figure 3.10. A schematic diagram of a section of the distant magnetotail, showing one possible scenario for the production of the magnetic field and energetic ion signatures observed between 0600 and 0700 UT on March 21st 1983.

velocity would be 254 kms^{-1} and the minimum size of each loop would be 3.6 R_E (for a TCR duration of 1.5 min).

Energetic ion decreases associated with TCRs

From the data set of 54 TCR events 2 were found which showed a significant decrease in ion flux associated with the observation of a TCR. Both events were observed on December 26 1982 (Day 360), the first between 0607 and 0626 UT and the second between 1325 and 1334 UT.
A complicating factor in the analysis of these events was that they occurred during a solar particle event (they were not the only observations of TCRs during solar particle events, and so the decrease in energetic ion flux in the two events is not caused by the presence of the solar particle event). A solar particle event has three main effects on energetic ions in the magnetotail; firstly the fluxes of energetic ions are higher than normal (a factor of 100 in some cases), secondly the pitch angle distribution of the ions is isotropic in the magnetotail frame, and thirdly the energy spectrum of the ions is much harder than normal.

Figure 3.11a) shows omnidirectional ion fluxes for the three lowest energy channels of the EPAS instrument, (35-56, 56-91, 91-147 and 147-238 keV) together with the magnetic field magnitude and direction, between 0530 and

0630 UT on Dec 26 1982. At this time ISEE-3 was at -69 R_E GSE X. The magnetic field data shows a TCR between 0607 and 0626 UT, with a peak in field compression at 0611 UT and a compression ratio of 0.21. The energetic ion data shows a slight decrease in flux in the two lowest energy channels between 0559 and 0607 UT (from 10 to 7 cm^{-2} s^{-1} sr^{-1} keV^{-1} in channel 1). This decrease in energetic ion flux is followed by a second decrease seen in all three energy channels between 0611 and 0622 UT (from 10 to 4.5 cm^{-2} s^{-1} sr^{-1} keV^{-1} in channel 1). If we compare the effect seen in each energy channel we see that the decrease in ion flux is progressively less in higher energy channels. The first decrease in ion flux seems to have no obvious cause in the magnetic field data, however the second decrease begins when the magnetic field strength peaks during the TCR.

Figure 3.11b) shows the magnetic field strength and direction compared with the omnidirectional ion flux in the lowest three energy channels of the EPAS instrument, for a period of one hour between 1300 and 1400 UT on Dec 26 1982. From the magnetic field data we can see that there are two TCRs, one occurring between 1325 and 1334 UT with a peak compression at 1328 UT, the other between 1344:30 and 1349:30 UT with a peak compression at 1347 UT. The compression ratios of these two TCRs were 0.15 and 0.04 respectively. The energetic ion data for this

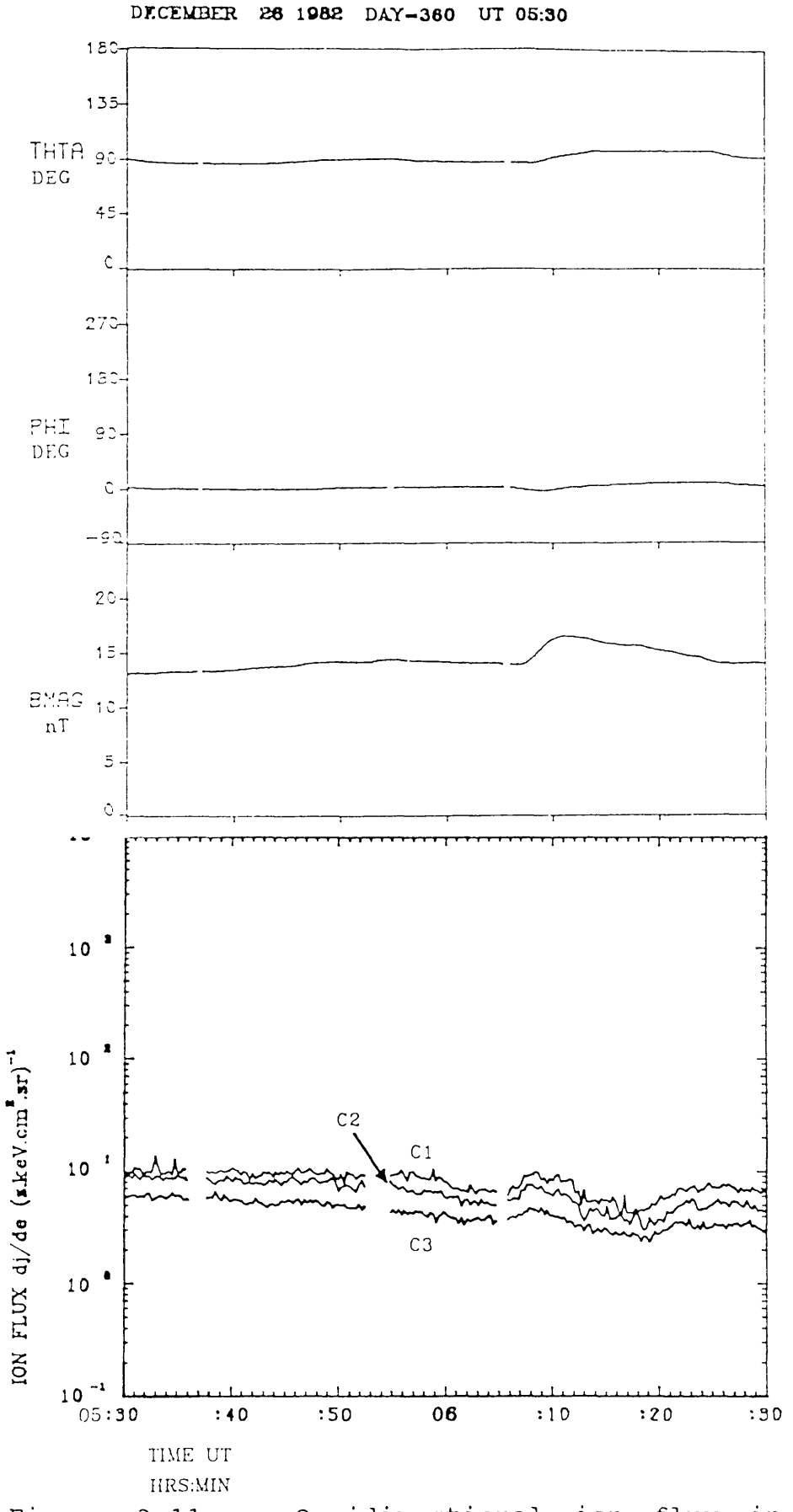


Figure 3.11a. Omnidirectional ion flux in the three lowest energy channels, (35-56, 56-91 and 91-147 keV) compared with the magnetic field magnitude, BMAG, polar angle THTA and azimuthal angle PHI, for the period between 0530 and 0630 UT on December 26th 1982. The energy channels are marked C1, C2 and C3 respectively.

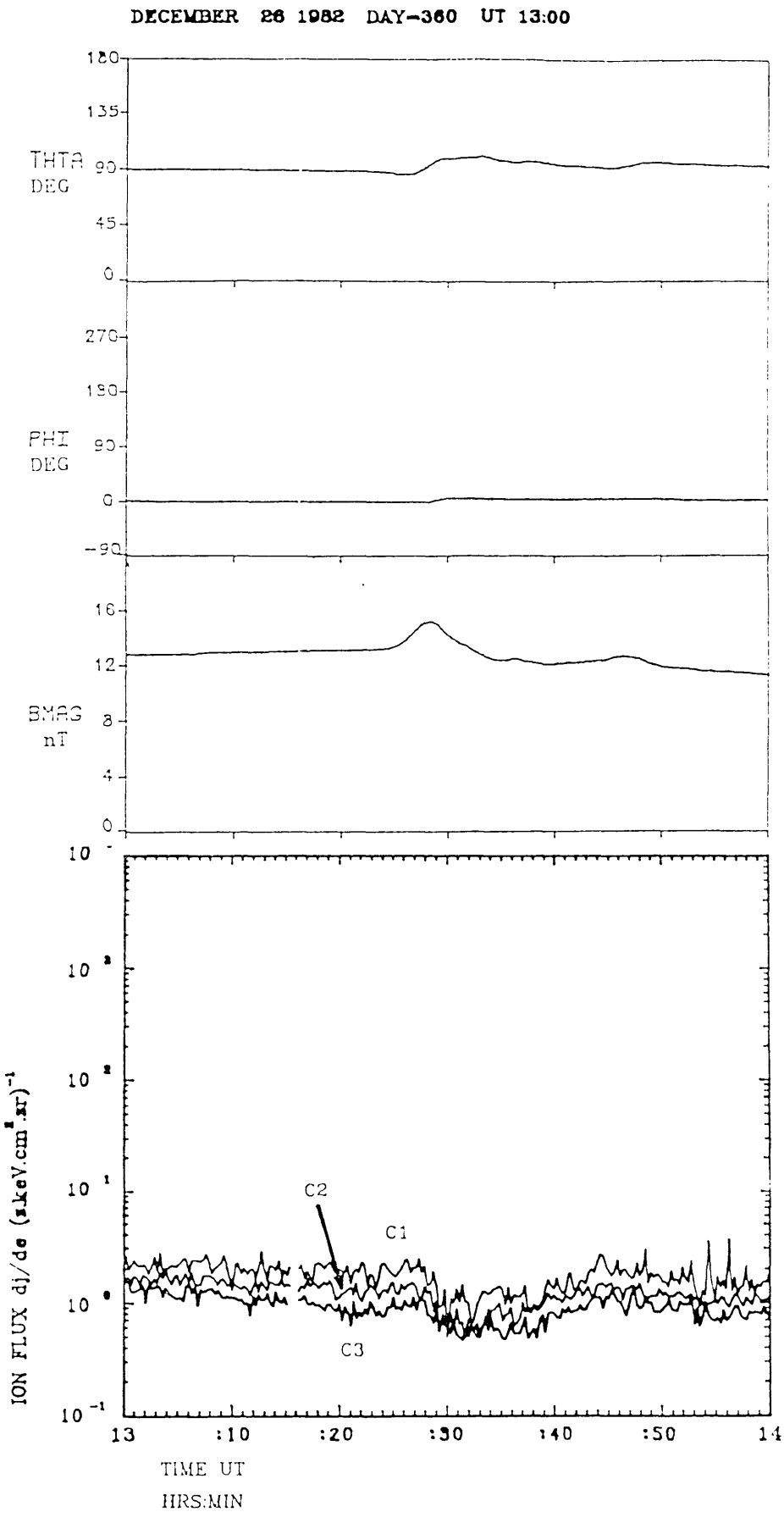


Figure 3.11b. As figure 3.11a for a period of one hour, between 1300 and 1400 UT on December 26 1982.

period show a decrease in ion flux in all three energy channels between 1328 and 1344 UT. As was seen in the previous event the decrease in ion flux becomes less pronounced with increasing energy, and this decrease begins at the peak of the TCR compression. During the second TCR in this period there is no significant decrease in energetic ion flux.

Interpretation

We can interpret these events if we consider the effect of a moving magnetic mirror, formed by the TCR moving along the tail lobe, on the energetic ion distribution (the ion distribution is isotropic in the spacecraft frame of reference). This magnetic mirror would sweep out ions as it travelled along the magnetotail, thus giving rise to the decrease in both the energetic ion fluxes, and the plasma density following the TCR. The minimum pitch angle, α, (in the frame of reference of the TCR) at which ions are reflected from the TCR, depends upon the mirror ratio, that is the pre-TCR magnetic field strength, B_0, divided by the peak magnetic field strength in the TCR, B_m. This angle is given by:

$$\alpha = \sin^{-1}((B_0/B_m)^{0.5})$$

In order to calculate the effect seen in the spacecraft frame of reference we need to know not only the mirror ratio, but also the velocity of the TCR. For both the events considered substorm data is available, and gives velocities of 328 kms^{-1} and 630 kms^{-1} respectively. From the magnetic field data we also find that the mirror ratios are 0.83 and 0.86 respectively. So, in the TCR frame the angle α is 65^0 for the first event and 68^0 for

the second event, thus ions with pitch angles larger than these values, in the TCR frame, will be unable to penetrate the TCR. The transformation back to the spacecraft frame gives pitch angles of 71^{0} and 79^{0}, respectively, for ions of energy 45 keV (the mean energy in the lowest EPAS energy channel). The energy dependence of this transformation is small, eg, for the last event the transformed pitch angle changes from 81^{0} to 78^{0} as the ion energy changes from 35 to 56 keV.

The above calculations imply that the decrease in ion flux should occur only for ions of large pitch angle, indeed for the above events the decrease in ion flux should be confined to the EPAS telescope sectors which nominally view ions with pitch angles of 90^{0}, as the azimuthal sweep for each telescope sector is 45^{0}. Examination of the fluxes of ions with 90^{0} pitch angle and ions with pitch angles close to 0^{0} (not shown) show that this is in fact the case, that is, no effect is seen in the small pitch angle ions, whilst a decrease in flux is seen in the telescope sectors which view ions with 90^{0} pitch angles.

There are two aspects of the observations which remain unexplained. Firstly, the above calculations imply that the decrease in ion flux, seen after the passage of a TCR, should be a steady state effect, so that the ion

flux should not recover after several minutes, as is the case. Secondly, the decrease in energetic ion flux should be only weakly dependent on energy, and should be greater for higher energies, whereas the observed decrease in flux is less at higher energies. Both the above anomalies could be due to the geometry of the TCR; the observed energy dependence might be caused if the mirror ratio varied on the scale of an ion gyroradius, whilst the limited duration of the ion decrease could be caused by ISEE-3 moving onto magnetic field lines which do not intersect the TCR. It is clear that, whilst the decrease in energetic ion flux associated with these TCRs is consistent with the effects of a moving magnetic mirror, further work is required to determine the exact nature of the interaction.

TCRs not showing any effect in energetic ion fluxes

Finally we consider the cases where the observation of a TCR has no effect on the energetic ion flux. In all these cases the background ion flux was extremely low making any significant change difficult to determine. These events will therefore be observed when the spacecraft is too far from the plasma sheet to see the boundary layer, and the lobe ion flux is so low that no decrease in ion flux can be determined due to statistical effects.

Chapter 4

Determination of the thickness of the plasma sheet in the distant magnetotail.

Introduction

In studies of the magnetotail plasma sheet a number of ambiguities can arise due to the use of different terms to describe the same plasma regimes. The magnetotail plasma sheet is generally divided into two regions, the near earth plasma sheet and the distant tail plasma sheet. In the framework of Dungey's open magnetosphere these two regions are usually taken to be the plasma sheet earthward and tailward of the neutral line, (ie on closed and open magnetic field lines respectively) Gosling et al. 1985 use the term current sheet to describe the distant magnetotail plasma sheet, in order to distinguish it from the near earth plasma sheet, whilst Slavin et al. 1985 and Tsurutani et al. 1986 persist with the term plasma sheet. From examination of the current data set it is clear that the terms near earth and distant magnetotail plasma sheet do not adequately delimit regions of different magnetic field topology. In particular, regions of closed magnetic field lines are observed right out to the apogee of ISEE-3 (Slavin et al. 1984) therefore in the current study the latter convention, ie use of the term plasma sheet, will be maintained.

Entry into the plasma sheet is recognized by a diamagnetic decrease in magnetic field strength, relative

to the Lobe magnetic field, and observed adjacent to one of the tail lobes. Studies using plasma data tend to use the plasma temperature to recognize the plasma sheet, but this technique can sometimes wrongly identify the plasma sheet boundary layer as the plasma sheet, and would therefore lead to an overestimate of the plasma sheet thickness. The above method of recognizing a plasma regime as the plasma sheet is verified by energetic ion remote sensing, which allows us to determine the orientation of the plasma region, and so to verify that ISEE-3 enters the plasma sheet and not the magnetosheath. A further characteristic of the events used in this survey is that after entering the plasma sheet there is a reversal in magnetic field direction, implying that ISEE-3 has crossed the central current sheet within the plasma sheet.

Data selection

The data set used in this analysis consisted of 32 events in which it has been possible to determine the thickness of the plasma sheet. The original data set from which this subset was produced consisted of 210 events in which ISEE-3 detected a magnetic field reversal shortly after entering, or before leaving, the plasma sheet. No precise time limit was set for the interval between plasma sheet entry, or exit, and magnetic field reversal,

although in general this interval was less than 5 minutes. Events were not considered if there was any large magnetic field variation observed in the interval between observation of the magnetic field reversal and the edge of the plasma sheet. This condition was imposed in order to eliminate events in which ISEE-3 underwent some complex motion relative to the plasma sheet. Some of these events were in fact complete crossings of the plasma sheet, whilst in other events the plasma sheet was not completely traversed. Events were not included if they showed a large bipolar perturbation in THETA, the polar magnetic field angle, thus removing plasma sheet encounters which were caused by plasmoids (Hones et al., 1984. Richardson and Cowley, 1986). This original data set of 220 events, was then reduced, for a number of reasons; firstly those events in which it was difficult to determine the exact time of entry into, or exit from, the plasma sheet (due to fluctuations in the magnetic field magnitude on the edge of the plasma sheet) were rejected; secondly the events in which the energetic ion data were too disturbed to allow the entry or exit velocity of ISEE-3 to be determined were rejected (this type of event occurred when ISEE-3 spent an extended period in the plasma sheet boundary layer before or after the plasma sheet encounter); and thirdly those events in which EPAS detected no significant increase in energetic ion flux were rejected.

The final data set consisted of two types of events, those in which it was possible to determine the velocity of ISEE-3 relative to the plasma sheet on both entry and exit, and those in which it was only possible to determine the velocity on either entry or exit. In the latter case the half thickness of the plasma sheet was calculated using the time between between ISEE-3's entry to, or exit from, the plasma sheet and the magnetic field reversal, as determined by the reversal in PHI (the azimuthal magnetic field angle). This half thickness was then doubled to give the full plasma sheet thickness. A similar method of calculating the half thickness of the plasma sheet was also employed in events where multiple magnetic field reversals took place during ISEE-3's passage through the plasma sheet, thus removing some of the effects of more complicated plasma sheet motions.

Figure 4.1a) shows one hour of magnetic field data, between 0830 and 0930 UT on March 7 1983 (day 66), combined with the omnidirectional ion flux in the lowest three EPAS energy channels (35-56, 56-91, and 91-147 keV). An example of a plasma sheet crossing from north to south lobe can be seen between 0908:30 and 0915 UT, and is identified by a region of lower magnetic field strength surrounding a reversal in the azimuthal magnetic field angle PHI. Although the angle PHI appears to jump

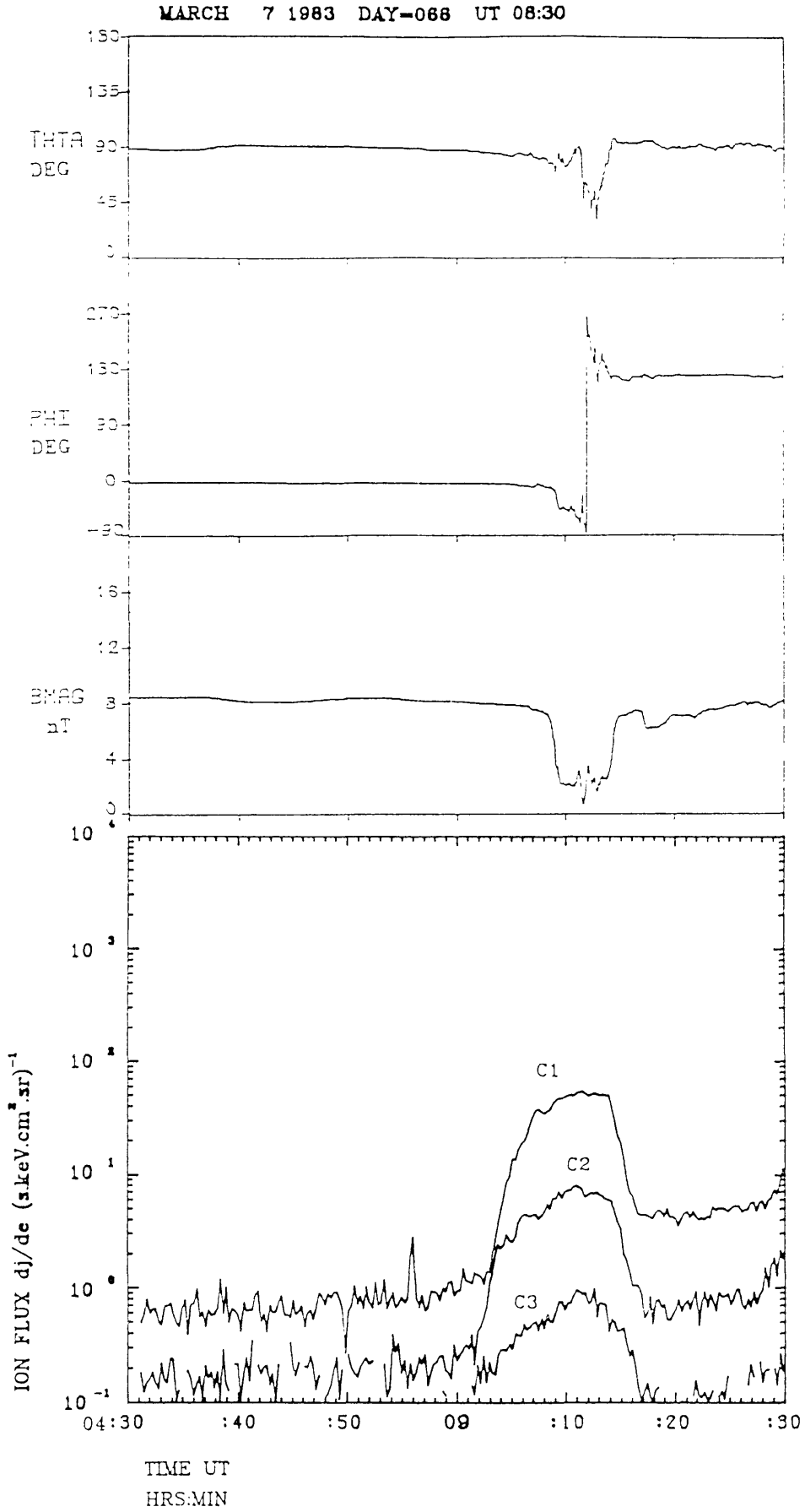


Figure 4.1a) Omnidirectional ion flux, in the 35-56, 56-91 and 91-147 keV energy channels (C1, C2 and C3), compared with the magnetic field magnitude and direction in, GSM coordinates, for a period of one hour between 0830 and 0930 UT on March 7th 1983. THTA and PHI are the polar and azimuthal magnetic field angles respectively.

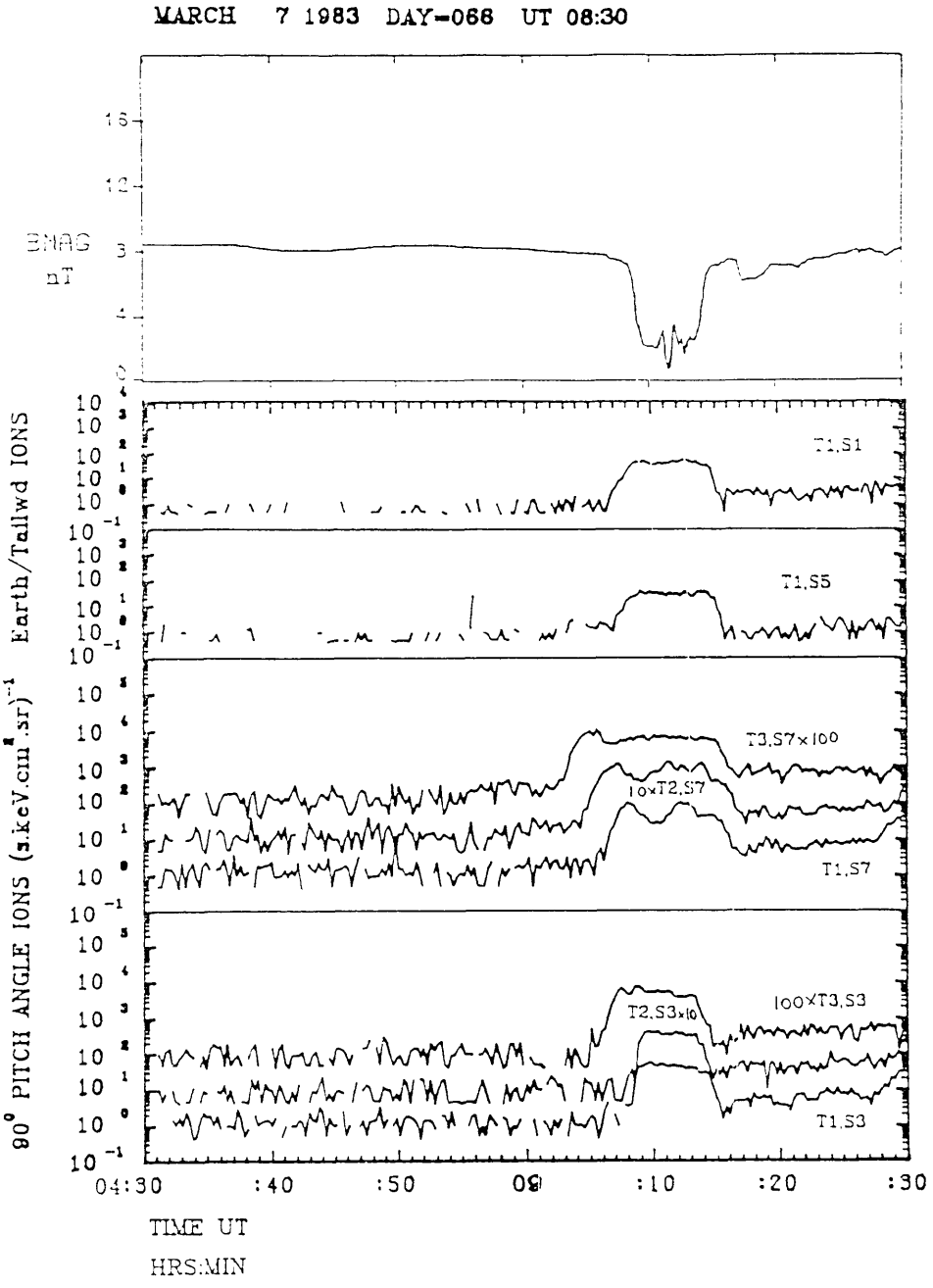


Figure 4.1b) Shows streaming ion and 90^{O} pitch angle ion data, in the 35-56 keV energy channel, between 0830 and 0930 UT on March 7^{th} 1983, compared with the magnetic field magnitude. The top panel shows the magnetic field magnitude, the next two panels show the energetic ion fluxes directed tailward and earthward respectively (from T1,S1 and T1,S5), whilst the lower two panels show energetic ion fluxes from the 6 sectors detecting ions with pitch angle 90^{O} (T3,S7 T2,S7 T1S7 from below ISEE-3 and T3,S3 T2,S3 T1,S3 from above ISEE-3, in the northern tail lobe.). The terminology Tn,Sm refers to telescope n sector m where n ranges from 1 to 3 and m from 1 to 8.

sharply between 0^{O} and 180^{O}, in this event, this is just an artifact of the method of presentation. In fact PHI rotates by 180^{O} slowly from 0^{O}, through -90^{O}. A slow rotation of this type, in PHI, is unusual, but what appears to be a discontinuity in PHI still represents the point at which Bx changes sign from positive to negative, and so can be considered to be the centre of the plasma sheet. At the centre of the plasma sheet the polar magnetic field angle THETA points northwards, from which we can deduce that Bz is positive. From this figure we can also see that there is a wavelike structure in the magnetic field magnitude, during the plasma sheet crossing. It is not possible to determine from the data whether this magnetic field variation is due to a real wave structure, or is just an artifact of a more complicated motion relative to the plasma sheet.

The ion flux is initially low, at less than 1 s^{-1} kev^{-1} cm^{-2} sr^{-1}. An increase in ion flux can be seen in all three energy channels shown, between approximately 0903 and 0916:30 UT. The ion flux does not return to its value prior to the plasma sheet crossing, which may suggest that ISEE-3 remains close to the plasma sheet after exit, or this may be the result of different plasma densities on adjacent sides of the plasma sheet, an observation which was reported by Gosling et al. 1985.

Figure 4.1b) shows the 90^{O} and streaming ion fluxes in the 35-56 keV energy channel, again for a one hour period between 0830 and 0930 UT (the magnetic field magnitude is shown for reference). Two important pieces of information can be gained from this plot; the direction of plasma bulk flow in the plasma sheet, and the entry and exit velocities of ISEE-3 from the plasma sheet. The direction of plasma flow can be inferred from the two traces in the top panel of figure 4.1b), that is, by comparing the earthward and tailward ion fluxes. In this case the tailward ion flux is greater than the earthward ion flux, and so we deduce that the plasma bulk flow is tailward. Daly et al., 1985 have showed that it is possible to calculate the bulk plasma velocity in the plasma sheet (during both a plasmoid event and a simple encounter with the plasma sheet). This calculation is based on the assumption that the energetic ion pitch angle distribution can be represented by an isotropic distribution in the plasma rest frame. The technique of Daly et al. will not be applied in the current work, however, because the plasma sheet thicknesses being measured are of the order of, or in many cases less than, a proton gyroradius in the 35-56 keV energy channel. Instead we will assume that by a comparison of the earthward and tailward directed ion fluxes we can determine the correct direction of bulk plasma flow.

The entry and exit velocities of ISEE-3 relative to the plasma sheet are calculated in the same way as described in chapter 2, by comparing ion rise and decay times in various telescope sector directions detecting ions of pitch angle 90^{O}. In this case ISEE-3 enters the plasma sheet with a velocity of 24 +/- 1 kms^{-1} at an angle of 322^{O} +/- 2^{O} to the GSE Z axis, and exits the plasma sheet with a velocity of 76 +/- 3 kms^{-1} at an angle of 24^{O} +/- 6^{O} to the GSE Z axis. If we use the average of these two speeds, and take the time spent by ISEE-3 in the plasma sheet to be 6.5 minutes a time of flight calculation gives us a plasma sheet thickness of 3.0 +/- 0.2 R_E.

Figure 4.2a) shows one hour of magnetic field data and one hour of omnidirectional ion data in the energy channels 1 to 3, between 2100 and 2200 UT on January 21 1983. As can be seen a plasma sheet crossing occurs at approximately 2130 UT, and is from the southern to the northern tail lobe. The lower, more variable, magnetic field magnitude after the plasma sheet exit suggests that ISEE-3 stays in, or close to the plasma sheet boundary layer for some time. This proximity to the plasma sheet is also indicated by the energetic ion data, with a much higher omnidirectional ion flux after the plasma sheet crossing than before the crossing (up to 20 s^{-1} kev^{-1} cm^{-2} sr^{-1} in the 35-56 kev energy channel after the crossing compared to 1 s^{-1} kev^{-1} cm^{-2} sr^{-1} before). The

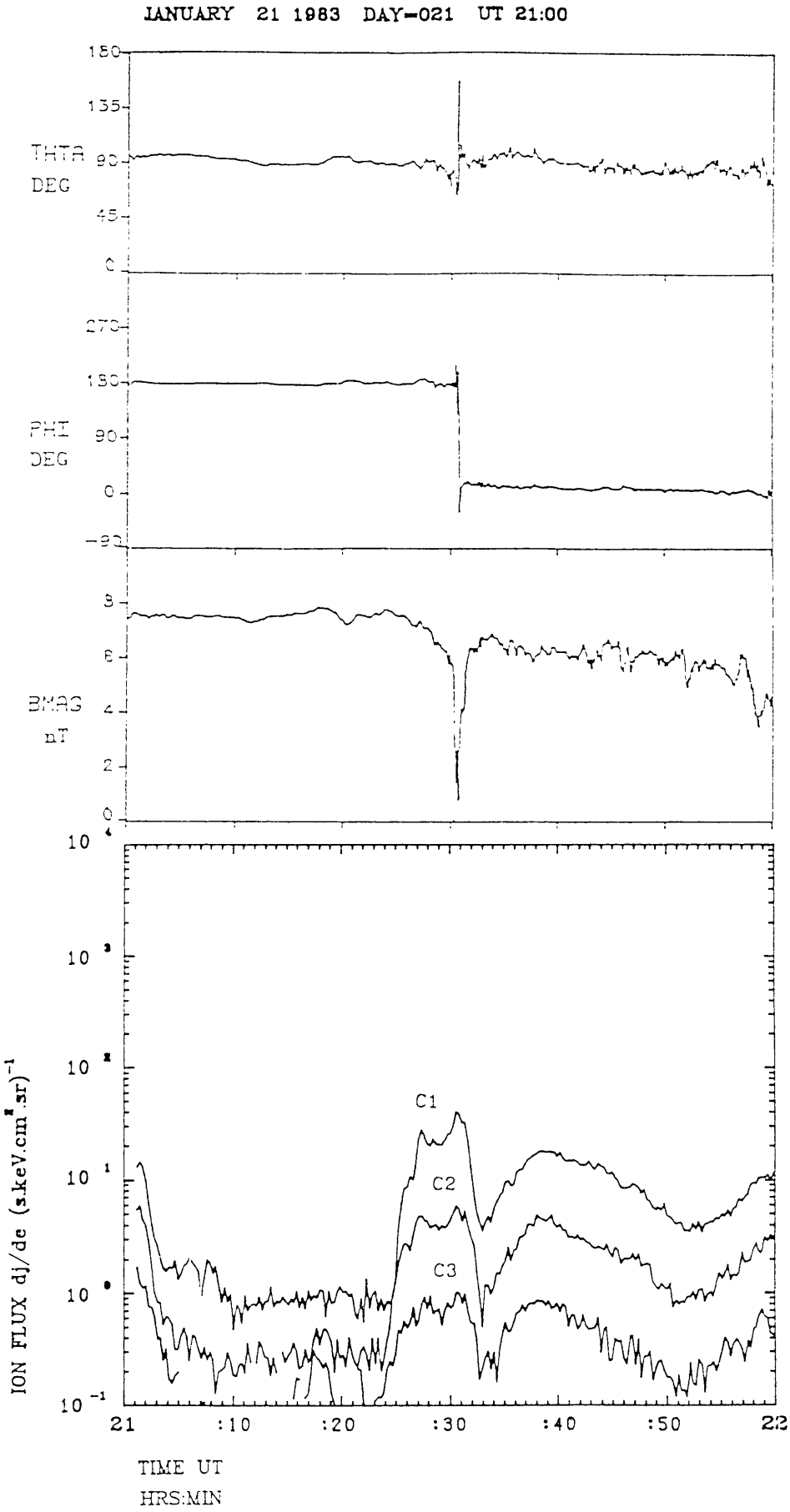


Figure 4.2a) Omnidirectional ion flux, in the 35-56, 56-91 and 91-147 keV energy channels (C1, C2 and C3), compared with the magnetic field magnitude and direction for a period of one hour between 2100 and 2200 UT on January 21st 1983

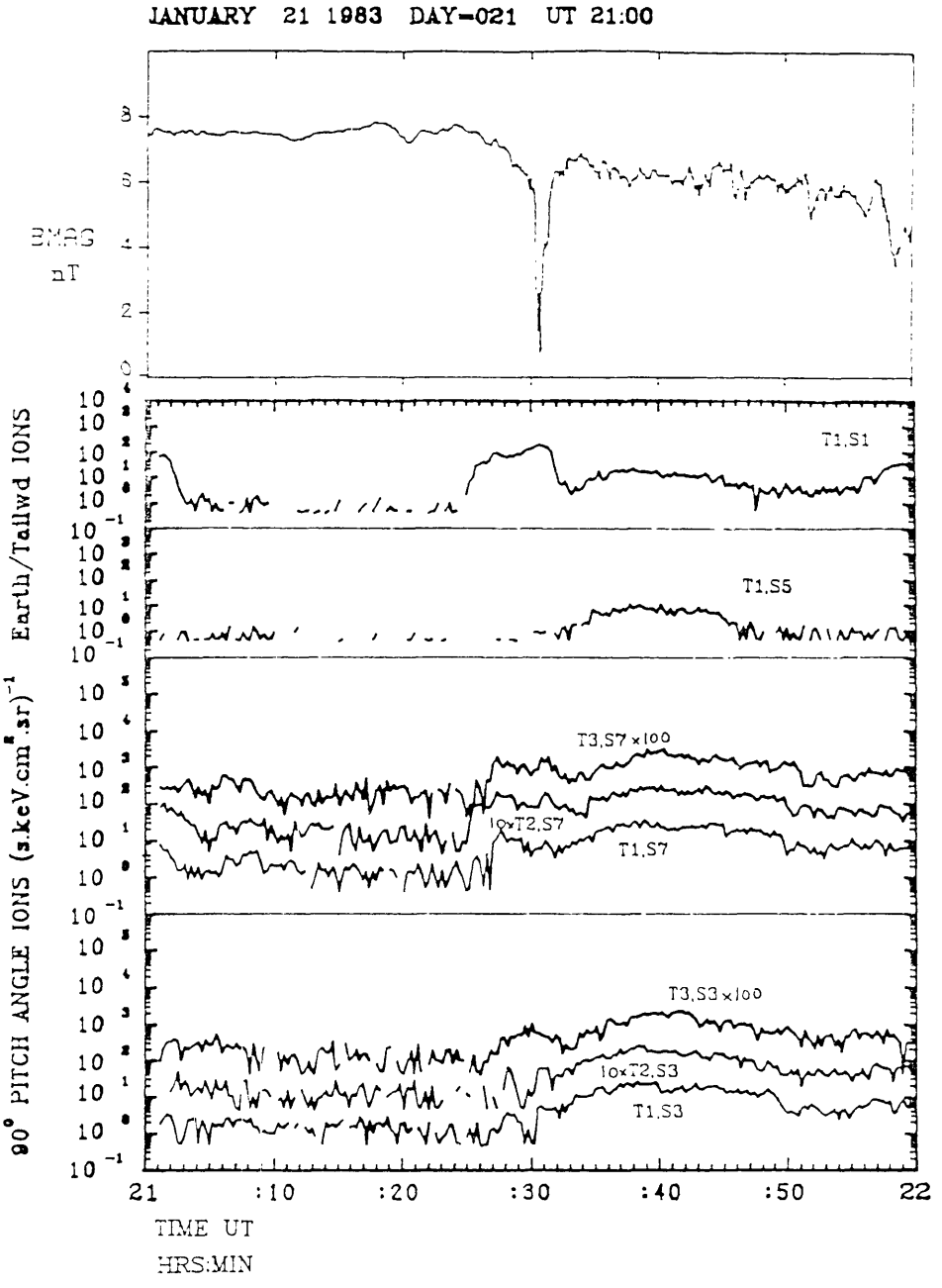


Figure 4.2b) As figure 4.1b) for one hour between 2100 and 2200 on January 21st 1983

polar magnetic field angle THETA varies greatly during the plasma sheet crossing, but from high resolution (6Hz) magnetic field data (not shown) we find that Bz is negative at the point where Bx reverses, thus suggesting that this portion of the plasma sheet is on open magnetic field lines.

Figure 4.2b) shows the earthward and tailward streaming ion data and 90^{O} pitch angle ion data for the above event. As in the previous example the earthward and tailward ion fluxes suggest that the plasma bulk flow is tailwards during the plasma sheet crossing. Using the fluxes of ions with a pitch angle of 90^{O} we can calculate an entry velocity for ISEE-3 into the plasma sheet of 25 +/- 3 kms^{-1} at an angle of 146^{O} to the GSE Z axis. In this case it is not possible to calculate an exit velocity from the plasma sheet, because of the high ion fluxes after the plasma sheet exit (probably due to ISEE-3 remaining in the plasma sheet boundary layer). Using the entry speed of 25 kms^{-1} and taking the time in the plasma sheet to be 2 minutes we can calculate a plasma sheet thickness of 0.47 +/- 0.05 R_E.

The above two examples show calculation of the plasma sheet thickness in the two possible cases, ie with both an entry and exit velocity for ISEE-3, or with only one velocity. It is preferable, of course to have two

velocities per crossing, as this allows us to correct for the effects of acceleration as ISEE-3 crosses the plasma sheet. Two important parameters derived for each crossing were also derived; The direction of plasma bulk flow in the plasma sheet, and the sign of Bz threading through the plasma sheet.

Results of thickness measurements.

Figure 4.3 shows the frequency distribution of plasma sheet thicknesses obtained from the data set of 32 events. The average value for the thickness of the plasma sheet is 1.2 $^{+}_{-}$ 0.8 R_E (7644 $^{+}_{-}$ 5096 km). This value is much smaller than the estimate of 9 - 15 R_E made by Tsurutani et al. 1984a, but it is consistent with the value predicted theoretically by Owen and Cowley, 1987, for the thickness of the quiet time plasma sheet. Tsurutani et al. studied the magnetotail structure at greater than 200 R_E from the earth; their estimate of the plasma sheet thickness was made using a statistical analysis of the time spent by ISEE-3 in the various regions of the magnetotail, which would not be expected to yield as precise a value as that obtained by individual measurements of thickness, and would also tend to include intervals when ISEE-3 was observing plasmoids. It is interesting to note that Tsurutani's technique also suggested that the magnetotail has an elongated cross section in the North-South direction, which is in contradiction of the cross sectional models constructed by Sibeck et al. 1985.

Whilst the average thickness of the plasma sheet is in itself an important result, it is useful to compare this thickness with the other parameters in the data set, and

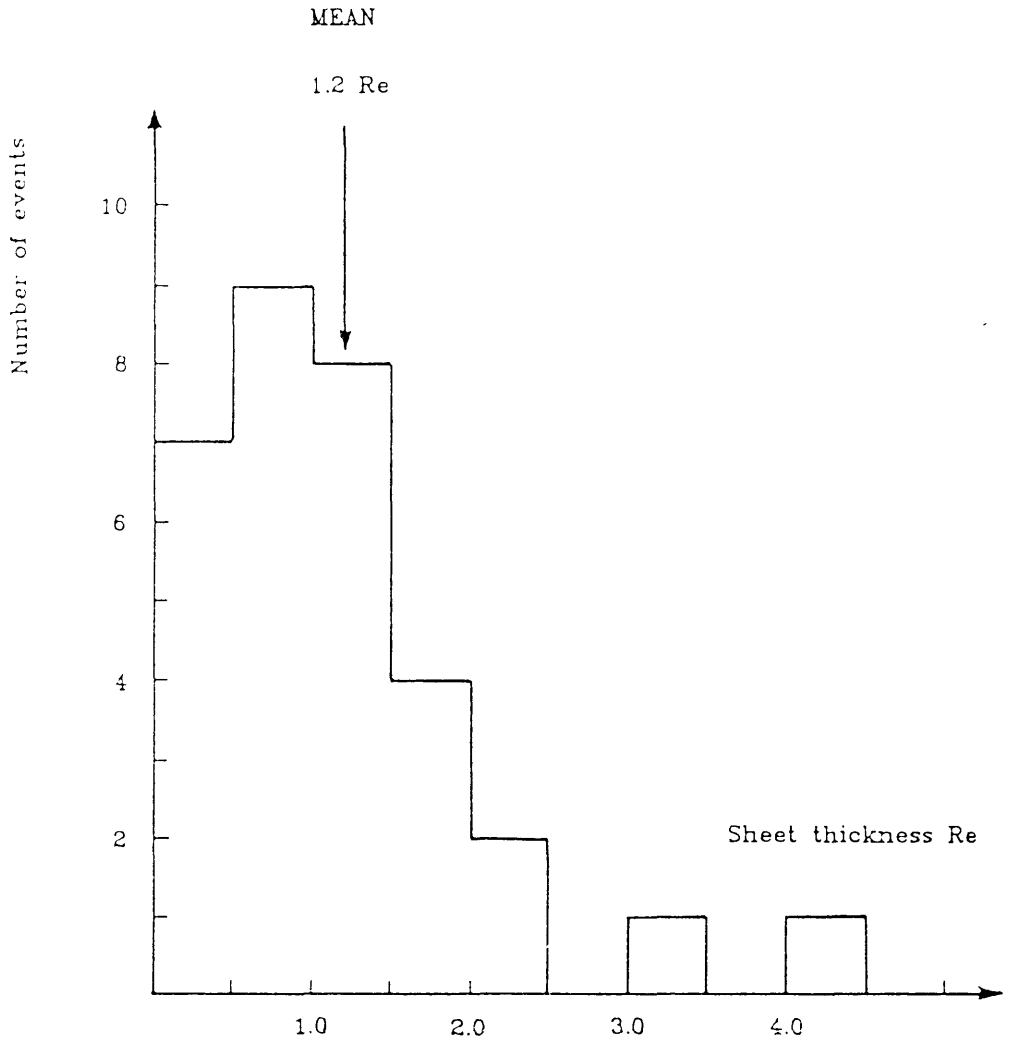


Figure 4.3) Shows a frequency histogram of plasma sheet thicknesses. The average plasma sheet thickness is 1.2 R_E.

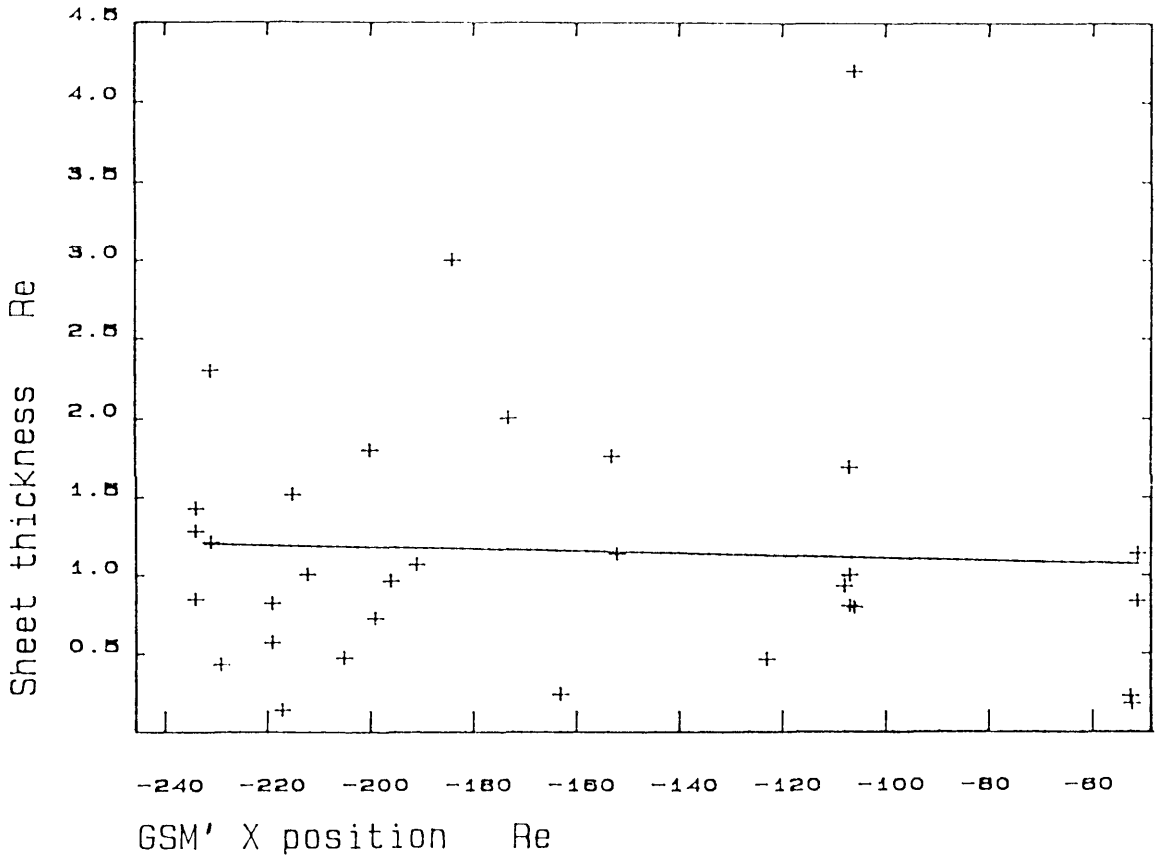


Figure 4.4) Shows a scatter plot of plasma sheet thickness against GSM' X position. The straight line least squares fit to the data is shown for reference; the regression coefficient is 0.06.

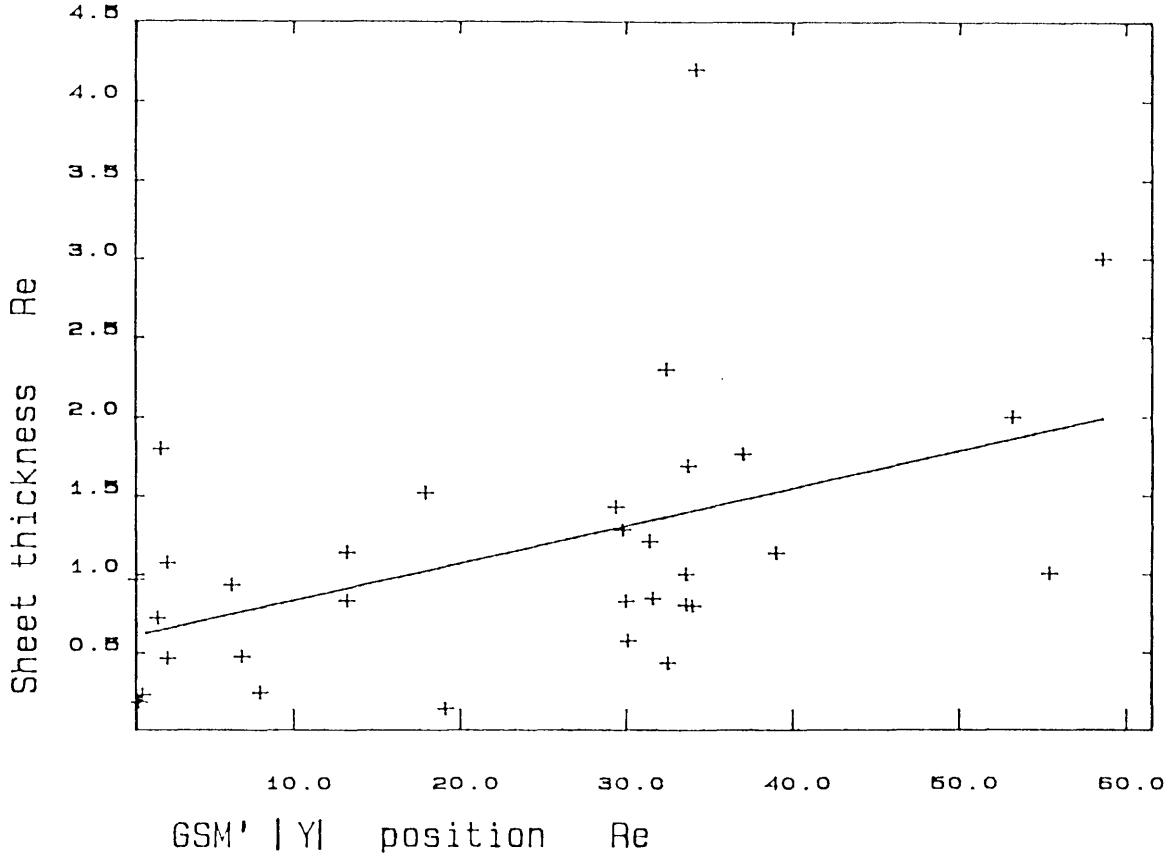


Figure 4.5) Shows a scatter plot of plasma sheet thickness against GSM' |Y|. A linear regression analysis give a regression coefficient of 0.48, and the least sqaures line is shown for reference.

thus to gain some idea of the range of conditions under which this average is valid.

The first set of parameters with which the plasma sheet thickness is compared are those related to position in the magnetotail. As in chapter 3 the coordinate system used to determine position within the magnetotail is an aberrated GSM system, based on a tail aberration angle of 4^{O}. This coordinate system will again be denoted by GSM'.

Figure 4.4) shows the plasma sheet thickness plotted against GSM' X. As can be seen there is no obvious correlation between X and thickness (the regression coefficient is $6x10^{-2}$), but the plot does serve to show the large range in GSM X, between -51.2 and -234 R_E, for which plasma sheet thicknesses were obtained.

It is also of interest to determine if there is any variation of plasma sheet thickness with distance across the plasma sheet, ie in the GSM' Y direction. Figure 4.5) is a plot of plasma sheet thickness against GSM' |Y|, ie the magnitude of GSM' Y. The plot shows that there is a trend for thicker plasma sheets at larger distances from the nominal centre of the plasma sheet. A least squares linear fit to the data gives a regression coefficient of 0.48, which is a significant correlation

at less than the 5% level. The least squares fit of thickness against GSM' Y suggests an average plasma sheet thickness of 0.6 R_E at the centre of the magnetotail, and 2.0 R_E at 60 R_E from the centre. One unexpected feature of Figure 4.5) is that the range of GSM' |Y| values for which plasma sheet thicknesses were obtained is from 0 to 59 R_E, in contrast to a nominal radius for the magnetotail of 30 R_E reported by Slavin et al. 1985 (Slavin's value was calculated from a survey of 756 magnetopause crossings). Whilst it is possible that, at certain times, the magnetotail radius could be greater than 30 R_E in the GSM Y direction (Sibeck et al., 1985), the observed discrepancy is probably due to variations in the magnetotail aberration angle. A decrease in the aberration angle from 4^O to 0^O would mean that the centre of the magnetotail at 220 R_E GSM' X was at 15 R_E GSM' Y.

Plasma flow and magnetic field topology.

As has been mentioned previously, from the examination of the earthward and tailward directed ion fluxes it is possible to determine the direction of bulk plasma flow in the plasma sheet. From the data set of 32 events only three were found in which the plasma bulk velocity was earthwards. Two of these events occurred at -52 R_E GSM' X, whilst the third occurred at -173 R_E GSM' X. Interpreted in terms of an open magnetosphere, earthward plasma flow suggests that during these observations ISEE-

3 was earthward of an active reconnection line, across the plasma sheet.

In simple open models of the magnetosphere (Dungey 1961) magnetic field topology in the plasma sheet is directly related to plasma flow direction, ie in the plasma sheet, tailward flowing plasma lies on open magnetic field lines, whilst earthward flowing plasma lies on closed field lines. More complex models (eg. Slavin et al. 1985) suggest that this direct correspondence may not always be the case. In order to determine which type of model this data set supports we need to have some way of determining the magnetic field topology, and we have this from the sign of Bz across the plasma sheet.

The value of Bz closest to the reversal in Bx was determined from listings of 6 Hz magnetic field data; this value was taken to be representative of the magnetic field threading through the plasma sheet. In two of the cases Bz was highly variable across the plasma sheet, and so these events were not used in the following analysis. From the 30 events considered, 7 had Bz less than zero, suggesting open magnetic field lines, whilst 23 had Bz greater than zero, suggesting closed magnetic field lines. The average plasma sheet thickness for the cases where Bz was negative was 1.6 +/- 1.1 R_E, and for the cases where Bz was positive the average thickness was

1.0 +/- 0.7 R_E. Whilst these values seem to suggest that the plasma sheet is thicker when Bz is negative, ie, when the plasma sheet is on open magnetic field lines, it is impossible to draw a firm conclusion due to the poor statistics involved.

This simplistic approach to determining the magnetic field topology by using GSM Bz has one drawback; GSM Bz will only give a correct indication of whether the magnetic field in the plasma sheet is open or closed if the plasma sheet is parallel to the GSM X-Y plane, that is Bz is the magnetic field component perpendicular to the plasma sheet. In determining the entry or exit velocity of ISEE-3 relative to the plasma sheet the inclination of the plasma sheet in the GSM Y-Z plane is also determined, and so this measurement can be used to check the validity of the assumption that the plasma sheet lies parallel to the GSM X-Y plane (it will be assumed that the plasma sheet is not inclined to the GSM X axis, that is, any inclination only occurs in the GSM Y-Z plane). Figure 4.6 shows a histogram plasma sheet inclination in the GSM Y-Z plane against frequency of occurrence. The inclination is expressed as the angle between the plane of the plasma sheet and the GSM Y-Z axis, as determined by ISEE-3's average velocity relative to the plasma sheet. This figure shows that the orientation of the plasma sheet in the GSM Y-Z plane is

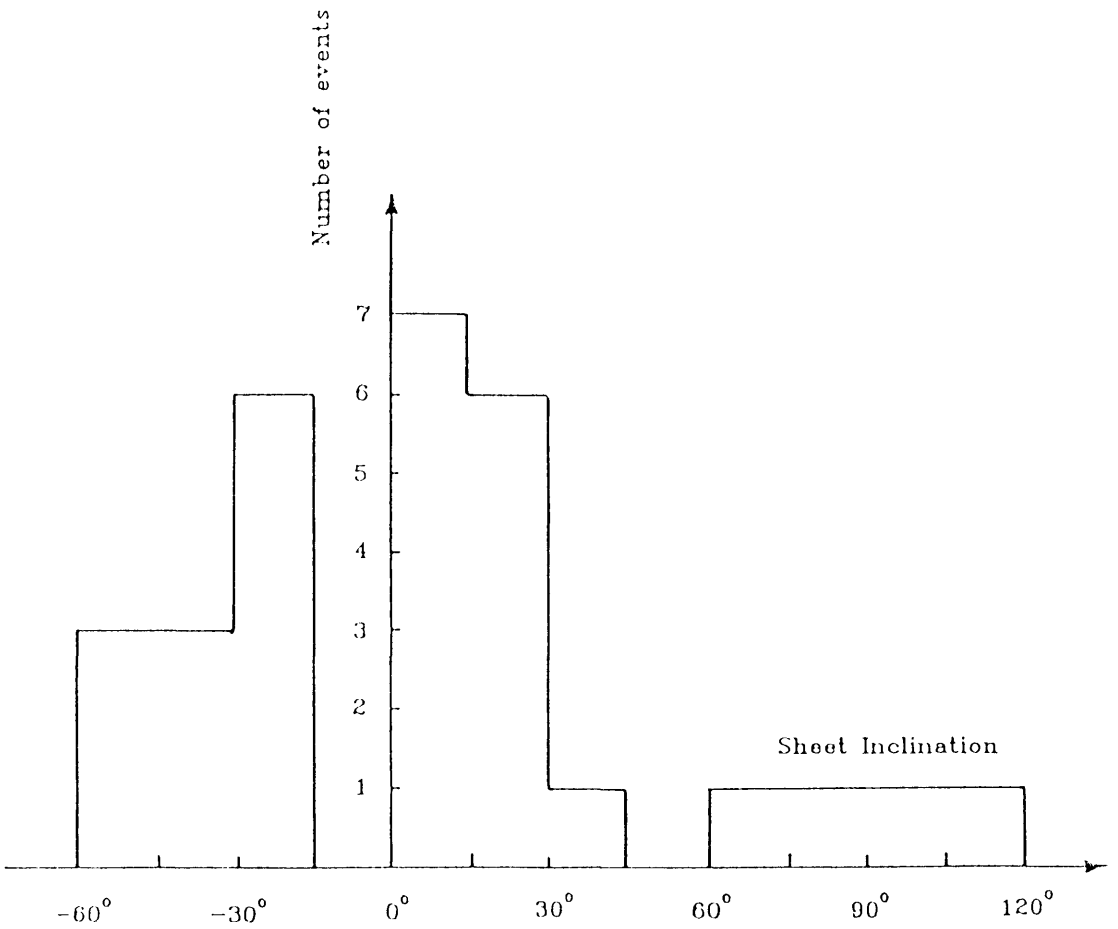


Figure 4.6) Shows a frequency histogram of plasma sheet inclination, obtained by sensing remotely ISEE-3's velocity relative to the plasma sheet.

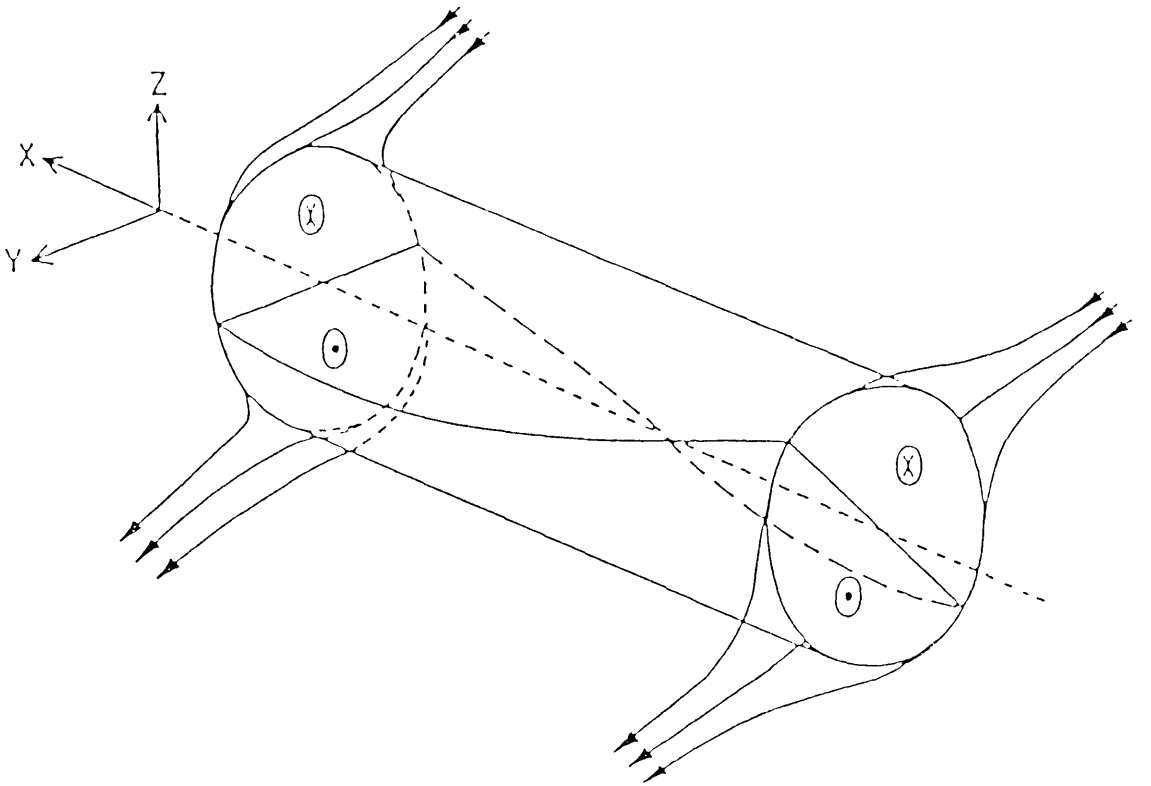


Figure 4.7) (after Cowley 1981) Shows the twist on the magnetotail resulting from the penetration of the IMF when IMF By is positive. X,Y and Z refer to GSM coordinates.

very variable, and so casts doubt on the validity of using GSM Bz as a measure of the magnetic field threading through the plasma sheet. The large variation in plasma sheet inclination could come from two sources Firstly, in the steady state the interplanetary magnetic field (IMF) is expected to penetrate the magnetotail, and the resulting stresses would produce a twist on the magnetotail as a whole. This effect was predicted by Cowley, 1981, and observational evidence was presented by Sibeck et al., 1985. Figure 4.7) (after Cowley 1981) shows the effects of penetration of the IMF into the magnetotail, for IMF By positive. The resulting twist would be reversed for IMF By negative. Secondly the magnetotail is in continual motion, due to the exitation of the magnetotail's own normal modes (Erskovich and Nusinov 1972, Sibeck et al., 1987) and the effects of variations in the solar wind speed and direction, a fact which is almost certainly responsible for ISEE-3's encounters with the plasma sheet, shown in this data set.

The data shown in figure 4.6) suggests the need to find some alternative method of quantifying the magnitude of the magnetic field threading through the plasma sheet. As we already know the orientation of the plasma sheet in the GSM Y-Z plane, we can develop a coordinate system in which to express the magnetic field, that is ordered relative to the plasma sheet. The plasma sheet

coordinate system has its X axis parallel to the aberrated GSM X axis, whilst its Y and Z axes form an orthogonal pair, with Z perpendicular to the plasma sheet and Y in the plane of the plasma sheet. The analogue of Bz in plasma sheet coordinates can be obtained by a rotation of the GSM magnetic field components in the GSM Y-Z plane, and will be denoted by $B_{\hat{e}}$. One possible drawback of a coordinate system produced in this way is that it is based on a measurement taken locally, and so may not be representative of the plasma sheet as a whole. Some idea of the degree of localization of the plasma sheet coordinate system is given by the gyroradius of the ions used to sense remotely the plasma sheet when determining ISEE-3's relative velocity; for the velocities used in this study ion data from the 35-56 keV energy channel were used, assuming that these ions were protons, this gives a mean gyroradius of 0.5 R_E. Thus the plasma sheet coordinate system which we have developed would be expected to be valid over a scale length of at least 0.5 R_E, which is of the same order as the plasma sheet thicknesses calculated, and so can be considered to be quite adequate for the work in question.

Using the plasma sheet coordinate system, we find that 11 of the events show $B_{\hat{e}}$ to be less than zero, implying that the section of the plasma sheet observed is on open magnetic field lines, whilst 19 of the events have $B_{\hat{e}}$

positive, implying closed magnetic field lines. The average thickness for $B_{\hat{e}}$ negative is 1.5 +/- 1.0 R_E and for $B_{\hat{e}}$ positive is 1.0 +/- 0.7 R_E. These values are not qualitatively different from the values obtained using GSM Bz, even though the number of events in which the plasma sheet is thought to be on open magnetic field lines has increased to just over 35% of the events sampled.

The above results suggest that in a significant number of the events studied the plasma sheet was on closed magnetic field lines, and yet the bulk plasma flow was tailward. Comparison of $B_{\hat{e}}$ with position data yields no obvious relationship between magnetic field topology and position in the magnetotail, but does show that closed magnetic field lines are observed up to 230 R_E down the magnetotail. This type of result is not new, and was interpreted by Slavin et al. 1985 in terms of a curved neutral line across the plasma sheet. Figure 4.8) shows a reproduction of Slavin's model for the average configuration of the quiet time neutral line. As can be seen, on the flanks of the magnetotail the average position of the neutral line is well beyond 230 R_E, and whilst the results in this study show no positional dependence for the magnitude of $B_{\hat{e}}$ they are consistent with this model. The idea of a curved neutral line was first put forward by Russell (1977) who suggested that it

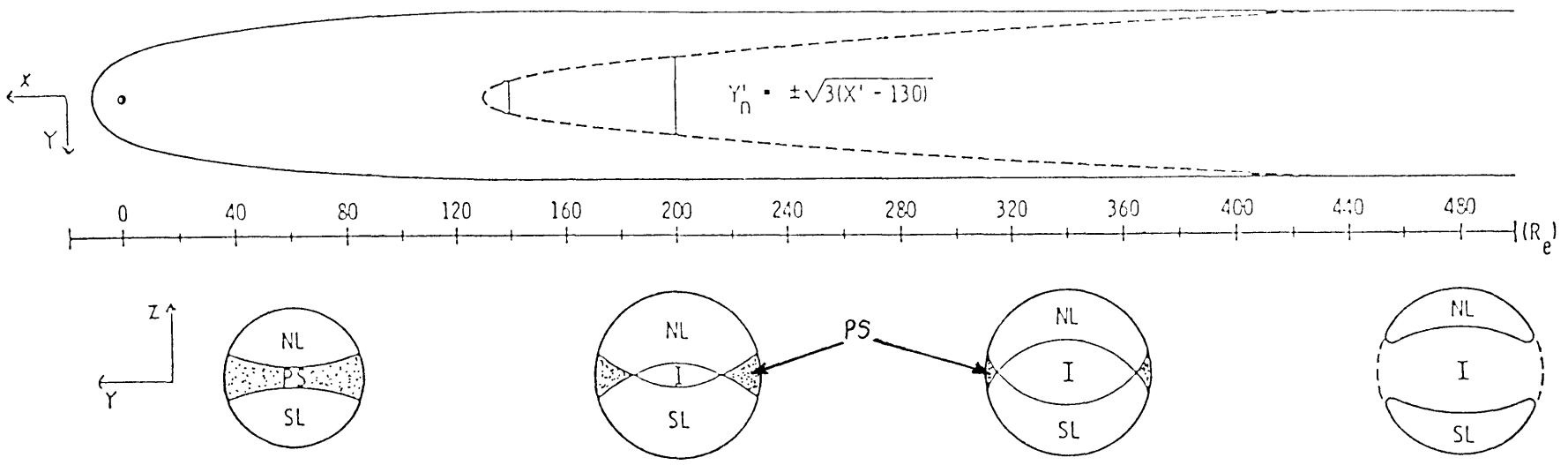


Figure 4.8) A model of the average distant tail magnetic field topology based on a curved neutral line. The upper part of the figure is a cut in the X-Y plane, with a model neutral line shown dashed. The bottom part of the figure shows four cuts through the magnetotail parallel to the Y-Z plane. NL signifies the northern tail lobe SL the southern tail lobe, PS the plasma sheet, and I interplanetary magnetic field lines. After Slavin et al., 1985.

may be due to stress placed on the magnetotail by a viscous interaction with the solar wind.

CHAPTER 5

Magnetotail flux ropes.

Introduction

Observations consistent with the existence of flux ropes, ie, magnetic flux tubes which are twisted, in the distant magnetotail have been reported by Siscoe et al. 1984 and Sibeck et al. 1984. Some of the energetic particle characteristics of these events were reported by Scholer et al. 1985. All these papers dealt with the same three events, which occurred between 0220 and 0235 UT on December 28 1982, (Event 1), between 0450 and 0510 UT on December 30 1982, (Event 2), and between 0710 and 0730 UT on March 25 1983, (Event 3). These events were interpreted as encounters with flux ropes whose axes were in the GSM X-Y plane and almost parallel to the GSM X axis. To date these are the only reported observations which are consistent with the existence of such flux configurations in the distant magnetotail. In this chapter we examine the energetic ion characteristics of these events, as seen from ISEE-3 EPAS data, and compare our results with those obtained previously.

Magnetic field observations.

Figure 5.1 shows the magnetic field observations for the three events, as measured by the vector helium magnetometer on board ISEE-3 (from Sibeck et al. 1984) As can be seen, each event can be characterized by a bipolar magnetic field change in one field angle, either BLAT (the polar angle) or PHI (the azimuthal angle), and a

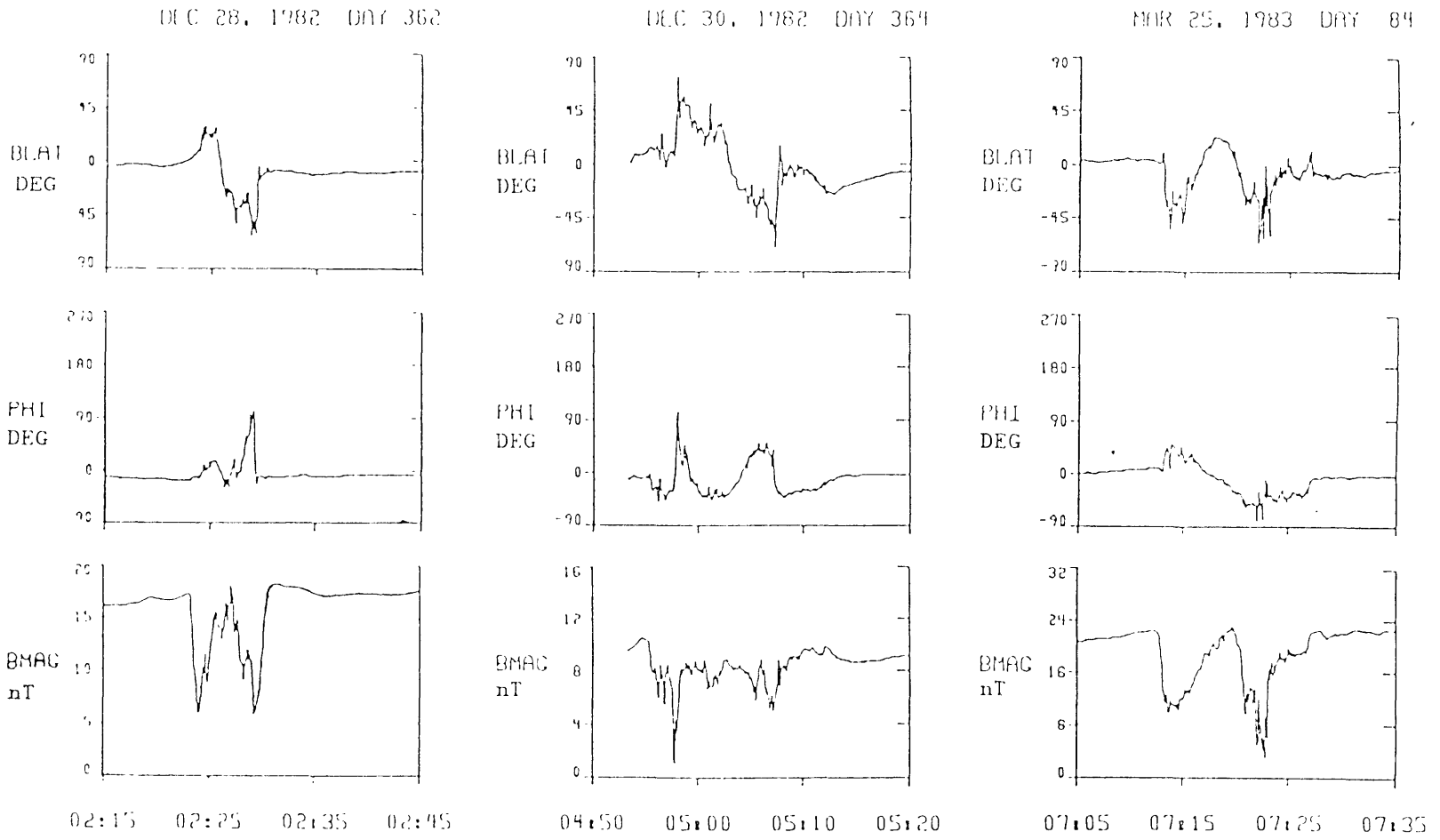
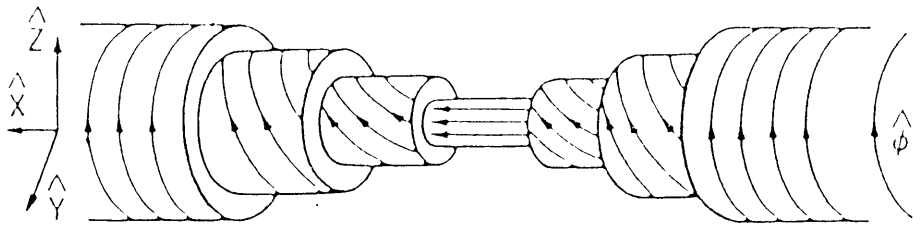


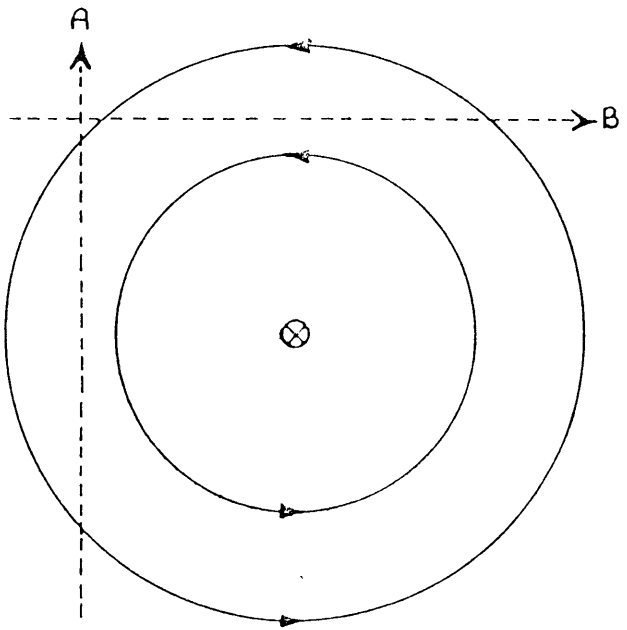
Figure 5.1. Magnetic field magnitude and direction for the three flux rope events; between 0215 and 0245 UT on December 28th 1982 (event 1), 0450 and 0520 UT on December 30th 1982 (event 2) and 0705 and 0735 UT on March 25th 1983 (event 3). BMAG is the magnetic field magnitude, BLAT the polar angle and PHI the azimuthal angle. After Siscoe et al. 1984.

double peaked signature in the other field angle. There is a strong magnetic field at the centre of each event, which is approximately the same magnitude and strength as the lobe magnetic fields before and after the event. This type of magnetic field signature is similar to that observed for flux ropes seen in the Venus ionosphere (Russell and Elphic 1979) and can be explained by the spacecraft moving through a structure similar to the one shown in figures 5.2a and 5.2b, embedded in the magnetotail lobe with its axis parallel to the GSM X axis. A bipolar magnetic field signature in the polar angle would be produced by passing through the structure parallel to the GSM X-Y plane, (across the tail, eg trajectory B in figure 5.2b). A passage through the structure perpendicular to the GSM X-Y plane (in the north-south direction, eg trajectory A in figure 5.2b) would produce a bipolar signature in the azimuthal magnetic field angle. This suggests that the events 1 and 2 are caused by flux rope crossings parallel to the GSM X-Y plane, whilst event 3 is caused by a flux rope crossing perpendicular to the GSM X-Y plane, as is also suggested by Scholer et al. 1985. As the hypothetical flux ropes have their axes parallel to the GSM X axis, we should be able to use energetic ion remote sensing to determine the geometry, in the GSM Y-Z plane, of each crossing.



FROM
RUSSELL AND ELPHIC
(1979)

a) INTERIOR STRUCTURE OF FLUX ROPE



b) Cross section through a model flux rope

Figure 5.2a. Model structure of a flux rope, showing the change from azimuthal to axial magnetic field at the core of the structure. 5.2b Section of a model flux rope perpendicular to the axis, together with two possible spacecraft trajectories; (A) producing a bipolar signature in the azimuthal magnetic field angle, (B) producing a bipolar signature in the polar magnetic field angle.

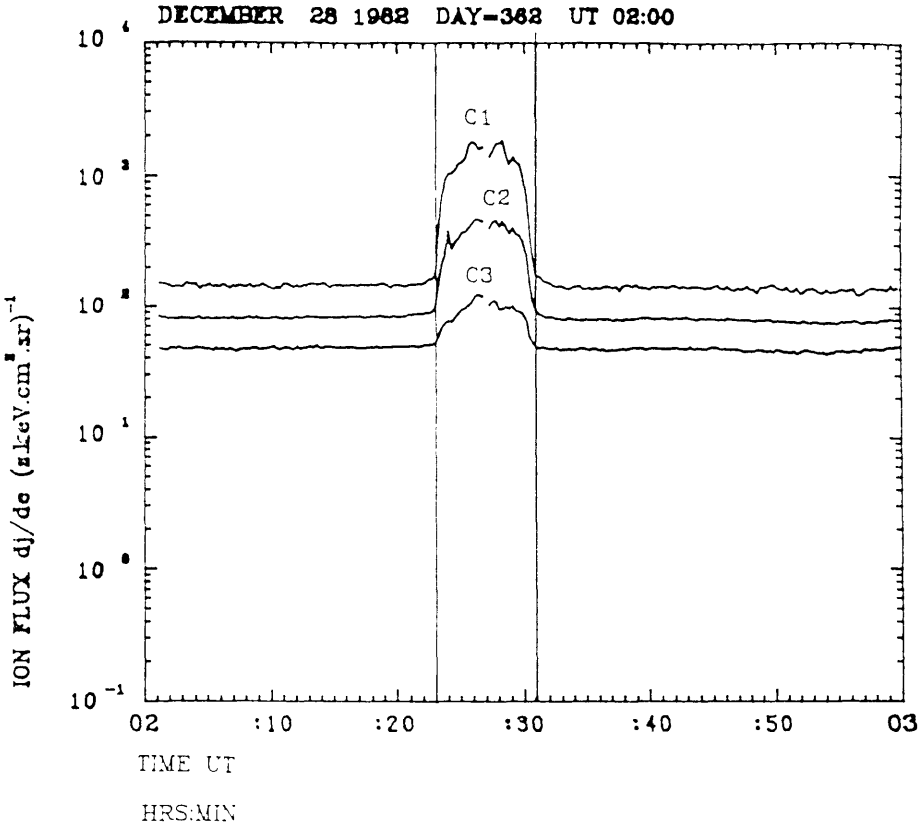


Figure 5.3a. Omnidirectional energetic ion fluxes for the 35-56, 56-91 and 91-147 keV energy channels (C1,C2 and C3 respectively), between 0200 and 0300 UT on December 28th 1982 (event 1). The extent of the magnetic field structure is shown by vertical lines.

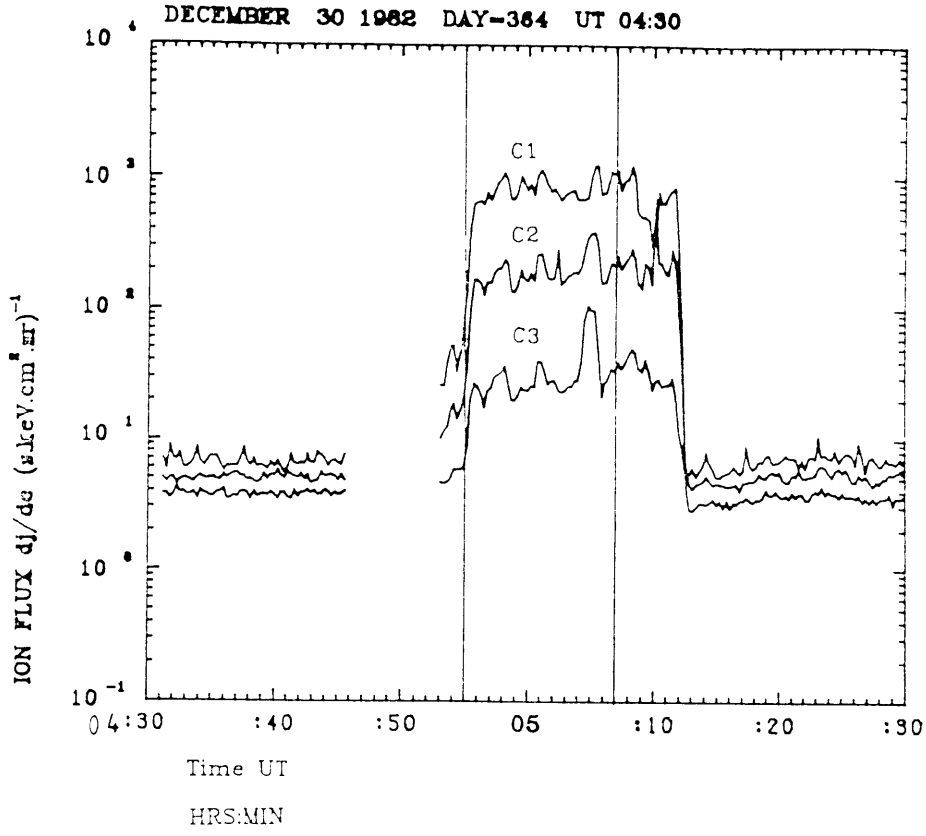


Figure 5.3b. As figure 5.3a, for the period between 0430 and 0530 UT on December 30th 1982 (event 2).

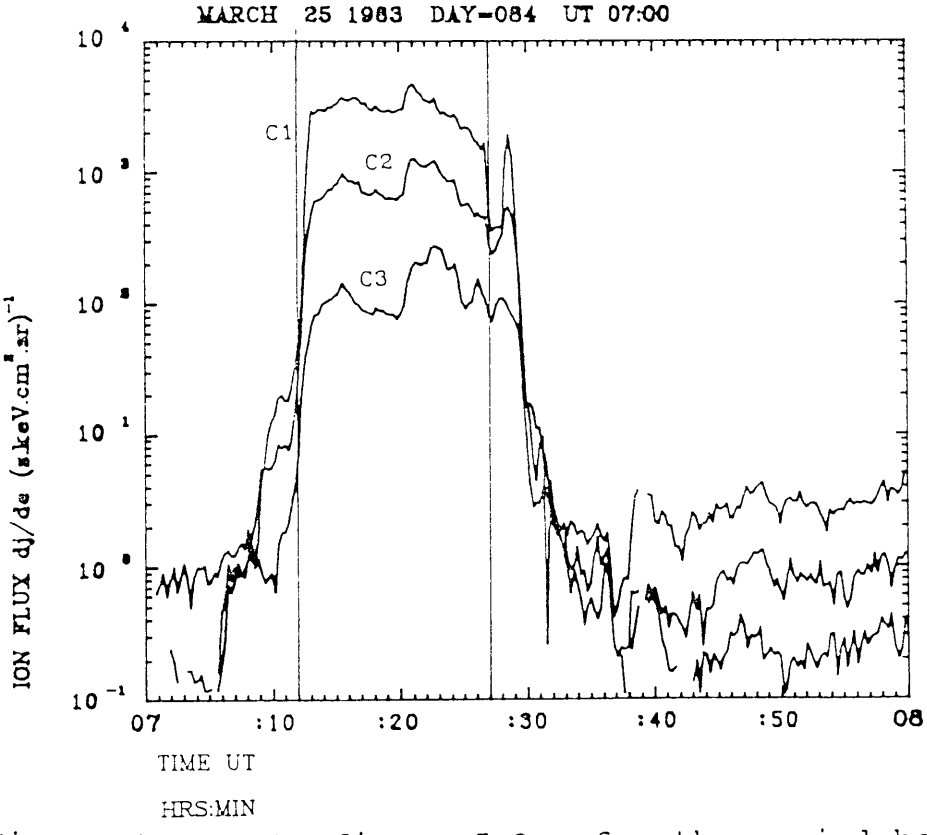


Figure 5.3c. As figure 5.3a, for the period between 0700 and 0800 UT on March 25th 1983 (event 3).

Energetic ion observations.

Figures 5.3a, b and c show the omnidirectional ion flux for the three flux rope events, in the 35-56 keV, 56-91 keV, 91-147 keV and 147-238 keV energy channels. The approximate duration of each event in the magnetic field is shown by vertical lines. As can be seen each event shows a large enhancement in the omnidirectional ion flux, but events 1 and 2 are complicated by the presence of unusually high ion fluxes in the tail lobes prior to and following the flux rope encounters. These high lobe fluxes were commented upon by Scholer et al., 1985, and are thought to be due to a solar particle event. The presence of this high background flux restricted the analysis of Scholer et al. somewhat, and so they performed a remote sensing analysis on the event 3 only. Figures 5.4, 5.5 and 5.6 show 90^{O} pitch angle ion fluxes, together with tailward and earthward streaming ion fluxes for the three flux rope events. The duration of each event, in the magnetic field, is again shown by vertical lines on each plot. As can be seen from these three figures, each event causes a significant enhancement in the 90^{O} pitch angle ion fluxes despite the presence of solar particle event ions. Using the times of the increase and decrease of 90^{O} pitch angle ion fluxes, as in previous chapters, it is possible to calculate the velocities of ISEE-3 relative to the flux rope on entry and exit.

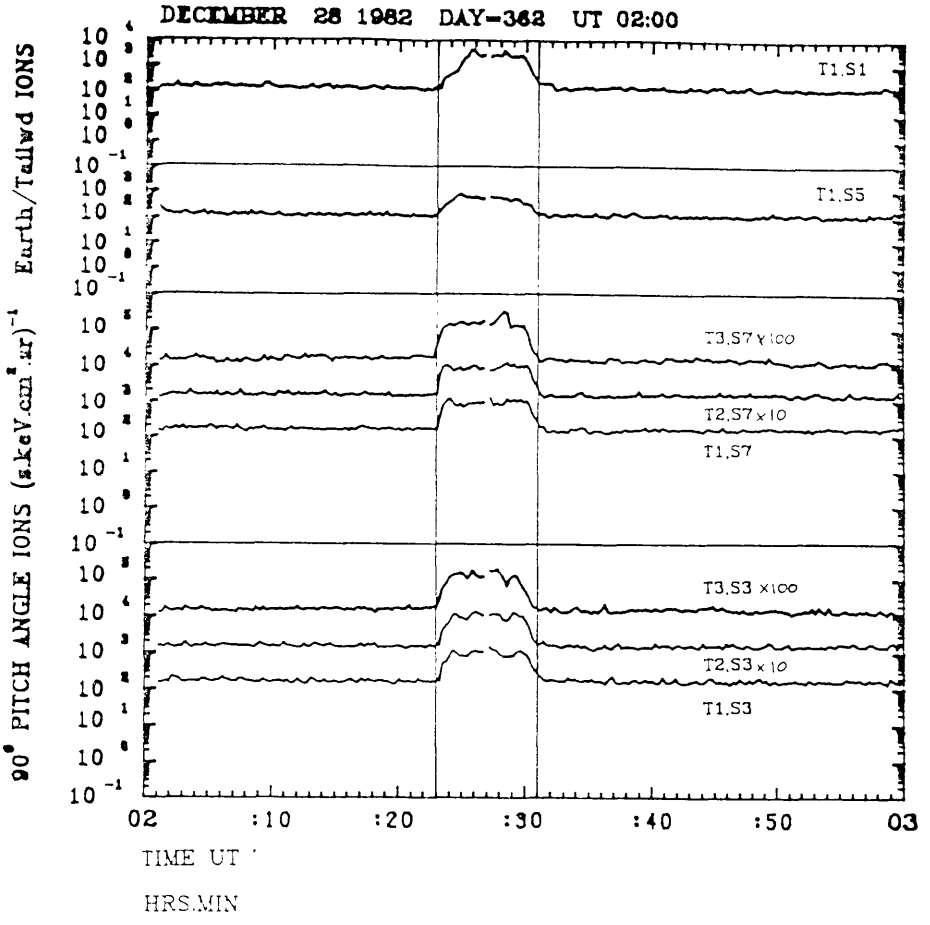


Figure 5.4 Plot of 90^{O} pitch angle, earthward and tailward streaming ion fluxes in the 35-56 keV energy channel between 0200 and 0300 on December 28^{th} 1982 (event 1). The top two panels show the energetic ion fluxes directed tailward and earthward respectively (T1,S1 and T1,S5), whilst the lower two panels show energetic ion fluxes from the 6 sectors detecting ions with pitch angle 90^{O} (T3,S7 T2,S7 T1S7 from below ISEE-3 and T3,S3 T2,S3 T1,S3 from above ISEE-3, in the northern tail lobe.). The terminology Tn,Sm refers to telescope n sector m where n ranges from 1 to 3 and m from 1 to 8. Vertical lines mark the approximate duration of the event in the magnetic field data.

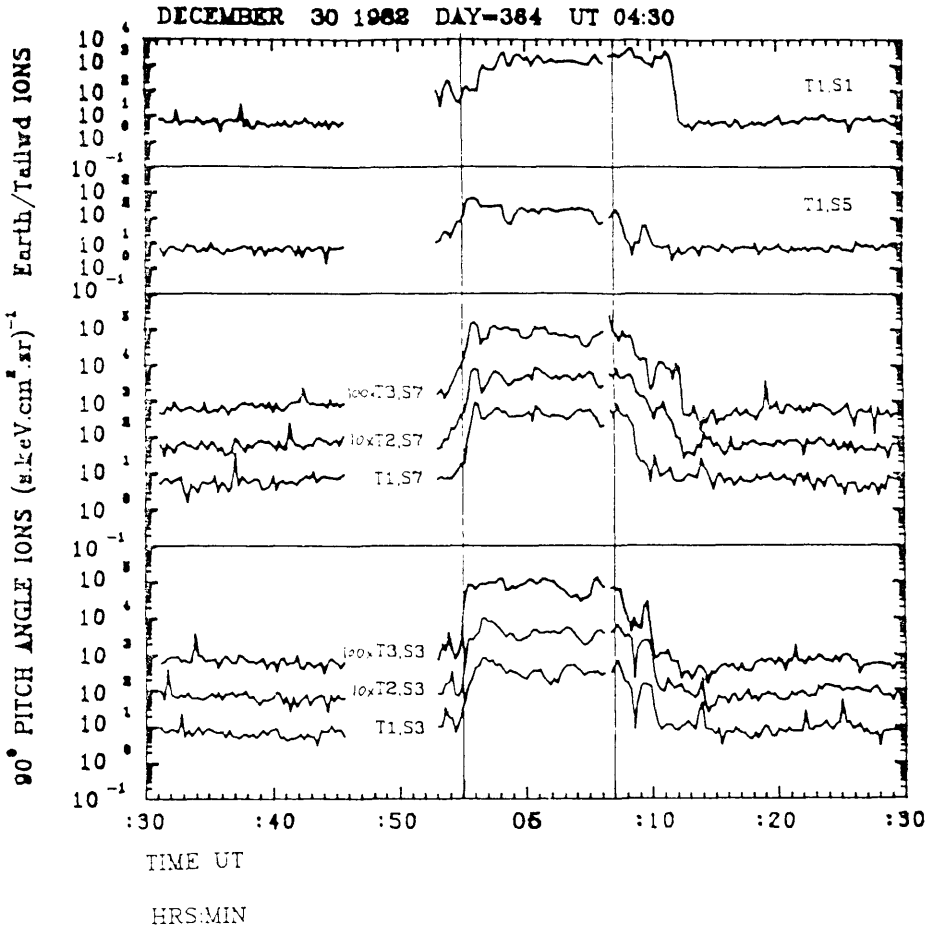


Figure 5.5. As figure 5.4, for the period between 0430 and 0530 UT on December 30th 1982 (event 2).

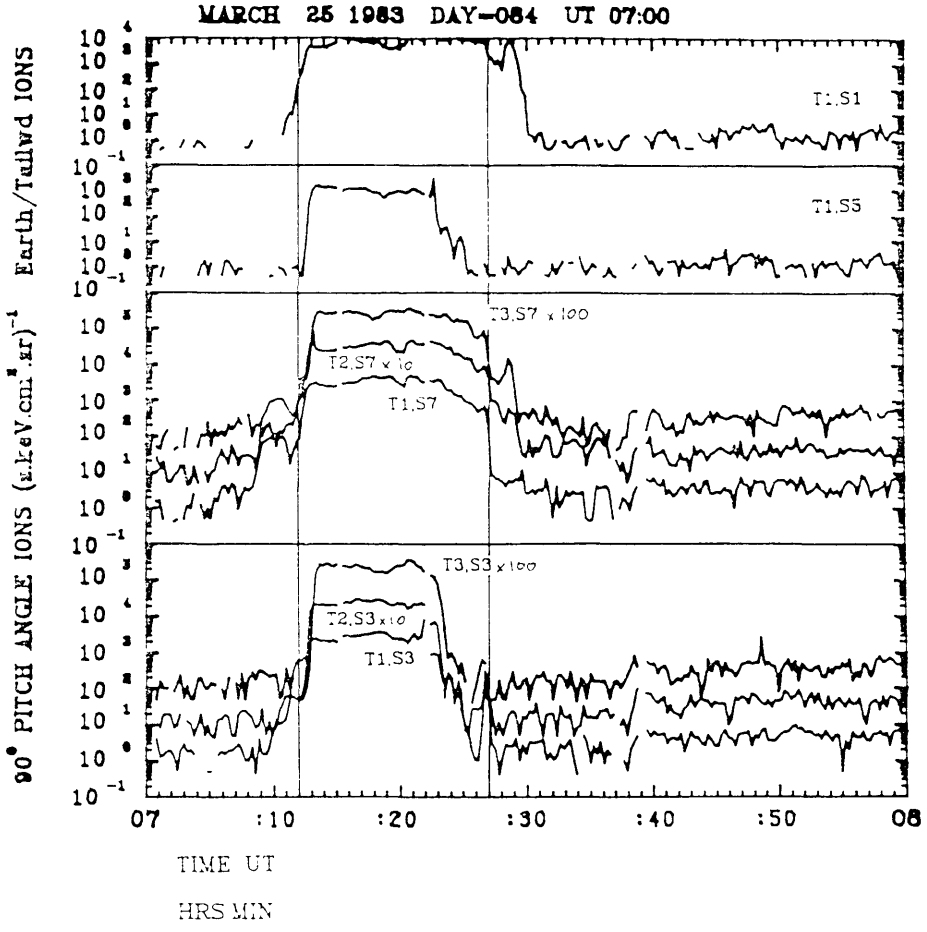


Figure 5.6. As figure 5.4, for the period between 0700 and 0800 UT an March 25th 1983 (event 3).

Table 1

EVENT	1	2	3
ENTRY vel =	120+/-6 kms^{-1}	140+/-7 kms^{-1}	44+/-2 kms^{-1}
ϕ_m =	153^o	79^o	262^o
EXIT vel =	77+/-4 kms^{-1}	81+/-4 kms^{-1}	8+/-2 kms^{-1}
ϕ_m =	51^o	341^o	10^o

Table 1 shows these velocities for each event, together with the angle of the velocity vector to the GSM Z axis ϕ_m (Positive towards GSM Y).

Figure 5.7 shows these velocities projected onto model cross sections of a flux rope. It is possible, using figure 5.7, to compare magnetic field configuration of the observed structures with that expected of an ideal flux rope.

Considering Event 1 (figure 5.7a) we see that the magnetic field signature produced is consistent with a passage through an ideal flux rope, ie we would expect to see a bipolar signature in BLAT and a double peaked signature in PHI (The double peaked structure is characteristic of an off centre crossing of a flux rope, Russell and Elphic 1979). If we look more closely at the magnetic field components in this event we see that there is an asymmetry in both the bipolar signature and the

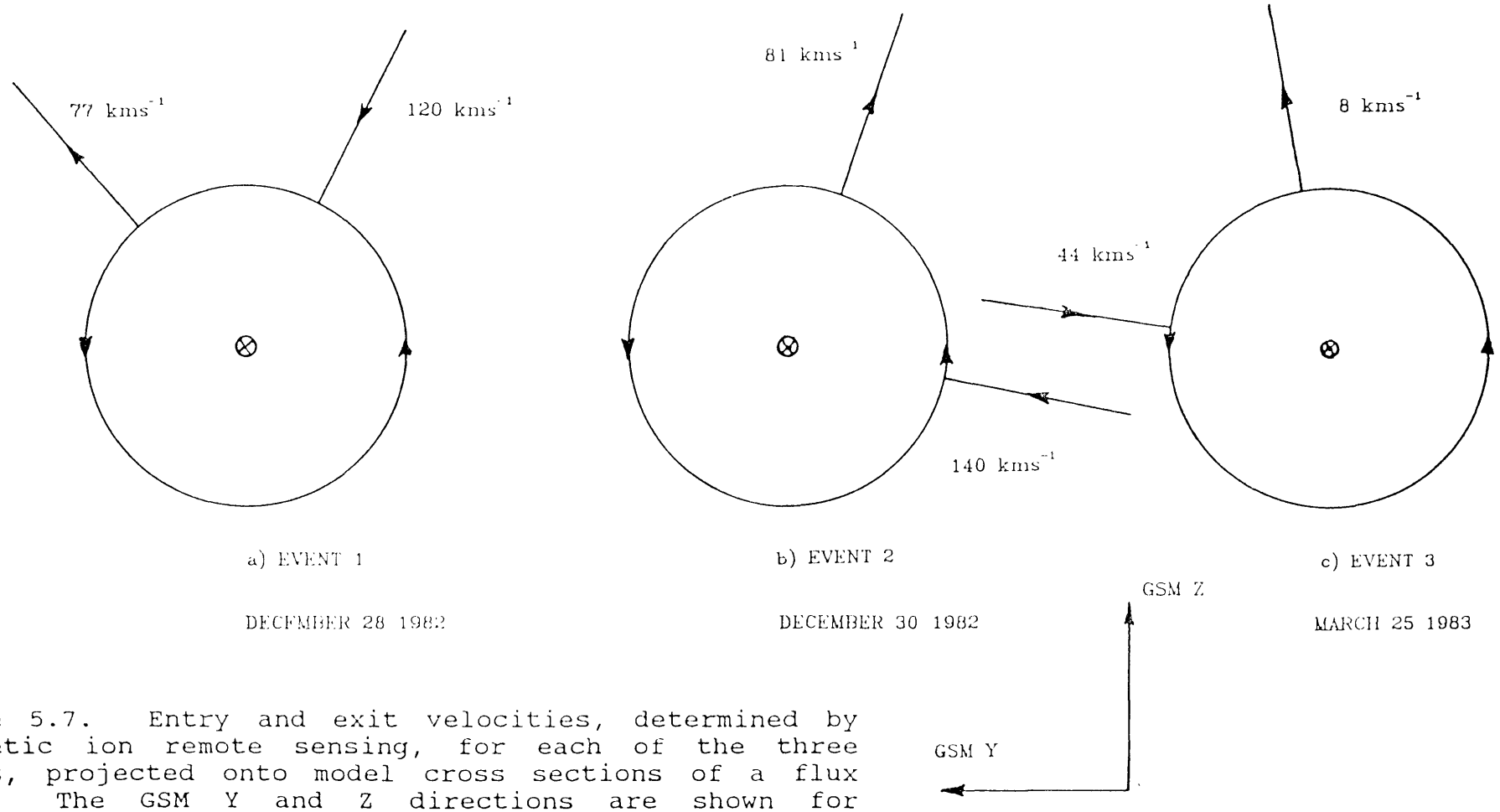


Figure 5.7. Entry and exit velocities, determined by energetic ion remote sensing, for each of the three events, projected onto model cross sections of a flux rope. The GSM Y and Z directions are shown for reference.

double peaked signature. The negative dip in BLAT is larger then the positive one, whilst the second peak in PHI is larger than the first. It is possible to produce asymmetries in these signatures by a rotation of the coordinate system, (the events discussed here are not examined in a preferred coordinate system as were the events studied by Russell and Elphic), but this would not produce the observed effect. In fact, because the larger deviation in BLAT corresponds with the larger peak in PHI, the only way this effect can be produced is by an increase in the pitch length of the rope between entry and exit. An increase in pitch length of could be caused by a true variation of pitch length with GSM X, which is seen because the flux rope is convected in -GSM X direction (plasma bulk velocity inside the flux rope is 200 km s^{-1} tailward, Sibeck et al. 1984), or by the structure being kinked in the GSM Y-Z plane.

If we now look at the magnetic field outside the structure it can be seen that there is a significant difference in the value of BLAT before and after the encounter with the flux rope. This difference is as would be expected if the magnetic field outside the flux rope is draped over the structure (Farrugia et al. 1987). Looking at PHI we see that there is a slight deviation toward negative PHI before and after the encounter, which is again consistent with field line draping (Farrugia et

al. 1987), and suggests that the flux rope axis is inclined to the GSM X axis in the direction of GSM -Y. From figure 5.4 we can see that there is no significant enhancement in earthward or tailward streaming ions outside the flux rope, which tells us that the magnetic field lines on the edge of the structure do not map back to an active neutral line.

Event 2 has a much more complex magnetic field signature than events 1 and 3, (figure 5.1), with the field magnitude showing large fluctuations during the encounter. The bipolar nature of BLAT suggests that the passage through a flux rope would be parallel to the GSM X-Y plane. This is not the case as can be seen from figure 5.7b. In order for the magnetic field data to be consistent with this event being a flux rope PHI must have a large positive value on exit from the structure. As can be seen from figure 5.1 PHI is negative, and tends to zero on exit (implying an exit close to, and below the Y axis of the structure) and so we must conclude that Event 2 is not caused by an encounter with a flux rope. We come now to event 3, which is the only event with a bipolar magnetic field signature in the azimuthal angle PHI. Scholer et al. 1985 concluded that this event represented the crossing of a flux rope from South to North, ie in the GSM Z direction. As can be seen from figure 5.7c this is not the case. Scholer et al's

conclusion was based on the observation of a dusk-dawn (towards GSM -Y) gradient anisotropy at 0720:12 UT, associated with an increase in ion flux. This suggests that the spacecraft is travelling in the GSM Z direction at this time. The exit velocity from the structure (at 0725 UT), as deduced from EPAS measurements, is also approximately in this direction, but as can be seen from figure 5.7c the entry to the structure (at 0712:45 UT) is in approximately the GSM -Y direction. This complicates the interpretation of the magnetic field data show in figure 5.1, which implies that the passage through the flux rope is perpendicular to the GSM X-Y plane. Both these sets of data can, however, be explained in terms of a more complex path through a flux rope. Further evidence for the complexity of the trajectory can be obtained from the variation of BLAT, which passes through zero twice during the encounter. This suggests that ISEE-3 crosses the Z axis of the structure on both occasions.

A possible trajectory through the flux rope, which accounts for the observed magnetic field variations, is shown in figure 5.8. This trajectory is simplified somewhat during the exit from the structure, because the data in figure 5.6, together with the magnetic field data, suggest that ISEE-3 re-enters the structure briefly close to the exit point. This is not entirely unexpected

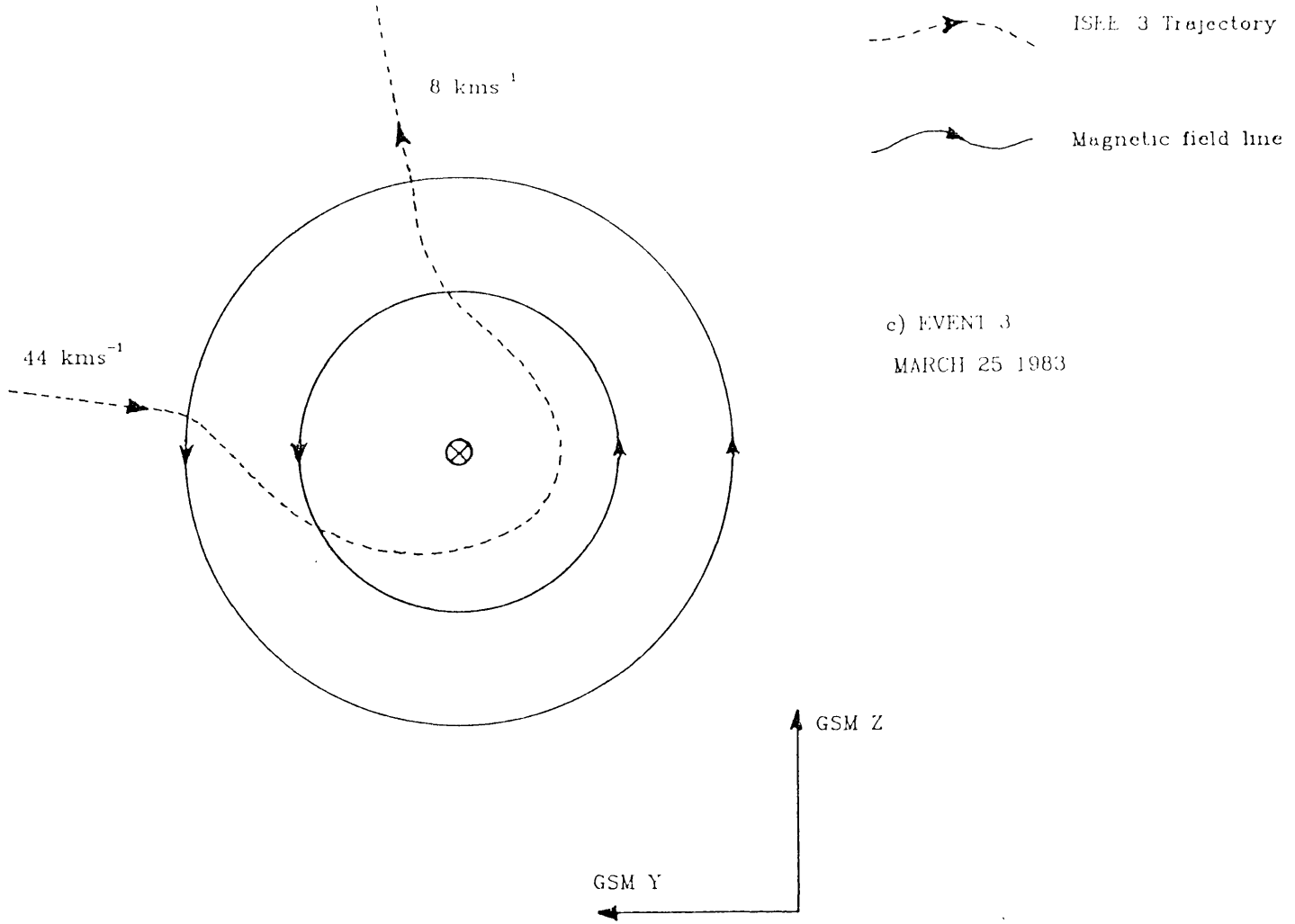


Figure 5.8. Possible trajectory of ISEE-3 through a flux rope, which is consistent with the data in event 3 (25 March 1983).

given the low exit velocity of 8 km s^{-1}. If we look at the magnetic field outside the structure (figure 5.1) there is evidence again for magnetic field line draping, with BLAT showing an asymmetry before and after the encounter and PHI becoming positive before the encounter. This suggests that the magnetic field is draped over the flux rope and the rope axis is inclined towards the GSM +Y direction (Farrugia et al. 1987)

We now consider an alternative explanation for event 2. If we assume that the perturbation in the magnetic field during the event is due to an encounter with the plasma sheet and its boundary layer, then the northward deviation in BLAT implies that ISEE-3 is earthward of a neutral line, whilst the southward deviation in BLAT (commencing at 0503 UT) implies that ISEE-3 is tailward of a neutral line. From figure 5.5 we see that for most of the encounter tailward ion fluxes are greater than earthward fluxes, suggesting that the bulk plasma flow is tailward, however there is a burst of earthward streaming ions during the onset of the ion enhancement. One possible scenario for the production of these magnetic field and energetic ion signatures is that ISEE-3 is initially earthward of the quiet time neutral line (which we would expect to find at this distance from earth) and enters the plasma sheet during the formation of a plasmoid. Thus we see an initial burst of earthward

moving ions, suggesting earthward moving plasma, followed by tailward directed ion fluxes, as the plasmoid begins to move tailwards. The variable magnetic field magnitude suggests that ISEE-3 remains close to the edge of the plasmoid as it moves tailward. This type of magnetic field signature is typical of those seen in association with plasmoids in other studies (Richardson and Cowley 1985, Hones et al. 1984)

Conclusions.

In conclusion close examination of the energetic ion and magnetic field data confirm the flux rope nature of the December 28th 1982 and March 25th 1982 events, although there is no evidence that these flux ropes are detached from the plasma sheet. We can obtain a rough scale size for the flux ropes, from the average speed on entry and exit together with the time spent in each structure. This gives 7.4 R_E for event 1 and 3.5 R_E for event 3 (which is in rough agreement with the value deduced by Scholer et al.). Magnetic field line draping is apparent in both these events which further suggests that they are caused by extended structures. The December 30th 1982 event has been shown to be inconsistent with an encounter with a flux rope, but an alternative explanation for this event can be found in the plasmoid model of geomagnetic substorms.

Chapter 6

Concluding remarks.

The work presented in this thesis, (Chapters 3,4 and 5) deals with observations which were transitory in nature. When observations of this nature are made by a single spacecraft, as in the case of ISEE-3, it is often difficult to determine whether the observations are due to time varying phenomena, or are caused by spatial effects, such as the movement between two plasma regimes. By the use of energetic ion remote sensing we have, to a large extent, been able to isolate the observations produced by spatial effects,

In Chapter 3 it was shown that the energetic ion enhancements associated with travelling compression regions (TCRs) are caused by the movement of the plasma sheet boundary layer past ISEE-3. Given the substorm association observed in the present data set, this result is entirely consistent with the model proposed by Slavin et al., 1984, that is, that TCRs are caused by the tailward motion of plasmoids. The range of TCR lengths is comparable with, but smaller than, that reported by Richardson and Cowley., 1987. This discrepancy is consistent with the plasmoid model, as we would expect the TCR data set to be weighted towards smaller plasmoids, which would not cause ISEE-3 to enter the plasma sheet. The question of whether every magnetic field compression, in multiple TCR events, is caused by a loop of closed magnetic field in the plasma sheet has not

been resolved, and further study of the magnetic field properties of these events, together with detailed information about substorm development, is required.

The main effects of geomagnetic activity on the magnetotail have been shown to be impulsive in nature (Hones et al., 1976, 1984, Richardson and Cowley 1985, 1987, Murphy et al., 1987.), and the work described in chapter 3 supports this idea. In contrast the work detailed in chapter 4 concentrates on the study of the magnetotail plasma sheet, when not disturbed by impulsive events such as plasmoids. In chapter 4 we found that the average thickness of the plasma sheet, in these circumstances was 1.2 R_E. An important result of this study of the magnetotail plasma sheet was that in many cases the plasma sheet was found to be closed, ie magnetically connected to the earth, as far tailwards as 230 R_E. It is tempting to assume that the plasma sheet intervals reported in chapter 4 represent the quiet time conditions in the plasma sheet; preliminary studies using the AE index as a measure of geomagnetic activity indicate that this is not the case. In fact the data set contained events in which AE was as high as 1000 nT, suggesting large geomagnetic disturbances. The interpretation of the plasma sheet data, then, requires some degree of caution; although no obvious dependence of plasma sheet thickness on AE was found, it is unsafe to

assume that the mean thickness deduced represents any sort of ground state of the plasma sheet. The observation of tailward convecting plasma on closed magnetic field lines (ie, magnetic field lines connected to the earth), as far tailward as 230 R_E GSM -X, may indicate that a stable ground state of the plasma sheet does not exist. This would mean that there would be no fixed quiet time position for the distant tail neutral line, instead it would convect tailwards until the magnetotail was disrupted by geomagnetic activity.

A further application of the work developed in Chapter 4 can be found in Smith et al., 1986. This paper interprets the magnetosonic waves, seen in the boundary layers of the distant tail plasma sheet (Tsurutani and Smith, 1986), in terms of the magnetohydrodynamic normal modes of a Harris neutral sheet (the magnetic field magnitude across the sheet is modelled by a tanh function). A preliminary value for the thickness of the plasma sheet, as derived in Chapter 4, is used as a parameter in this model. The results of Smith et al. show that magnetosonic waves, of the required frequency, are in fact predicted by normal mode calculations, although some aspects of the observed polarities of these waves remain unexplained.

Finally, chapter 5 deals with the observation of events, seen in the magnetotail lobes, which are interpreted as flux ropes, with their axes nearly parallel to the magnetotail axis. Any statistical study of these events is, at present, impossible, but efforts to expand the data set are in progress. A number of possible causes of flux ropes in the magnetotail exist; they could be due to the unstable development of waves on the plasma sheet lobe boundary, or they could be formed by magnetic reconnection in the plasma sheet, in a similar way to plasmoids. Observations of flux ropes in the near earth plasma sheet have been reported (Elphic et al.,1987), and it could be that both types of flux rope have a common origin. Before any firm conclusions can be drawn about the origin of flux ropes in the magnetotail lobes, a much larger data set needs to be compiled.

In conclusion the use of energetic ion remote sensing has been confirmed as an important and flexible tool in the study of magnetotail phenomena, allowing us to gain useful insights into the spatial structure of the magnetotail.

References

Andrews, M.K., E. Keppler and P.W. Daly, Plasma sheet motions inferred from medium energy ion measurements, J. Geophys. Res., 86, 7543, 1981.

Axford, W.I. and C.O. Hines, A unifying theory of high latitude geophysical phenomina and geomagnetic storms. Can. J. Phys., 39, 1433, 1961.

Axford, W.I., H.E. Petschek and G.L. Siscoe, The tail of the magnetosphere.
AVCO-Everett Research Report R190, August, 1964.

Balogh, A., G. van Dijen, J. van Genechten, J. Henrion, R.J. Hynds, G. Korfmann, T. Iversen, J. van Rooijen, T. Sanderson, G. Stevens and K.-P. Wenzel, The low energy proton experiment on ISEE-C,
IEEE Trans. Geosci. Electron., GE-16, 195, 1978.

Bame S.J., R.C. Anderson, J.R. Asbridge, D.N. Baker, W.C. Feldman, J.T. Gosling, E.W. Hones, Jr., D.J. McComas, and R.D. Zwickl, Plasma regimes in the deep geomagnetic tail: ISEE-3.
Geophys. Res. Lett., 10, 912, 1983.

Bavassano, B., F. Mariani, and U. Villante, Far magnetospheric field observations by Pioneer 8: The distant bowshock and extended tail.
Space Res., 14, 403, 1974.

Cahill, L.J., Preliminary results of magnetic field measurements in the tail of the geomagnetic cavity.
IGY Bulletin 79, 1964.

Cowley, S.W.H., Magnetosheric asymmetries associated with the Y-component of the IMF.
Planet. Space Sci., 29, 79, 1981

Cowley, S.W.H., R.J. Hynds, I.G. Richardson, P.W. Daly, T.R. Sanderson, K.-P. Wenzel, J.A. Slavin, and B.T. Tsurutani, Energetic ion regimes in the deep geomagnetic tail: ISEE-3.
Geophys. Res. Lett., 11, 275, 1984

Daly, P.W. and E. Keppler, Remote sensing of a flux transfer event with energetic particles,
J. Geophys. Res., 88, 3971, 1983.

Daly, P.W., K.-P. Wenzel and T.R. Sanderson, Sounding of the plasma sheet in the deep geomagnetic tail using energetic particles,
Geophys. Res. Lett., 11, 1070, Oct. 1984.

Daly, P.W., T.R. Sanderson, and K.-P. Wenzel, A method to measure the bulk velocity of an energetic ion distribution in the presence of ion composition mixing.
J Geophys. Res., 90, A2, 1499, 1985.

Dessler, A.J., Length of the magnetospheric tail.
J Geophys. Res., 69, 19, 3913, 1964.

Dessler, A.J. and R.D. Juday, Configuration of auroral radiation in space, 1964

Dungey, J.W., Interplanetary magnetic field and the auroral zones.
Phys. Rev. Lett., 6, 47, 1961.

Dungey, J.W., The length of the magnetos[heric tail.
J Geophys. Res., 70, 7, 1753, 1965.

Elphic, R.C., C.A. Cattell, K. Takahashi, S.J. Bame and C.T. Russell, ISEE-1 and 2 observations of magnetic flux ropes in the magnetotail: FTE's in the plasma sheet?
Geophys. Res. Lett., 13, 7, 648, 1986.

Ershkovich, A.I. and A.A. Nusinov, Geomagnetic tail oscillations.
Cosmic Electro., 2, 471, 1972.

Farquahar, R.W. and D.W. Dunham, A new trajectory concept for exploring the earth's geomagnetic tail,
J. Guidance and control, 4, 192-196, 1981.

Farrugia, C.J., R.C. Elphic, D.J. Southwood and S..H. Cowley, Field and flow perturbations outside the reconnected field line region in flux transfer events: Theory.
Planet. Space Sci., 35, 2, 227, 1987.

Fransden, A.M.A., B.V. Connor, J. van Amersfoort and E.J. Smith, The ISEE-C Vector Helium Magnetometer,
IEEE Trans. Geosci. Electron., GE-16, 195, 1978.

Fritz, T.A., and S.C. Fahnenstiel, High temporal resolution energetic particle soundings at the magnetopause on November 8 1977 using ISEE-2,
J Geophys. Res., 87, 2125, 1982.

Furth, H.P., J. Killeen and M.N. Rosenbluth, Finite-Resistivity instabilities of a sheet pinch.
Phys. of Fluids, 6, 459-484, 1963.

Gosling, J.T., ISEE-3 plasma measurements in the lobes of the distant geomagnetic tail: Inferences concerning reconnection at the dayside magnetopause.
Magnetic Reconnection in Space and Laboratory Plasmas, edited by E.W. Hones, Jr., American Geophysical Monograph 30, Washington D.C. pp. 157, 1984.

Gosling J.T., D.N. Baker, S.J. Bame, E.W. Hones, D.J. McComas, R.D. Zwickl, J.A. Slavin, E.J. Smith, and B.T. Tsurutani, Plasma entry into the distant tail lobes: ISEE-3.
Geophys. Res. Lett., 11, 1078, 1984.

Gosling, J.T., D.N. Baker, S.J. Bame, W.C. Feldman, R.D. Zwickl and E.J. Smith, North-south and dawn-dusk asymmetries in the distant tail lobes: ISEE-3
J. Geophys. Res., 90, 6354, 1985.

Heppner, J.P., N.F. Ness, T.L. Skillman and C.S. Scearce, Explorer X magnetic field measurements.
J. Geophys. Res., 68, 1, 1963.

Hones, E.W., Jr., The magnetotail: Its generation and dissipation.
Physics of solar and planetary environments, ed. D.J. Williams, 558-571, AGU, Washington, D.C., 1976

Hones, E.W., Jr., D.N. Baker, S.J. Bame, W.C. Feldman, J.T. Gosling, D.J. McComas, R.D. Zwickl, J.A. Slavin, E.J. Smith, and B.T. Tsurutani, Structure of the magnetotail at 220 R_E, and its response to geomagnetic activity.
J. Geophys. Res., 11, 5, 1984.

Intriligator, D.S., H.R. Collard, J.D. Mihavlov, O.L. Vaisberg, and J.H. Wolfe, Evidence for earth magnetospheric tail associated phenomena at 3100 R_E.
Geophys. Res. Lett., 6,585, 1979.

Jorgensen, T.S., E.Friis-Christensen, and J. Wilhjelm, Interplanetary magnetic field direction and high latitude ionospheric currents.
J. Geophys. Res., 77, pp1976, 1972.

Ness, N.F., The earth's magnetotail.
J. Geophys. Res., 70, 2989, 1965.

Owen, C.J., and S.W.H. Cowley, Simple models of time dependent reconnection in a collision-free plasma with an application to substorms in the geomagnetic tail.
Planet. Space Sci., submitted August 1986.

Richardson, I.G. and S.W.H. Cowley, Plasmoid associated energetic ion bursts in the deep geomagnetic tail: Properties of the boundary layer,
J. Geophys. Res., Jan. 1986, 90, 12133, 1985

Richardson, I.G., S.W.H. Cowley, E.J. Hones, Jr., S.J. Bame, Plasmoid associated energetic ion bursts in the deep geomagnetic tail: Properties of plasmoids and the post plasmoid plasma sheet.
J. Geophys. Res., in press may 1987

Russell, C.T., and G. Atkinson, Comments on a paper by J.P. Heppner, Polar cap electric field distributions related to interplanetary magnetic field direction.
J. Geophys. Res., 78, 4001, 1973.

Russell, C.T., Some comments on the topology of the geomagnetic tail,
J. Geophys. Res., 82, 1625, 1977.

Russell, C.T. and R.C. Elphic, Obsevations of magnetic flux ropes in the venus ionosphere.
Nature, 279, June 1979.

Saito, T., Geomagnetic pulsations.
Space Sci. Rev., 10, 319, 1969.

Sakurai, T., and T. Saito, Magnetic pulsations Pi 2 and substorm onset.
Planet. Space Sci., 24, 573, 1976.

Scholer, M., G. Gloeckler, B. Klecker, F.M. Ipavich, D. Hovestadt and E.J. Smith, Fast moving plasma structures in the distant magnetotail,
J. Geophys. Res., 89, 6717, 1984.

Sibeck D.G., G.L. Siscoe, J.A. Slavin, E.J. Smith, S.J. Bame and F.L. Scarf, Magnetotail flux ropes.
Geophys. Res. Lett., 11, 1090, 1984.

Sibeck D.G., G.L. Siscoe, J.A. Slavin, E.J. Smith, S.J. Bame and F.L. Scarf, Magnetotail's response to a strong magnetic field By: Twisting flattening and field line draping.
J. Geophys. Res., 90, 4011, 1985.

Sibeck D.G., J.A. Slavin, and E.J. Smith, ISEE-3 Magnetopause crossings: Evidence for the Kelvin-Helmholtz Instability.
Submitted to Chapman Conference Monograph on Magnetotail Physics, 1986.

Slavin, J.A., B.T. Tsurutani, E.J. Smith, D.E. Jones, and D.G. Sibeck, Average configuration of the distant (<220 R_E) magnetotail: Initial ISEE-3 magnetic field results. Geophys. Res. Lett., 10, 973, 1983.

Slavin, J.A., E.J. Smith, B.T. Tsurutani, D.G. Sibeck, H.J. Singer, D.N. Baker, J.T. Gosling, E.W. Hones, and F.L. Scarf, Substorm associated traveling compression regions in the distant tail: ISEE-3 Geotail observations, Geophys. Res. Lett., 11, 657, July 1984.

Slavin, J.A., E.J. Smith, D.G. Sibeck, D.N. Baker, R.D. Zwickl, and S.-I. Akasofu, An ISEE-3 study of average and substorm conditions in the distant magnetotail.
J. Geophys. Res., 90, 10875, 1985.

Smith, P.R., K.I. Hopcraft and N. Murphy, An interpretation of magnetosonic waves in the boundary regions of the plasma sheet as seen by the ISEE-3 spacecraft.
Submitted to Chapman Conference Monograph on Magnetotail Physics, 1986.

Tsurutani, B.T. and E.J. Smith, Magnetosonic waves adjacent to the plasma sheet in the distant magnetotail: ISEE-3,
Geophys. Res. Lett., 11, 331, 1984.

Tsurutani, B.T., D.E. Jones, and D.G. Sibeck, The two lobe structure of the distant (X > 200 R_E) magnetotail, Geophys. Res. Lett., 11, 1066, 1984.

Tsurutani, B.T., B.E. Goldstien, M.E. Burton and D.E. Jones, A review of the ISEE-3 geotail magnetic field results.
Planet. Space Sci. 34, 10, 931, 1986.

Tsurutani, B.T., M.E. Burton, and E.J. Smith, Distant (200-238 R_E) magnetotail lobe characteristics during queit solar wind conditions.
Planet. Space Sci. 35, 3, 285, 1987.

van Rooijen, J.J., G.J. van Dijen, H.Th. Lafleur and P. Lowes, Alow energy proton spectrometer for directional distribution measurements in space.
Space Sci. Inst. 4, 373-392, 1979.

Vasyliunas, V.M., Theoretical models of magnetic field line merging, 1.
Rev. of Geophys. and Space Phys., 13, 1, 303, 1975.

Voots, G.R., D.A. Gurnett, and S.I. Akasofu, Auroral kilometric radiation as an indicator of auroral magnetic disturbance.
J. Geophys. Res., 82, 2259, 1977.

Walker, R.C., U. Villante, and A.J. Lazarus, Pioneer 7 observations of plasma flow and field reversal regions in the distant geomagnetic tail.
J. Geophys. Res., 80, 1238, 1975.